

Copyright  
by  
Hongwoo Jang  
2022

**The Dissertation Committee for Hongwoo Jang certifies that this is the approved  
version of the following Dissertation:**

**Graphene E-Tattoos: Design, Fabrication, Characterization, and  
Applications as Wearable Sensors**

**Committee:**

Nanshu Lu, Supervisor

Rui Huang

Jonathan W. Valvano

Guihua Yu

**Graphene E-Tattoos: Design, Fabrication, Characterization, and  
Applications as Wearable Sensors**

**by**

**Hongwoo Jang**

**Dissertation**

Presented to the Faculty of the Graduate School of

The University of Texas at Austin

in Partial Fulfillment

of the Requirements

for the Degree of

**Doctor of Philosophy**

**The University of Texas at Austin**

**May 2022**

## **Dedication**

This dissertation is dedicated to my family for their endless support and love.

## Acknowledgements

First, I would like to thank my supervisor, Dr. Nanshu Lu, for her guidance throughout my Ph.D. journey. I truly learned a lot from her not only how to become an independent researcher but how to become a person with desired soft skills. My research has become so fruitful due to her insights, vision, support, and suggestions. I respect her enormous passion for research and training her students. I can't thank her enough and I'm excited to deliver what I've learned from this group to the next chapter of my life.

I would like to thank Dr. Rui Huang, Dr. Guihua Yu, and Dr. Jonathan W Valvano for being my committee members and for their support and feedback on my dissertation. I also would like to thank my collaborators, Dr. Roozbeh Jafari and Mr. Kaan Sel at Texas A&M University, for their support of electronics for bio-impedance, sharing their instruments, and consistent feedback for multiple years. I want to express my gratitude to Dr. Krishnaswamy Ravi-Chandar in the Department of Aerospace Engineering and Engineering Mechanics at UT Austin for sharing his wisdom doing micro-mechanical analysis and training for high-power microscopy. Also, Dr. Raluca Gearba in Texas Materials Institute has helped me with various instruments training in a cleanroom, debugging issues together, and providing me tremendous help. Thank you so much.

Financial support for this dissertation from the US National Science Foundation (Grant Nos. 1738293, 2133106), US Office of Naval Research (Grant No. N00014-20-1-2112), and US National Institute of Health (Grant No. 1R01EB028106) is highly appreciated.

My research group members have been always nice and supportive and here I want to thank you for the friendship, support, and feedback during and beyond my Ph.D. journey.

Thank you so much, Dr. Hyoyoung Jeong, Dr. Taewoo Ha, Dr. Shutao Qiao, Dr. Shideh Kabiri Ameri, Dr. Liu Wang, Dr. Zhaohe Dai, Dr. Danny Sanchez, Dr. Siyi Liu, Kyoung-Ho Ha, Sangun Kin, Heeyong Huh, Seungmin Kang, Xiangxing Yang, Yifan Rao, Eunbin Kim, Susmita Gangopadhyay, and many others.

Finally, I would love to thank my family for their countless support and unconditional love throughout my Ph.D. journey. There have been many failures and frustrations, but I could stand again and move forward because of their support and love. Thank you so much and I love you all, especially, my father, mother, sister, Aggie, and fiancé Hyoju.

## Abstract

# Graphene E-Tattoos: Design, Fabrication, Characterization, and Applications as Wearable Sensors

Hongwoo Jang, Ph.D.

The University of Texas at Austin, 2022

Supervisor: Nanshu Lu

The remarkable mechanical robustness and unique electrical/optical properties make atomically thin graphene a promising candidate for future flexible, stretchable, and bio-integrated electronics. Our invention of sub-micron-thin graphene e-tattoos (GET), designed as filamentary serpentine ribbons of a graphene-polymer bilayer, has demonstrated superior skin-conformability, imperceptibility, and low contact impedance for monitoring various physiological signals, such as ECG, EMG, EEG, skin hydration, and temperature. However, there are unanswered questions on the failure mechanisms of GET and unsolved challenges to make GET applicable in ambulatory sensing. This dissertation attempts to address those critical issues. First, to reveal the failure mechanism of GET and its electrical contacts, I conducted uniaxial tensile tests with *in situ* microstructure and Raman investigations. I discovered four deformation/fracture stages of GET: pre-cracking elastic deformation, limited micro-cracking in graphene, extensive micro-cracking in graphene, and macro-cracking in the supporting polymer layer. Various conductive overlayers need to directly laminate on graphene to make electrical contacts. I

placed gold/polyethylene terephthalate (Au/PET) as well as GET over GET. I found that the Au/PET - GET interface is very vulnerable due to the large stiffness mismatch between them but the GET - GET interface behaves very similar to intact GET electromechanically. Second, to reliably connect GET to rigid back-end-circuits with orders of magnitude mismatch in mechanical stiffness, I proposed the idea of heterogeneous serpentine ribbons (HSPR), which refer to serpentine GET partially overlapping with a serpentine gold-polyimide (Au/PI) ribbon. When the Au/PI step edge is located at the arm of the GET serpentine, 50 folds of strain reduction in GET using HSPR vs. heterogeneous straight ribbons (HSTR) have been confirmed. This simple method offers a generic remedy for the long-standing interconnect challenges between ultrathin sensors and rigid electronics. Finally, based on the electromechanical understanding of GET and the novel design of HSPR, I successfully created an unobstructive and robust GET sensor that is capable of continuous and ambulatory monitoring of electrodermal activity (EDA) on the palm.

## Table of Contents

List of Tables .....	xii
List of Figures .....	xiii
Chapter 1: Introduction .....	1
1.1 Overview of 2D-Materials-Based Wearables .....	2
1.2 Design .....	6
1.3 Fabrication .....	11
1.4 Characterizations .....	15
1.5 Applications .....	16
1.5.1 Strain Sensors.....	17
1.5.2 Electrophysiological Sensors .....	20
1.6 Scope of Research.....	24
Chapter 2: The Invention of Graphene Electronic Tattoos (GET) .....	26
2.1 Objective and Overview .....	26
2.2 Mechanical and Optical Characterizations .....	28
2.3 Electrical Performance of GET on Skin .....	31
2.4 Impact by Motion Artifacts.....	33
2.5 Summary .....	34
Chapter 3: Stretchability of Linear GET and of Its Electrical Contacts .....	36
3.1 Objective and Overview .....	36
3.2 Stretchability of CVD Graphene on Polymer Substrates – A Survey .....	38
3.3 Stretchability and Electromechanical Behaviors of GET .....	40
3.4 Microstructure Analysis of GET under Deformation .....	43

3.4.1 Raman Mapping under Uniaxial Tension .....	43
3.4.2 High-Power Optical Microscopic Analysis .....	44
3.5 Stretchability of Electrical Contacts with GET .....	48
3.6 Discussion .....	52
3.6.1 Cyclic Behaviors of GET .....	52
3.6.2 Effect of Polymer Thickness .....	53
3.6.3 Effect of the Adhesion between GET and Substrate .....	54
3.7 Summary .....	55
Chapter 4: Enhancing the Stretchability of GET Electrical Contacts Through Heterogenous Serpentine Ribbons (HSPR) .....	57
4.1 Objective and Overview .....	57
4.2 Fabrication Process .....	58
4.3 Mechanical Characterizations of HSPR .....	60
4.3.1 Serpentine Geometry Effect .....	62
4.3.2 Experimental Stretchability .....	64
4.3.3 Strain Reduction Validated by FEM Simulation .....	66
4.3.4 Stretchability Prediction Using FEM Simulation .....	68
4.3.5 Stretchability in Transverse Direction .....	69
4.3.6 Stretchability Depending on Stiffness Ratios .....	71
4.4 Summary .....	73
Chapter 5: GET for Ambulatory Long-Term EDA Sensing .....	75
5.1 Objective and Overview .....	75
5.2 Design and Working Principles of GET-Based EDA Sensor .....	78
5.3 Strain Isolation by Soft Interlayer .....	81

5.3.1 Experiment.....	81
5.3.2 FEM Simulation.....	82
5.4 Electrode-to-Skin Interface Characterizations.....	85
5.4.1 Electrode-to-Skin Impedance Measurements .....	85
5.4.2 Modeling Conformability .....	86
5.4.3 Established Equivalent Circuit Model .....	88
5.5 EDA Measurement and Statistical Analysis.....	93
5.5.1 EDA Testing Protocol.....	93
5.5.2 EDA Measurement.....	95
5.5.3 SCR Detection Algorithm and Statistical Analysis .....	96
5.6 Wearability of GET-Based EDA Sensor .....	100
5.6.1 Impact by Motion Artifacts.....	100
5.6.2 Short-Term Wearability .....	102
5.6.3 Long-Term Wearability .....	103
5.7 Summary.....	104
Chapter 6: Conclusions and Outlook .....	106
Appendices.....	108
References.....	126

## List of Tables

Table 3.1:	A survey of the stretchability of CVD graphene on different polymer substrates under different strain quantification methods [247].....	39
Table 5.1:	Values of circuit parameters either from literature (indicated by *) or from our own measurements.....	89
Table 5.2:	An EDA testing video consisting of five different sessions – Expectation, "Uncontrolled" Emotional, Expectation (identical as session #1), "Controlled" Emotional, and "Habituation." .....	93
Table A1:	Index of the affective pictures used from the EmoMadrid database. Mean values are scaled from 0 (neutral) to 2 (maximum arousal) by EmoMadrid. Images from No. 1 – 10 are used for session (4) and No. 11 is used for session (5).....	122
Table A2:	EDA correlation score for human subject #1.....	123
Table A3:	EDA correlation score for human subject #2.....	124
Table A4:	EDA correlation score for human subject #3.....	125

## List of Figures

Figure 1.1: An Ashby plot of the stretchability and the thickness of soft wearable electronics based on 2D materials and non-2D materials [6,32–36,38,41,46,53,54,62,65,66,94,105,107,116,117,148–153].	5
Figure 1.2: Various types of mechanisms and corresponding applications of 2D materials for wearable electronics [13,117,154–156].	6
Figure 1.3: Examples of soft structures. [In Press, <a href="https://doi.org/10.1016/j.matt.2022.02.006">https://doi.org/10.1016/j.matt.2022.02.006</a> ] (a) A paper-cut serpentine ribbon and the ribbon buckled out-of-plane upon stretching [161]. (b) A stretchable hydration sensor array on skin with serpentine-plus-island design [164]. (c) A multifunctional epidermal electronic platform with both filamentary serpentine and serpentine-plus-island design [166]. (d) Micrographs of a glass-based stretchable photonic resonator in undeformed state (upper panels) and at 36% nominal tensile strain (lower panels) [170]. (e) Multi-stage unraveling of a hierarchical serpentine with fractal design under uniaxial stretching [163]. (f) Fractal electrodes and temperature sensors for epicardial electrotherapy [174]. (g) A serpentine mesh conformed to a fingertip [175]. (h) Geometric parameters of a kirigami design (left) and stretchable kirigami electrodes laminated on a mouse brain for visual stimulation (right) [178]. (i) A fiber-based generator woven into a lab coat to power a wireless temperature monitoring wristband [184].	10

Figure 1.4: Manufacturing methods of 2D-materials-based wearable electronics. (a) “Cut-and-paste” method for graphene electronic tattoos (GET) sensors [32]. (b) Inkjet printing of rGO on a textile [188]. (c) i) Laser-induced graphene on a polyimide substrate [191] and ii) Laser-induced graphene on a polyimide textile using UV laser [198]. .....14

Figure 1.5: 2D-materials-based strain sensors. (a) Strain sensor based on single-layer graphene and the demonstration on the finger [68]. (b) Highly stretchable and sensitive strain sensor using fragmented graphene foam and the demonstration on the wrist [133]. (c) High-performance strain sensor with fish-scale-like graphene-sensing layers on the wrist [90]. (d) A wearable strain sensor for precise home-based pulse wave monitoring on the wrist [103]. (e) Carbon/graphene composite nanofiber yarns for highly sensitive strain sensors and the demonstration on the forearm [123]. (f) MoS<sub>2</sub>-based strain sensor on the thumb and the output signals and gauge factor over strain [105]. .....18

Figure 1.6: 2D materials in electrophysiology sensing applications. (a) Flexible nylon textile with rGO. (i) rGO coated sample for ECG testing, (ii) ECG signal obtained from graphene-clad textile electrode [91]. (b) Inkjet-printed graphene-based conductive patterns on textiles. (i) SEM images and a textile sample picture of the inkjet-printed rGO ink onto cotton fabrics, (ii) Experimental methods for measuring heart rate using graphene textile, (iii) Illustration of the measured ECG signal using graphene textile [188]. (c) Graphene electronic tattoo (GET) sensors for skin impedance, EEG, ECG, and EMG sensing. (i) GET on a relaxed skin, (ii) Measured EEG data from the GET mounted on the forehead, (iii) ECG on the chest, and (iv) EMG on the forearm [32], (v) GET EOG sensor worn around human eyes, (vi) Measured EOG signal recorded by GET EOG sensor [4]. (d) Pt-TMD tattoos based on platinum diselenide (PtSe<sub>2</sub>) and platinum ditelluride (PtTe<sub>2</sub>) layered materials for multiple vital sign measurements. (i) Pictures of Pt-TMD device on the skin with polymeric support, (ii-iii) Demonstration for ECG and EEG measurement with PtSe<sub>2</sub> and PtTe<sub>2</sub> electrodes [204].....23

Figure 2.1: Mechanical and optical characterization of the GET [32]. (a) Picture of the as-fabricated GET with a white background, labeled with different sensors including graphene-based electrophysiological sensors (GEPS), a resistance temperature detector (GRTD), and a skin hydration sensor (GSHS). (b) The thickness of PMMA was measured by a profilometer to be  $463 \pm 30$  nm. (c) Optical transparency of bare PMMA and Gr/PMMA. (d) Normalized resistance of the GET versus applied tensile strain. The linear GET ribbon ruptures at 20%, whereas the serpentine-shaped GET can be stretched up to 50%. (e) Less than 6% change in GRTD resistance after 1300 cycles of 15% stretching. (f) GET mounted on skin. (g, h) GET on skin compressed and stretched by 25%, respectively. (i) Change in GEPS and GRTD resistance after all kinds of skin-tolerable deformations. (j to l) Magnified photographs of a GET on relaxed, compressed, and stretched skin, which demonstrate its full conformability even under skin deformation.....28

Figure 2.2: Electrical performance of the GET on skin [32]. (a) Without any skin preparation, GET–skin contact impedance is almost on par with that between commercial gel electrodes and skin. (b) EEG sensing on the forehead with both the GET and gel electrodes (left). When the eyes were closed, an  $\alpha$  rhythm of 10 Hz is visible in both spectrograms. (c) ECG measured synchronously by the GET and gel electrodes. Characteristic ECG peaks can be measured by both electrodes. (d) EMG sensing on the forearm with the GET and gel electrodes when the subject squeezed the hand exerciser three times.....31

Figure 2.3: Comparison of motion artifacts in GET and gel electrodes [32]. (a, b) The motion was induced by poking the chest using a glass rod. (c) ECG synchronously recorded by a GET and gel electrodes shows comparable susceptibility to motion.....	34
Figure 3.1: Uniaxial tensile test with <i>in situ</i> electrical resistance measurement [247]. (a) A schematic of the experimental setup where graphene was covered by Au/PET for electrical contact and fully clamped at the two ends. (b) Representative raw and smoothed curves of measured normalized electrical resistance of graphene ( $R/R_0$ ) as a function of the applied strain ( $\epsilon_{app}$ ). (c) Slope of the curve in (b) ( $d(R/R_0)/d\epsilon_{app}$ ) (red) and the gauge factor ( $GF = (\Delta R/R)/\epsilon_{app}$ ) (blue) as functions of the applied strain. (d) Illustrations of the four-stage deformation and fracture of Gr/PMMA. ....	40
Figure 3.2: Raman mapping over $20 \mu\text{m} \times 20 \mu\text{m}$ graphene at 0%, 2% and 4% of applied strains [247]. Black arrows indicate the direction of stretching. Blueshift and redshift indicate tension and compression, respectively. ....	43
Figure 3.3: High-power optical micrographs of the Gr/PMMA under 500x (first and third rows) and 2000x (second and fourth rows) magnifications at (a) 0%, (b) 4%, (c) 10% and (d) 16% of applied strains ( $\epsilon_{app}$ ) [247]. Tensile strain was applied along the vertical direction of the micrographs. Yellow dashed lines highlight the edges of PMMA. Black boxes offer blown-up views of graphene cracks.....	45
Figure 3.4: Normalized electrical resistance of Gr/PMMA (black), Au/Cr/PMMA (orange), and Au/PET (magenta) ribbons plotted together against the applied strain [247]. The three insets display the center region of the Au/Cr/PMMA, Gr/PMMA and Au/PET specimens at failure.....	49

Figure 3.5: The stretchability of electrical contacts with Gr/PMMA [247]. (a) Au/PET and (b) Gr/PMMA overlayer laminated on Gr/PMMA with Au or graphene facing graphene to make electrical contacts. Au/PET was attached to Gr/PMMA through ACF adhesive but nothing was applied between two Gr/PMMA. The left panels plot the normalized end-to-end electrical resistance vs. applied strain. Right panels are micrographs at the edge of the contact taken at the fracture point. Red dashed line in the micrograph of (b) highlights the edge of the top Gr/PMMA.....51

Figure 3.6: Normalized resistance of the Gr/PMMA ribbon under applied cyclic strain of (a) 0-2% at 0.5 Hz and (b) 0-8% at 0.125 Hz [247]. .....52

Figure 3.7: PMMA thickness effect on the stretchability of (a) the Gr/PMMA ribbons and (b) Au/PMMA ribbons [247]. The inset in (a) shows the brittle fracture of graphene on 1- $\mu$ m-thick PMMA at the applied strain of 10%. .....54

Figure 3.8: Effect of Tegaderm adhesive on Gr/PMMA stretchability [247]. (a) Comparison of the normalized resistance vs. applied strain for Gr/PMMA ribbons transferred on the sticky (black) and non-sticky (red) sides of the Tegaderm. (b) The micrographs at fracture on the non-sticky side. Black dashed lines indicate the edge of the Gr/PMMA ribbon. Red circles highlight the delamination of the Gr/PMMA around the macro-cracks. ....55

Figure 4.1: Laminate-cut-paste fabrication of HSPR (Arm). Polyimide (PI) precursor – polyamic acid (PAA) is spin-coated on a CVD graphene grown on a Cu foil. The Cu is etched in  $\text{FeCl}_3$  solution, and the PI-supported graphene (Gr/PI) is transferred onto a commercial tattoo paper with graphene facing up. 100-nm-thin Au deposited on 650-nm-thin PI is partially laminated over the GET. A UV laser carves the two sheets into HSPR (Arm) which indicates that the Au/PI terminates at the arm of the serpentine. The patterned HSPR (Arm) can be pasted onto human skin by wetting the tattoo paper. ....58

Figure 4.2: Three different heterogeneous configurations (HSTR, HSPR (Crest), HSPR (Arm)) are stretched experimentally and numerically. The red arrow and black arrow highlight the edge of Au/PI and the edge of GET, respectively. ....60

Figure 4.3: Parametric study of HSPR (Arm) geometry. (a) Geometric parameters, (b-d) Schematics of HSPR (Arm) geometry depending on (b)  $w/r$ , (c)  $l/r$ , and (d)  $\alpha$ . Dark grey, red, and yellow indicates GET, GET on Au/PI, and Au/PI, respectively. Strain reduction of HSPR (Arm) depending on (e)  $w/r$ , (f)  $l/r$ , and (g)  $\alpha$ , accordingly. ....63

Figure 4.4: (a) The resistance change over strain for the three different configurations in comparison to straight GET. Micrographs at fracture are also shown on the right. Red-dashed circle indicates the location of the fracture. (b) Stretchability comparison for three configurations and straight GET. ....65

Figure 4.5: Cyclic test of HSPR (Arm) under 20% of applied strain with 0.25 Hz up to 10,000 times. ....66

Figure 4.6: (a) FEM results of stretching HSTR, HSPR (Crest), and HSPR (Arm) without showing the Ecoflex substrate. The edge of Au/PI is zoomed in to show the strain in GET at the Au/PI step edge, which is expected to suffer from strain concentration. (b) Comparison of strains at the Au/PI step edge in the heterostructures vs. the homogenous straight GET, which confirms the strain reduction effect in HSPR, especially in HSPR (Arm).....67

Figure 4.7: Comparison between the normalized maximum strain in FEM and the normalized stretchability in an experiment for different configurations. ....69

Figure 4.8: Transverse stretching of HSPR in FEM. (a) 300-nm-thin GET is connected to 750-nm-thin Au/PI on a 100- $\mu$ m-thick Ecoflex. 20% of strain is applied in the transverse direction. The FEM simulation results with the edge of contact of Au/PI located at (b) crest and (c) arm of the serpentine are displayed. The pink arrow indicates the global maximum strain, and the red arrow indicates the local maximum strain at the edge of the interface. Ecoflex is not displayed in the simulation results. ....70

Figure 4.9: The maximum strain on HSPR (Arm) depending on stiffness ratios. The 300-nm-thin GET is connected to (a) 750-nm-thin Au/PI, (b) 13- $\mu$ m-thick Au/PI, and (c) 18- $\mu$ m-thick Cu, which has the stiffness ratio of 7.7, 37.6, and 1596, respectively. Red arrows indicate the edge of Au/PI and pink arrows indicate the global maximum strain. The HSPRs are supported by 100- $\mu$ m-thick Ecoflex, and it is not displayed in the simulation results. ....72

Figure 4.10: Stretchability of HSPR (Arm) with different stiffness ratios.....73

Figure 5.1: A wireless palm electrodermal activity (EDA) sensor based GET connecting to a rigid E4 wristband through HSPR and soft interlayer. (a) An overall device schematic where the detailed structures of the HSPR and the soft interlayer are illustrated in blown-up views. The HSPR is composed of GET serpentine ribbon overlapping with Au/PI serpentine ribbon via just van der Waals forces. The cross-sectional view along the blue dashed arrow illustrates how the Au layer is connected to the rigid electrode built into the wristband through a conductive rubber. (b-d) Photographs showing GET EDA sensor on the palm when the hand is undeformed and deformed in macroscale, mesoscale, and microscale, highlighting two main features of GET – transparency and skin-conformability. (e) A representative EDA signal with both low-frequency tonic component and high-frequency phasic component illustrated. (f) Example EDA signals. ....78

Figure 5.2: Experimental characterization of the soft interlayer. (a) Photograph of soft interlayer covering the Au/PI laminated on the human wrist. (b) Stress-strain curve of the commercial conductive silicone rubber (SNE-553). (c) Cyclic test of SNE-553 under 20% of compressive strain with 0.1 Hz to confirm the stability of resistance. (d) Side-view of Ecoflex and SNE-553 sandwiched by glass slides before and after a shear displacement of 1 mm. ....81

Figure 5.3: Strain isolation effect of the soft interlayer. (a) FEM schematic to validate the strain isolation by the soft interlayer. Red arrows indicate the areas of interest with potential strain concentration. (b) FEM results showing the overall strain distribution and zoomed-in strain in Au at the areas of interest. ....	84
Figure 5.4: FEM simulation results showing the maximum strain in Au without the soft interlayer. ....	84
Figure 5.5: Electrode-skin interface impedance characterization. (a) A photograph of HSPR and gel electrodes connected to two identical E4 wristbands. (b) Impedance vs. frequency measured for GET (blue) and gel electrodes (red) of the same diameter. ....	86
Figure 5.6: (a) Analytical prediction of conformability of PI on the skin depending on its thickness. (b) Micrographs of 300-nm-thin GET (top) and 750-nm-thin Au/PI (bottom) laminated on human skin. It is obvious that only GET can fully conform to the skin, which is consistent with the analytical prediction. ....	87
Figure 5.7: Schematic of electrode-skin interface cross-section. ....	88
Figure 5.8: The corresponding circuit models to the schematic of electrode-skin interface cross-section. ....	89
Figure 5.9: The simplified equivalent circuit model between gel electrodes and the skin. ....	91
Figure 5.10: The simplified equivalent circuit model between Au/PI and the skin. ....	92
Figure 5.11: The simplified equivalent circuit model between HSPR and the skin. ....	92

Figure 5.12: (a) Raw data and decomposed data of EDA measured by the GET sensor. (b) Comparison of EDA measured by GET (blue) vs. gel electrodes (red) on subject #1. (c) Comparison of EDA measured by GET on the palm (blue) vs. dry metal electrodes on the wrist (black). .....	95
Figure 5.13: SCR detection algorithm for the correlation analysis. ....	97
Figure 5.14: Parameters of an EDA signal used in the statistical analysis to validate the correlation between GET and gel.....	99
Figure 5.15: A total number of events measured by GET (blue) and gel electrodes (red) on five different subjects. ....	100
Figure 5.16: Comparison of the motion artifacts in GET- and gel-measured EDA signals when subjected to hand clenching, wrist bending, cell phone grabbing, and finger poking .....	101
Figure 5.17: (a) Rubbing GET by a metal key ring only produces negligible artifacts compared with the EDA signal. (b) EDA quickly spikes and recovers when GET undergoes a quick exposure to water.....	102
Figure 5.18: Long-term, ambulatory EDA sensing using GET (blue) and gel electrodes (red) during driving, dinner, watching TV, exercise, study, sleep, exercise, and study. Gel electrodes were frequently delaminated and had to be replaced three times. Insets show the photographs of gel electrode delamination and Au/PI rupture beneath the soft interlayer. ....	103
Figure A1: Finite element analysis results of the normal strain in the stretching direction ( $\epsilon_{11}$ ) in the Gr/PMMA ribbon. Note that most of the Gr/PMMA ribbon experiences $\epsilon_{11}$ similar to the applied strain. ....	109
Figure A2: Repeatable electromechanical behavior of four Gr/PMMA ribbons on 3M Tegaderm tapes under tension. ....	110

Figure A3: Characterization of commercial CVD-grown graphene under Raman spectroscopy. (a) Three random spots were chosen, and the characteristic peaks of the graphene (2D peak and G peak) were measured. The inset figure shows a zoomed-in view of the 2D peaks. (b) Raman mapping was performed within an area of 80 $\mu\text{m}$ x 80 $\mu\text{m}$ of the CVD graphene to construct a contour plot of the ratio of 2D peak intensity over G peak intensity ( $I_{2D}/I_G$ ). .....	111
Figure A4: A micrograph of Gr/PMMA on a 3M Tegaderm tape at 16% of applied strain. Macro-cracks of PMMA were generated from the edge and graphene near the PMMA crack tip contained many micro-cracks due to crack tip strain concentration. In contrast, graphene far from the macro-crack of PMMA has fewer and smaller micro-cracks. ....	112
Figure A5: Additional micrograph of Gr/PMMA on a 3M Tegaderm tape at 16% of applied strain. ....	113
Figure A6: Additional micrograph of Gr/PMMA on a 3M Tegaderm tape at 16% of applied strain. ....	114
Figure A7: A global view of a Gr/PMMA ribbon on a 3M Tegaderm tape at fracture (18% of applied strain). Many macro-cracks transverse to the stretching direction is visible. ....	114
Figure A8: Loading and unloading tests on a Gr/PMMA ribbon supported by a 3M Tegaderm tape at different applied strains. The inset displays the zoomed-in view for the case when loading up to 3% and unloading. ....	115
Figure A9: Loading and unloading tests on the bridged Gr/PMMA supported by a 3M Tegaderm tape at different applied strains. ....	116
Figure A10: The thickness of diluted PI depending on spin-coating speed. ....	117

Figure A11: Stretchability of 750-nm-thin Au/PI. Each orange line indicates a different experimental trial. ....	118
Figure A12: The stretchability of 300-nm-thin serpentine GET. Each black line indicates a different experimental trial. ....	119
Figure A13: EDA measurement. a-d) EDA data from different human subjects (#2 - #5, respectively).....	120
Figure A14: EDA long-term monitoring data. a) Long-term wearability test on subject #6. Ag/AgCl gel electrodes were not replaced after delamination. b) Another long-term wearability tests. This time, GET was encapsulated by a 47- $\mu$ m-thick overlay (Tegaderm, 3M).....	121

## Chapter 1: Introduction<sup>1,2,3</sup>

Next-generation wearable electronics are expected to be high-performance, multifunctional, and imperceptible to wear. Although wearable platforms such as epidermal electronics have been built using conventional electronic materials, such as metals and semiconductors, the fabrication process, thickness, performance, and cost require further improvement. The superior electrical, mechanical, and photonic properties of 2D materials and their composites have afforded many recent advancements towards transparent, micron-meter-thin, intrinsically soft, and stretchable wearables. This chapter provides a survey for emerging 2D-materials-based wearable electronics with a special focus on their design, fabrication, characterization, and applications. First, an overview of 2D-materials-based wearable electronics is presented in comparison to non-2D-materials-based wearables. Next, different types of manufacturing methods of 2D-materials-based wearables are briefly discussed. Then, I cover some of the mechanical and electrical characterization methods of the wearables and diverse applications as wearables with the emphasis on the strain and electrophysiological sensors among others. As numerous 2D-materials-based strain sensors have been reported in the literature, I offer a thorough comparison by listing their fabrication methods, device thickness, stretchability, and gauge factors in one table. For electrophysiological sensors, I underscore the concept of imperceptible electronics because wearable devices made by 2D materials can be both mechanically and optically imperceptible. Finally, I conclude this chapter by providing a scope of research that includes the structure of the overall discussions.

---

<sup>1</sup>H. Jang, H. Jeong, Z. Dai, J. Barber, and N. Lu, 2D Materials Based Wearable Electronics, 2D Materials and Applications, In Preparation, May 2022.

<sup>2</sup>S. Liu, Y. Rao, H. Jang, P. Tan, and N. Lu, Strategies for Bio-Conformable Electronics, Matter, 5, 4, 1104-1136, 2022.

<sup>3</sup>D. Kireev, S.K. Ameri, A. Nederveld, J. Kampfe, H. Jang, N. Lu, and D. Akinwande, Fabrication, Characterization and Applications of Graphene Electronic Tattoos, Nature Protocols, 16, 2395-2417, 2021.

## 1.1 OVERVIEW OF 2D-MATERIALS-BASED WEARABLES

Recent wearable electronics have demonstrated a growing promise in various biotechnology applications that could mimic the properties and functions of human skin, and beyond [1–3]. Also, small form factors and mobility of the wearable electronics enable more facile human-machine interface (HMI) [4–8] and comfortable monitoring of human health [9–11] for all range of people including patients and athletes. Furthermore, wearable electronics have been trying to reach comparable performance to the bulky medical-grade instruments, and potentially replace them in near future. However, conventional wearables are possessing the following limitations: 1. Bulkiness (obstructive to wear, not flexible or stretchable, non-conformal to the skin, and not possible to cover a large area), 2. Modality (e.g., Holter is just for ECG, and smartwatches just have a fixed sensing capability), 3. Long-term wearability (constant high quality of signals, skin breathability, data storage, and power consumption), and 4. Cost (materials, manufacture). In other words, we have challenges for improving current wearables in many perspectives, and there has been significant progress to solve those challenges by enhancing materials, engineering mechanics, integrating multi-functionalities, and developing manufacturing methods [10,12–21].

In particular, advancements of sensing materials and structural designs have significantly improved the performance of human health/motion monitoring sensors [2,10,22–25], soft robotics [26–28], etc. [17,29] To achieve such a performance on soft human skin without obstructiveness, the stretchability and the thinness of the device are important factors among others. For example, the wearable devices, such as electronic-skins (E-skin) and strain sensors, need to be stretchable to accommodate various amounts of strains depending on the location of the body, up to 30 - 40% of strain [30,31]. Also,

wearable devices, especially those made for measuring biometrics on human skin including electrophysiological (electrocardiogram (ECG), electromyogram (EMG), and electrooculography (EOG)) and biochemical sensors, need to make a conformal contact to the skin to accurately capture the signals and reduce motion artifacts [32]. Moreover, wearable sensors call for mechanical imperceptibility so that continuous long-term monitoring would be achieved without discomfort.

Figure 1.1 illustrates a schematic of the stretchability and the thinness of several wearable electronics based on both 2D materials and non-2D materials. However, it should be noted that the definition of the stretchability varies slightly since each paper conducted tensile testing differently (i.e., whether conductive material is clamped together with the substrate or not) and defined the allowable maximum signal change under deformation distinctively according to their application or criteria. Conventional materials, such as metals and semiconductors, can achieve high stretchability up to ~50% when they are thinned down to less than sub-micron-meter and patterned to a nanomesh [33] or a serpentine [34].

Furthermore, the serpentine-shaped gold on a PET substrate [35] and the wrinkled gold film [36] can be stretchable over 100%. However, their sensitivity is poor, and the fabrication process is either expensive or time-consuming. Hydrogels [37–42] are the most stretchable material. Cai *et al.* introduced the SWCNT/hydrogel-based strain sensor, which can measure up to 1000% of strain [38]. However, hydrogel-based sensors are thick (~ few mm) in general and contain dehydration issues. Liquid materials, such as liquid metal and liquid ions [43–49], have a superior stretchability over 800% [46] and durability with negligible hysteresis over a few hundreds of cyclic strains. However, similar to the hydrogels, their thickness is typically in mm, which prevents the device from being affixed to the skin conformably. Furthermore, semiconductive (e.g., P3HT) and conductive

organic materials (e.g., PEDOT:PSS), are known to be transparent and stretchable but have a low intrinsic stretchability. Therefore, elastomers [50–52] and enhancers (e.g., STEC [53] or AgNWs [54]) are often being mixed with the organic materials to improve the stretchability. Consequently, it makes wearable electronics based on those composites become thicker and opaque. However, interestingly, Ershad *et al.* introduced an Ag + PEDOT:PSS ink which can be drawn directly on the skin and has submicron-thickness and stretchability up to 30% of strain [55]. Both the thinness and high stretchability can be also achieved by the materials with percolation networks, such as CNTs-based and AgNWs-based elastomers [56–60,61–64]. However, in most cases, the sensitivity of those sensors (i.e., gauge factor (GF)) is low.

To identify the material with superior performance, stretchability, and ultrathinness, an extensive effort has been made towards the wearable devices based on 2D materials and their derivatives, such as chemical vapor deposited (CVD) graphene [4,32,65–70,70–78], graphene nanoplatelets (GNP) [79–85], reduced graphene oxide (rGO) [86–97], graphene woven fabrics (GWFs) [98–103], molybdenum disulfide (MoS<sub>2</sub>) [104–106], MXenes [5,107–109,109–113], hybrid materials (2D materials + other nanomaterials) [7,114–124], etc. [125–138] due to their superior and unique properties including but not limited to ultrathinness, imperceptibility, low contact impedance, piezoelectricity, ballistic charge transportation, multi-functionality, and large surface-to-volume ratio [139–142]. Graphene, transition metal dichalcogenide (TMD), and MXenes are the 2D materials highly utilized as a key material in wearable electronics and particularly graphene has been applied the most due to the enabled large-scale production [74,143–145] and the easily-tunable electrical and mechanical properties [141,146]. Furthermore, outstanding electrical, mechanical, and photonic properties demonstrate a great potential of 2D materials to serve as versatile materials to attain superior device performance for diverse

applications [21,147]. Figure 1.2 describes some of the key mechanisms and their corresponding applications of the 2D materials for wearable electronics. 2D-materials-based noninvasive soft electronics successfully demonstrate on-skin applications, including 1) strain sensors, 2) pressure sensors, 3) electrophysiological sensors, 4) biochemical sensors, 5) optoelectronic/photonic sensors, and 6) energy storages and energy harvesters.

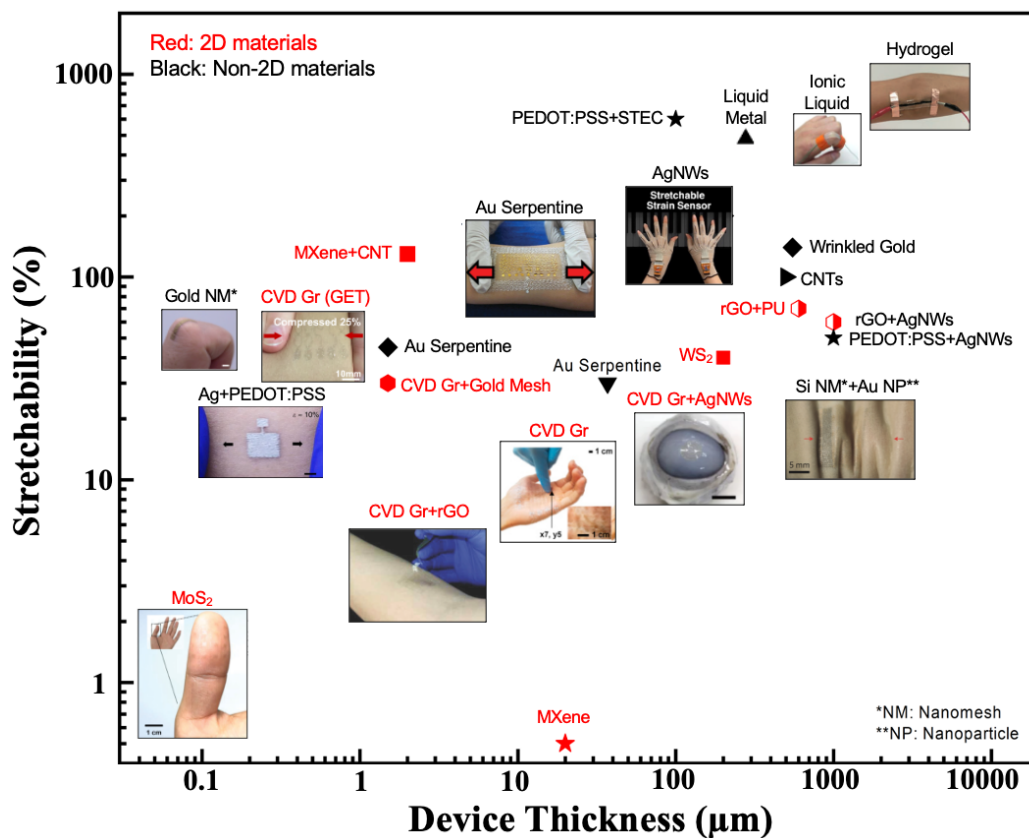


Figure 1.1: An Ashby plot of the stretchability and the thickness of soft wearable electronics based on 2D materials and non-2D materials [6,32–36,38,41,46,53,54,62,65,66,94,105,107,116,117,148–153].

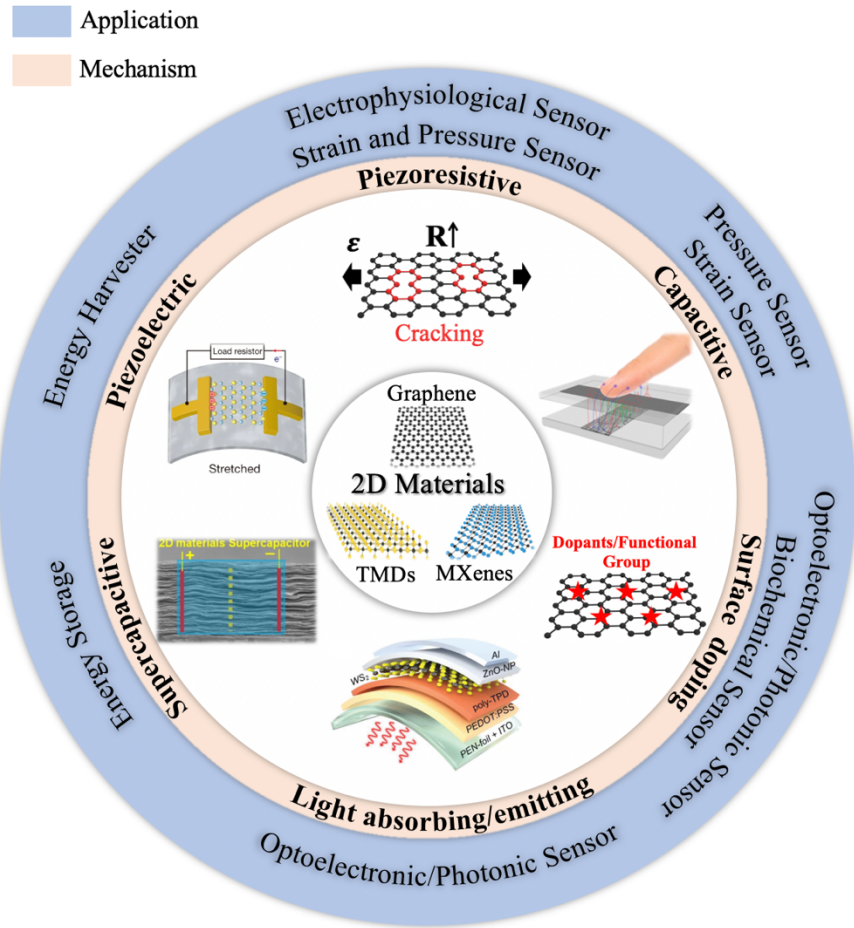


Figure 1.2: Various types of mechanisms and corresponding applications of 2D materials for wearable electronics [13,117,154–156].

## 1.2 DESIGN

The softness of wearable electronics is one of the most important requirements for long-term and unobstructive monitoring of biosignals on the skin. Regardless of the material's intrinsic softness or stiffness, the materials can be patterned into stretchable structural designs. Patterning intrinsically stiff materials into specific geometries or shaping them into specific structures may significantly reduce their effective stiffness. The

earliest approach was to fabricate periodically buckled ribbons or membranes by harnessing mechanical instability [157,158]. Later, deterministically formed 3D pop-up structures enabled 3D integration between soft electronics and tissue scaffolds [159]. With encapsulation, these structures can achieve biocompatibility regardless of material composition. However, a big limitation of out-of-plane buckled structures is that they may cause mechanical irritation in long-term applications if the device is not structurally well designed. As a result, buckled, pop-up or kirigami designs are not widely used in bio-conformable electronics. Instead, serpentine, fractal, and mesh designs are preferred structures due to their negligible out-of-plane deformation and low bending stiffness.

Serpentine design, i.e., 2D meandering ribbon design, for stretchable electronics was first proposed in 2004 [160]. In 2005, Li *et al.* pointed out that the elongation of a serpentine ribbon can be accommodated by in-plane rigid body rotation as well as minor out-of-plane buckling (Figure 1.3a) [161]. The introduction of serpentine ribbons opened up a new paradigm for stretchable electronics. A plethora of mechanics models have been built to predict the stretchability and effective stiffness of serpentine ribbons based on their geometric parameters (e.g., width-to-radius ratio, length-to-radius ratio, and crest angle) [162]. At first, serpentine ribbons were just used as interconnects linking rigid functional “islands”. Examples include stretchable batteries [163], integumentary cardiac monitoring devices, and hydration sensor arrays (Figure 1.3b) [164]. A major limitation of the serpentine-plus-island design is that the rigid islands still locally limit the conformability and the stretchability [165]. Here, conformability means the effective contact area of a membrane to a wavy surface of the skin, which can vary from 0 (nonconformed) to 1 (fully conformed). One remedy is to also pattern the functional materials into a filamentary serpentine network to eliminate the islands, a strategy used in epidermal electronics (Figure 1.3c) [166], stretchable piezoelectric sensors [167], epicardial electrodes [168], graphene

e-tattoos [169], and even glass-based stretchable photonics (Figure 1.3d) [170]. However, serpentine designs suffer from limitations such as small areal coverage and difficulties associated with miniature devices or a large number of channels.

Fractal [171,172] and hierarchical designs [164,173] involve more advanced serpentine patterns that offer higher stretchability and areal coverage than simple serpentine patterns. Figure 1.3e shows a hierarchical serpentine, consisting of one large, primary serpentine constructed from many smaller, secondary serpentine patterns [163]. Its stretchability can reach 350% due to the multi-stage unraveling of the primary and secondary serpentine patterns, as shown in the figure. Moreover, compared to basic serpentine patterns, fractal serpentine patterns can significantly increase areal coverage, which is useful for minimizing the contact impedance between metallic electrodes and bio-tissues, as shown in Figure 1.3f [174]. However, fractal and hierarchical serpentine patterns often have compromised reversibility after large deformation, hence are more suitable for applications involving one-time stretching (e.g., fitting on a curved surface and staying in that shape). Correspondingly, it is also challenging to handle fractal structures during the transfer printing process.

Mesh design involves patterning a sheet of a functional material or device into a meshed network, often with serpentine-shaped building blocks (Figure 1.3g) [175]. The effective stiffness of the mesh structure can be orders of magnitude lower than that of the planar sheet. For example, a filamentary serpentine mesh of polyimide offers decent stretchability (up to 57%) and a low modulus ( $< 5$  MPa) at small strains [175]. The mesh design has been used in both skin-conformable and skin-mimicking electronics (Figure 1.3g), as well as epicardial sensors with organic electrochemical transistors (OECTs) [176]. Generally speaking, electrodes with mesh designs are not as stretchable and compliant as fractal electrodes but have more reversible deformation and lower resistance. For example, Li *et al.* demonstrated that a so-called “watchchain” structure provided 27% lower

resistance than an equivalent serpentine due to the redundancy in conductive pathways [177]. The mesh design can also be specifically engineered to match the nonlinear stress-strain behavior of human skin (Figure 1.3g) [175].

Kirigami design is an emerging structure used in bio-conformable electronics. By adding periodic cuts in a sheet, as shown in Figure 1.3h, the kirigami design can be stretched up to 140% with minor mechanical force [178]. Kirigami has been increasingly utilized in stretchable electronics because it can provide the largest areal coverage among all the stretchable designs [179]. The kirigami design has been used as integumentary electrodes on the heart or on the muscle [178,180]. A kirigami piezoelectric harvester has also been developed for energy harvesting on human body [181]. However, kirigami has not been widely applied in implanted electronics due to the risk of fracture at the tips of the cuts and the risk of damaging the tissue from any sharp corners.

In addition to patterned thin films, nanotubes or nanofibers with superior bendability in any direction can act as biosensors individually [182] or as a nanomesh [183]. Coaxial, twisted, or interlaced microfibers with diameters ranging from 10  $\mu\text{m}$  to 100  $\mu\text{m}$  can be assembled or woven into stretchable meshes [182]. For example, Zhong *et al.* twisted CNT fibers and polytetrafluoroethylene (PTFE) fibers together to assemble a fiber-based generator and wove it into a lab coat to power a wireless temperature monitoring wristband (Figure 1.3i) [184]. Lee *et al.* developed an ultrasensitive capacitive pressure sensor by interlacing two PDMS-coated conductive fibers [185]. However, the difficulty to fabricate the unique fiber structure is a tradeoff for its excellent mechanical properties [186].

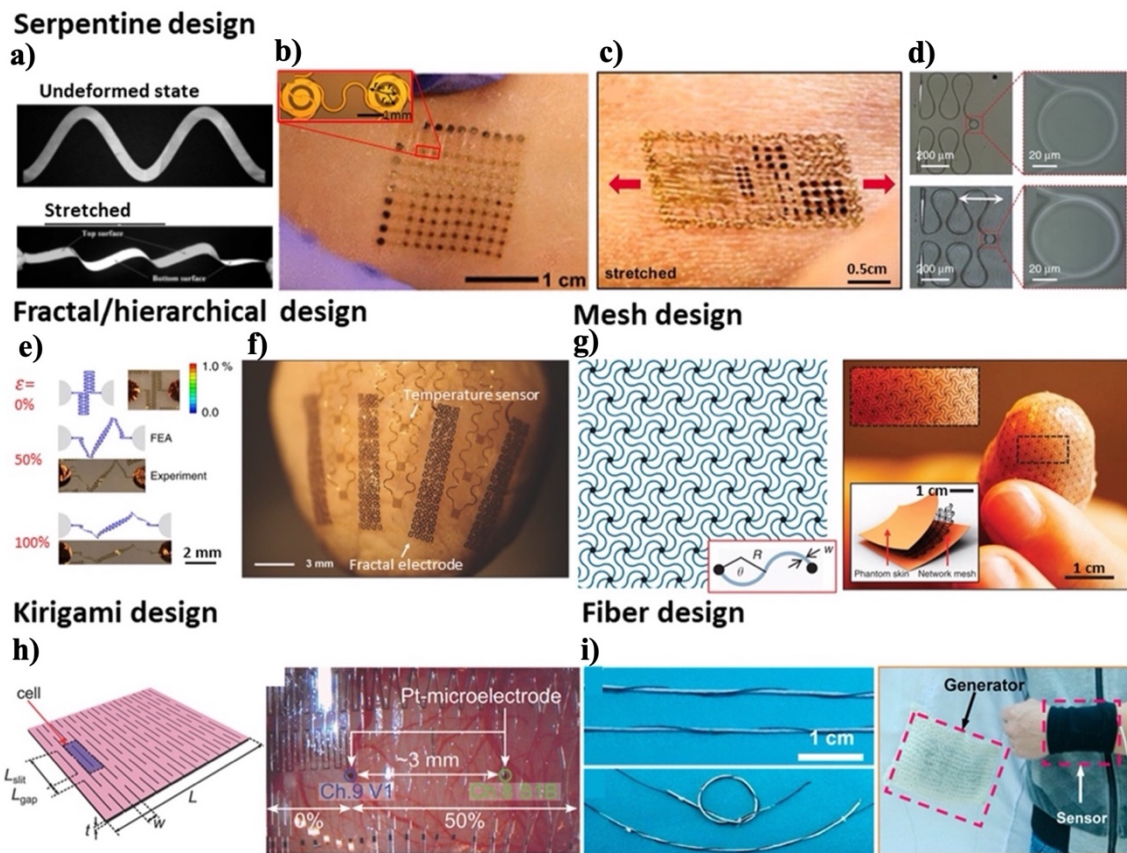


Figure 1.3: Examples of soft structures. [In Press, <https://doi.org/10.1016/j.matt.2022.02.006>] (a) A paper-cut serpentine ribbon and the ribbon buckled out-of-plane upon stretching [161]. (b) A stretchable hydration sensor array on skin with serpentine-plus-island design [164]. (c) A multifunctional epidermal electronic platform with both filamentary serpentine and serpentine-plus-island design [166]. (d) Micrographs of a glass-based stretchable photonic resonator in undeformed state (upper panels) and at 36% nominal tensile strain (lower panels) [170]. (e) Multi-stage unraveling of a hierarchical serpentine with fractal design under uniaxial stretching [163]. (f) Fractal electrodes and temperature sensors for epicardial electrotherapy [174]. (g) A serpentine mesh conformed to a fingertip [175]. (h) Geometric parameters of a kirigami design (left) and stretchable kirigami electrodes laminated on a mouse brain for visual stimulation (right) [178]. (i) A fiber-based generator woven into a lab coat to power a wireless temperature monitoring wristband [184].

### 1.3 FABRICATION

Diverse manufacturing methods of wearable electronics have been developed considerably due to the high demand for time- and cost-efficient and high-throughput manufacturing. In general, the manufacturing methods can be categorized but not limited to 1. Conventional IC fabrication methods (photolithography process) [105,151], 2. Subtractive methods (blade cutting and laser cutting) [32,187], 3. Additive methods (inkjet printing, 3D printing, electrospinning, R2R printing, and spraying) [65,188–190], and 4. Laser scribing/ablation [14,191,192]. The photolithography process has been widely used as a standardized method for large-scale manufacturing. However, this method requires high-cost facilities and intensive labor. Therefore, many other manufacturing methods including subtractive and additive have been developed widely.

Figure 1.4 shows some of the representative examples of manufacturing methods for 2D-materials-based wearable electronics, especially the ones which have on-skin applications. Figure 1.4a illustrates a fabrication method of the graphene electronic tattoo (GET) using a blade cutting, an example of subtractive methods [32]. In this work, Kabiri Ameri *et al.* used the so-called “wet transfer, dry patterning” fabrication process for GET, which is more cost and time effective than the conventional photolithography process. To fabricate a serpentine-shaped GET device, an inexpensive programmable mechanical cutter (Silhouette Cameo) was used [32]. Furthermore, to achieve higher resolution and time efficiency, laser cutting (such as using UV laser) can be utilized instead of a mechanical cutter, which I used for my research projects listed in Chapters 4 and 5.

As one of the examples of additive methods, inkjet printing method is easily accessible for prototyping and commercialization of cheap electronic devices. This technique allows small volumes of ink, typically about in picolitres, to be deposited with an expeditious and precise process of patterning [193]. Figure 1.4b describes a schematic

of the inkjet printing of wearable e-textile using reduced graphene oxide (rGO) inks, which can monitor heart rate [188]. For inkjet printing using metal-based inks has a choice limitation for the substrates due to the high-temperature sintering process in general. However, Karim *et al.* introduced graphene-based inks which resolved this issue and even could be inkjet-printed on a textile. Since all the fabrication process is operated at low temperature ( $< 100^{\circ}\text{C}$ ), heat-sensitive fabrics will not be damaged [188]. For the fabrication of e-textiles, inkjet printing can offer reduced material waste and water utilization by depositing the materials only at the desired locations in the fabric [194]. Furthermore, the additive printing technology also allows a large-scale fabrication of 2D-materials-based wearables via roll-to-roll (R2R) printing technology. For example, Chandrashekar *et al.* developed an R2R “green” method, which implies metal etching free, no polymer residue, eco-friendly and economic, to manufacture a wearable triboelectric nanogenerator using CVD graphene [189]. This method can potentially lead to the industry-level manufacturing of graphene-based wearable devices.

Another attractive manufacturing method of graphene-based wearables is by using laser scribing/ablation. Laser induced graphene (LIG) is porous graphene directly converted from polymers such as polyimide (PI) via infrared  $\text{CO}_2$  laser, visible laser, and ultraviolet laser [195–197]. It enables a facile fabrication of graphene-based wearables with eco-friendliness, tunable compositions, and controllable morphologies [14]. Figure 1.4c shows some of the representative schematics of fabrication methods for the LIG. Figure 1.4c-(i) demonstrates a low-cost and portable laser system using 450 nm laser to produce a LIG and the LIG-based wearable device was used as an artificial throat that can both emit and detect sound on a single device [191]. Additionally, Figure 1.4c-(ii) depicts a UV laser direct writing of porous graphene on PI fabrics to manufacture a wearable strain sensor [198]. The performance of the strain sensor was affected by the formation of LIG controlled

by the laser fluence, and as-fabricated LIG has a low sheet resistance of  $20 \Omega/\text{sq}$  and a maximum gauge factor (GF) of 27 [198].

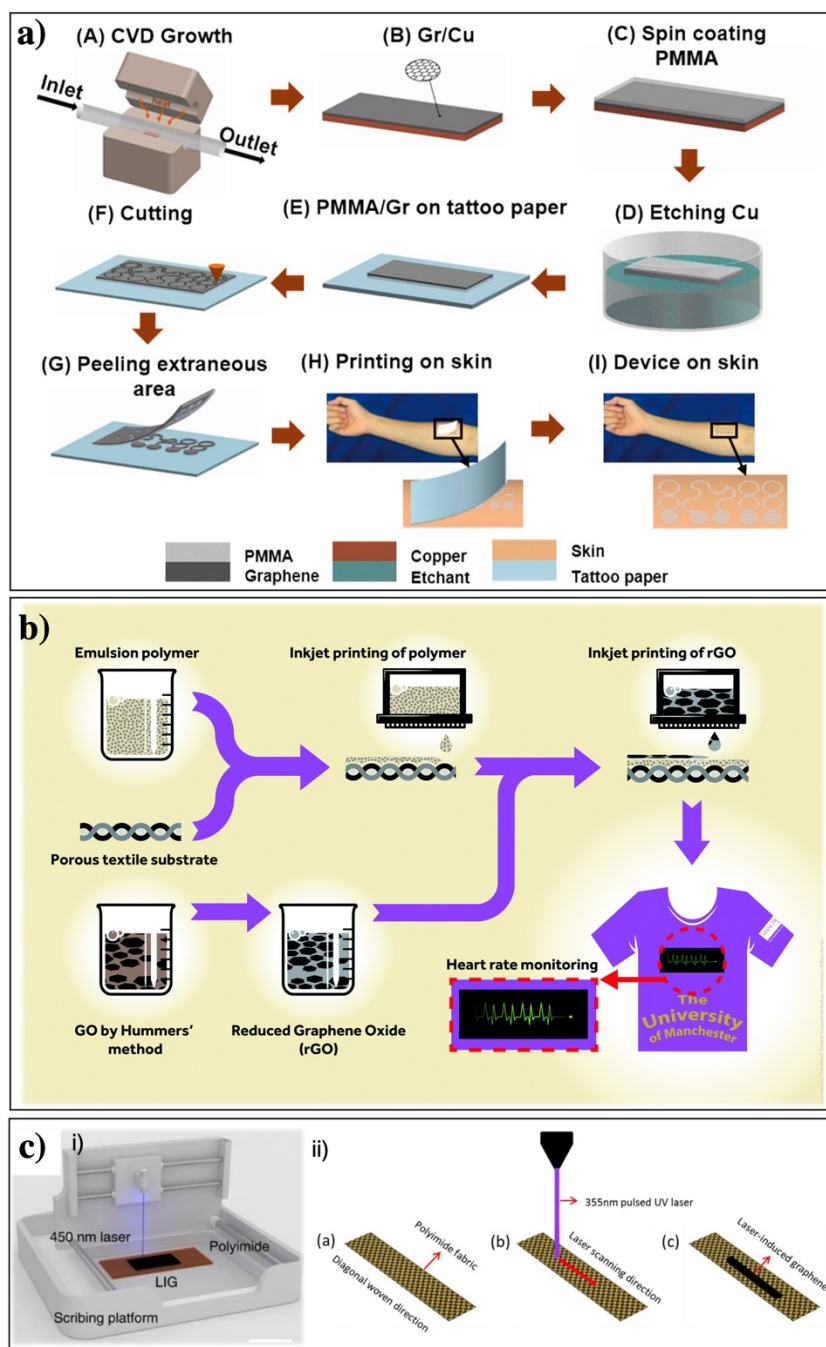


Figure 1.4: Manufacturing methods of 2D-materials-based wearable electronics. (a) “Cut-and-paste” method for graphene electronic tattoos (GET) sensors [32]. (b) Inkjet printing of rGO on a textile [188]. (c) i) Laser-induced graphene on a polyimide substrate [191] and ii) Laser-induced graphene on a polyimide textile using UV laser [198].

## 1.4 CHARACTERIZATIONS

Depending on the sensor applications, characterizations of the wearable sensor should be performed to unveil its mechanical, electrical, optical, and chemical properties. Among them, mechanical characteristics such as stretchability are the inevitably required property since the sensors will be placed on the soft skin. Therefore, I focus to discuss characterizations of mechanical and electrical (or electromechanical) properties by taking examples of strain sensors.

Basic sensing mechanism of the strain sensor is as follows. While a conductive material is geometrically deformed, the changes of electrical resistance are measured and the gauge factor (GF), the normalized changes of the resistance over strain, is calculated to indicate the sensitivity. However, the strain gauges based on conventional materials, such as metals and semiconductors, have very low stretchability and their sensitivities are very poor ( $GF \sim 2$ ) [101,199,200]. Recently, low dimensional materials including 1D materials and 2D materials have been introduced, but it has been still challenging to attain both high sensitivity and large stretchability. To obtain a high sensitivity (i.e., to obtain a large change of the electrical resistance over strain), the conductive material must be disfigured significantly at small strain, which leads to lower stretchability. In other words, there exists a compensation between sensitivity and stretchability.

To work as a strain sensor, 2D materials are supported by a polymeric substrate or mixed with a polymer due to their ultra-thinness. Therefore, the thickness of the device is mostly determined by the thickness of the polymer. Typical polymers used for wearable strain sensors are elastic and biocompatible, such as Polyimides (PI), Polydimethylsiloxane (PDMS), and Ecoflex<sup>TM</sup>. The majority of the stretchable and wearable strain sensors possess the sensing mechanism of either resistive type or capacitive type [25]. Although capacitive-type sensing provides high stretchability, linearity, and low hysteresis, in

general, capacitive-type strain sensors have the theoretical sensitivity limit (i.e.,  $GF \leq 1$ ) [25]. Also, the output signals from strain and pressure should be decoupled for the capacitive-type sensors. Hence, most of the strain sensors are employing the resistive-type sensing mechanism. Mostly, the gauge factor is not constant over the measurable strain range and the highest gauge factor is reported. Typical CVD-graphene-based strain sensors have gauge factors less than 100 [67,68,121,133]. However, different form factors of CVD graphene such as graphene woven fabrics [103] and graphene foam [133] can provide much higher gauge factor and stretchability to the strain sensor. Furthermore, the graphene with an eccentric geometry, graphene fibers and yarns, and graphene inks grant the better performance of the device compared to the non-patterned graphene. For example, the mesh-type strain sensors based on graphene nanoplatelets [85] and CVD graphene [103] show an extremely high gauge factor of  $> 10^4$  and  $> 10^6$ , respectively. Moreover, a strain sensor based on a graphene/silver nanoparticle synergic conductive network and sandwich structure demonstrates the stretchability of the sensor over 1000% of strain [124]. In terms of higher stretchability with linearity and reversibility, the strain sensors based on hybrid structures are superior to the one with 2D materials only, although the gauge factor is comparably low [121].

## **1.5 APPLICATIONS**

Over decades, many applications of wearable sensors have been developed including but not limited to strain sensors, pressure sensors, electrophysiological sensors, biochemical sensors, optoelectronic and photonic sensors, and energy storage and energy harvesting modules. In this section, I focus on strain sensors and electrophysiological sensors based on 2D materials since my research is mainly about defining stretchability and performance as an electrophysiological sensor.

### 1.5.1 Strain Sensors

Strain sensors are one of the most accessible applications of wearable electronics. In Figure 1.5, we introduce some of the representative strain sensors based on different material types and their corresponding mechanisms and performances. Figure 1.5a shows the all-graphene-based strain sensor [68]. Single-layer graphene (SLG) grown by CVD was used as an active material, and graphene flakes (up to 3 layers) were used as an electrode. To obtain higher stretchability and gauge factor, SLG was directly patterned on a copper sheet. The sensing mechanism is based on the change of resistance by the geometrical variations of the SLG pattern, and it is bidirectionally stretchable up to 20% [68]. Since SLG has been utilized in the strain sensor, it can achieve high transmittance and the sensing capability of the infinitesimal strain.

Unlike the simple layer structure of the active material, the 3D-shaped graphene layer named the fragmentized graphene foam (FGF) was introduced as a strain sensor (Figure 1.5b) [133]. The graphene foam was fabricated by CVD, and the graphene foam was fragmentized by a vortex mixer and rearranged on a PDMS. The graphene foam has 200 – 300  $\mu\text{m}$  sized fragments, and they construct a percolation network [133]. Then, the change of contact resistance was measured when the strain sensor was stretched. Since it utilized the mechanism of a percolation network, the gauge factor was not high ( $\text{GF} = 15 - 29$ ) [133]. However, it provided high stretchability over 70% and durability of 10,000 cycles at 50% of strain [133].

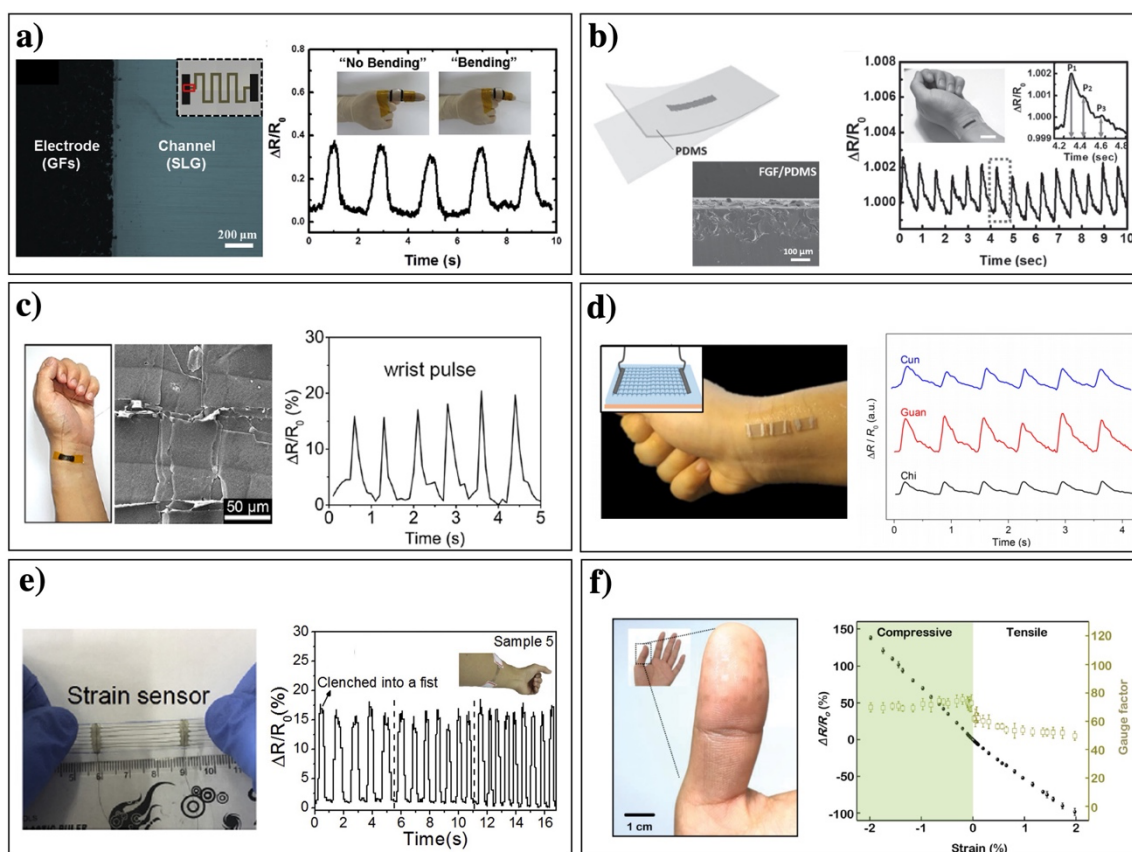


Figure 1.5: 2D-materials-based strain sensors. (a) Strain sensor based on single-layer graphene and the demonstration on the finger [68]. (b) Highly stretchable and sensitive strain sensor using fragmented graphene foam and the demonstration on the wrist [133]. (c) High-performance strain sensor with fish-scale-like graphene-sensing layers on the wrist [90]. (d) A wearable strain sensor for precise home-based pulse wave monitoring on the wrist [103]. (e) Carbon/graphene composite nanofiber yarns for highly sensitive strain sensors and the demonstration on the forearm [123]. (f) MoS<sub>2</sub>-based strain sensor on the thumb and the output signals and gauge factor over strain [105].

Liu *et al.* demonstrated another type of strain sensor possessing a unique structure of the reduced graphene oxide (rGO) with a “fish-scale-like structure” (Figure 1.5c) [90]. To create this structure, they employed a very simple, low-cost, energy-saving, and

scalable method. There were two layers of rGO film where the first rGO film on the elastic tape was stretched to 50% and another rGO film was transferred and stretched to 100%, then finally released the film so that the slices of rGO could be overlapped each other [90]. The rGO slices created a percolation network up to 60% of strain, and the change of contact resistance was measured [90]. After 60% of strain, the rGO slices were disconnected and cracks were produced, which induce a non-linear trend of the signal measurement [90]. The stretchability of the sensor was 82% and the gauge factor was varying from 16.2 to 150 [90].

Figure 1.5d introduces graphene woven fabrics (GWFs) based strain sensor where CVD graphene was deposited on a copper mesh [103]. The GWFs were supported by 100  $\mu\text{m}$ -thick PDMS substrate and the resistance change due to the crisscross morphology and crack propagations was measured. Because of this sensing mechanism, extremely high gauge factor was obtained (i.e.,  $\text{GF} = 500$  (0-2% strain),  $10^3$  (2-6% strain), and  $10^6$  (>8% strain)) [103]. Also, the sensitivity and the linearity of the sensor depend on Young's modulus of PDMS. Stiffer PDMS provides lower sensitivity but higher linearity due to more buckle-delamination [103]. The optimized strain sensor allowed precise pulse monitoring and the three signature locations of the pulse (Cun, Guan, Chi) were measured and distinguished properly (Figure 1.5d).

The fibers and yarns are other types of 2D materials-based composites which grant a scalable fabrication typically using electrospinning. To synthesize them, 2D materials are added to a polymer matrix. Yan *et al.* demonstrated the strain sensor consisting of carbon/graphene composite nanofibers yarns (CNYs) (Figure 1.5e) [123]. To obtain higher conductivity, stretchability, and stability, carbon/graphene composite was added to thermoplastic polyurethane (TPU) matrix to fabricate nanofiber yarns. The resistance of the strain sensor was changed due to the cracks on the surface of CNYs. The gauge factor

was very high ranging from 277 to >1700, and it depends on the number of the nanofibers [123].

Although most of the 2D-materials-based strain sensors use graphene as an active material, a semiconducting atom-thick crystal, molybdenum disulfide ( $\text{MoS}_2$ ), has been fabricated as a transparent, sensitive, and wearable strain sensor (Figure 1.5f) [105]. The  $\text{MoS}_2$  was grown with the CVD method and a patterned graphene electrode was used to receive the resistance change from  $\text{MoS}_2$ . The overall sensor is ultrathin (only 75nm), so it conforms and adheres to the skin completely without any aid of adhesives. Because of the piezoresistivity of  $\text{MoS}_2$ , a reversible resistance change was measured up to -1.98% of strain [105]. At higher strain up to -5.98%, an irreversible non-linear change of the resistance was measured due to the crack generations [105]. Under the tension and compression of the sensor, the gauge factor was consistent to be -56.5 and -72.5, respectively [105].

### **1.5.2 Electrophysiological Sensors**

Compared with conventional wearable electrodes, 2D materials have unique mechanical (robustness, ultrathin, ultralight), electrical (the thinnest conductive material), electrochemical (stable and biocompatible), and optical (transparent) advantages [32]. Hence, although its research and development history are relatively short, numerous promising 2D-materials-based flexible electronic devices have been reported for electrophysiological applications [201]. Various types of 2D-material-based electrodes have been demonstrated with different materials including rGO coated textile [91,188], platinum-based two-dimensional dichalcogenide (Pt-TMDs) [187], graphene electronic tattoo (GET) to allow such electrodes can fully conform to a natural skin morphology without artificial adhesives and acquire an improved signal to noise ratio (SNR) [4,32].

Designs of electrophysiology sensing electrodes based on 2D materials have mainly involved the printing of a conductive solution on flexible/stretchable substrates. This allows for conformal coating of a conductive 2D-material layer on polymer substrates [4,187,202], paper [203], or textiles [91,188] by printing conductive solutions or metal deposition methods. Figures 1.6a and 1.6b show an example of graphene-based textile electrodes for ECG monitoring. Yapici *et al.* proposed a simple and scalable fabrication method whereby conductive textiles are formed by dipping nylon fabric into an rGO solution followed by a thermal treatment as shown in Figure 1.6a [91]. Karim *et al.* also reported graphene-based conductive patterns by inkjet-printing onto a pre-treated textile surface. The surface pre-treatment improved the sheet resistance of conductive patterns by three orders from  $1.09 \times 10^6 \Omega \text{ sq}^{-1}$  to  $2.14 \times 10^3 \Omega \text{ sq}^{-1}$  (Figure 1.6b) [188]. When comparing the ECG signals recorded using the graphene-based textile electrodes to conventional Ag/AgCl electrodes, a slight variation in baseline can be observed Graphene-clad textile electrodes for electrocardiogram monitoring [91], which could be induced by motion-related artifacts due to a lessened degree of conformability between the electrodes and skin.

Ameri *et al.* demonstrated graphene electronic tattoo (GET) sensors which are designed as serpentine and fabricated by “wet transfer, dry patterning.” The main advantages of GET are its mechanical properties and functionality. As sub-micrometer-thick transparent stretchable electrodes ( $463 \pm 30 \text{ nm}$  thickness, around 85% transparency, and more than 40% stretchability) GET can fully conform to the skin and follow arbitrary skin deformation without experiencing any mechanical failures, while measuring multimodal electrophysiological biometrics including EEG, ECG, EMG [32], and EOG [4] as shown in Figure 1.6c.

Later, a large-scaled, low-temperature growth (400°C) platinum diselenide (PtSe<sub>2</sub>) and platinum ditelluride (PtTe<sub>2</sub>) layered materials feature four times lower impedance and almost 100 times lower sheet resistance compared to monolayer graphene tattoos [187]. Figure 1.6d shows its diverse applications including ECG, EMG, EEG, EOG, and temperature measurements. Mechanical patterning process followed by transferring to a conventional medical tape (Tegaderm) allows for tattoo-like form factor and monitoring human physiological vital signs on the skin, which is comparable signal quality to a conventional Ag/AgCl gel electrodes as shown in Figure 1.6d [187].

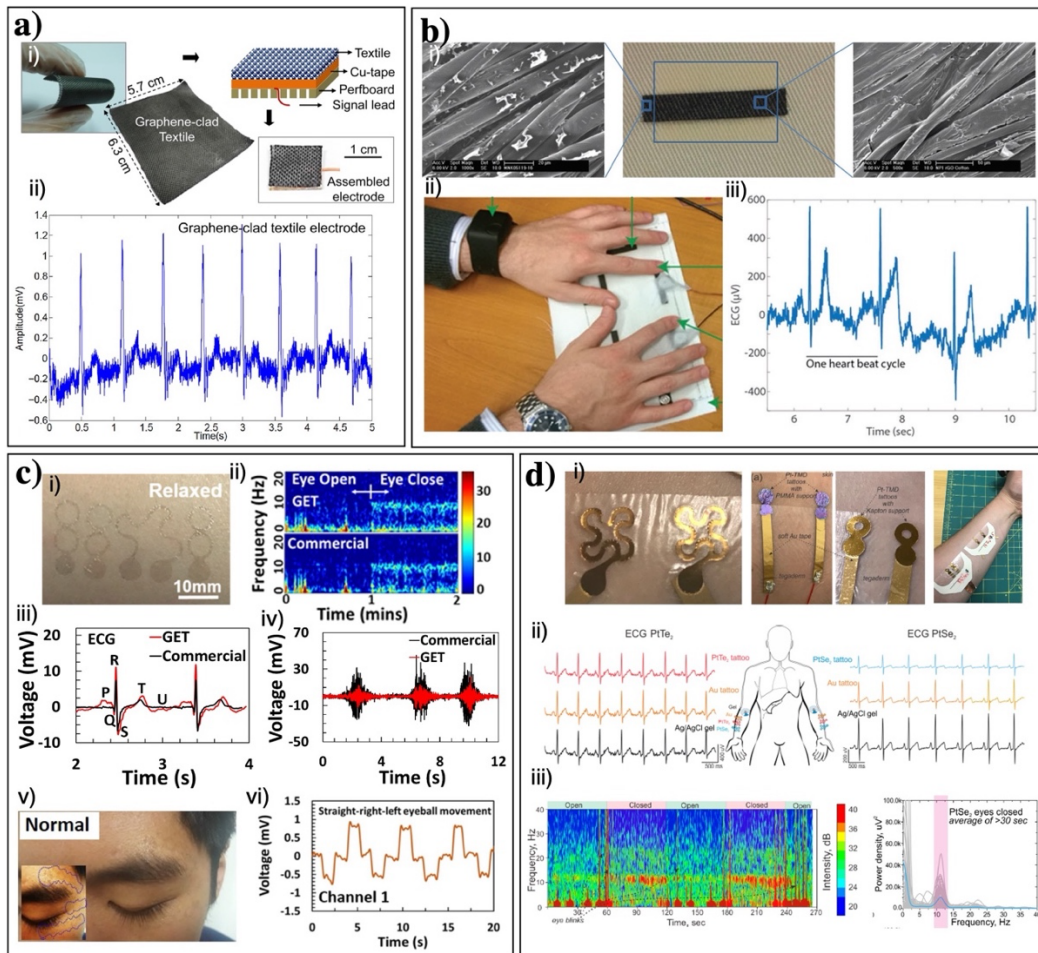


Figure 1.6: 2D materials in electrophysiology sensing applications. (a) Flexible nylon textile with rGO. (i) rGO coated sample for ECG testing, (ii) ECG signal obtained from graphene-clad textile electrode [91]. (b) Inkjet-printed graphene-based conductive patterns on textiles. (i) SEM images and a textile sample picture of the inkjet-printed rGO ink onto cotton fabrics, (ii) Experimental methods for measuring heart rate using graphene textile, (iii) Illustration of the measured ECG signal using graphene textile [188]. (c) Graphene electronic tattoo (GET) sensors for skin impedance, EEG, ECG, and EMG sensing. (i) GET on a relaxed skin, (ii) Measured EEG data from the GET mounted on the forehead, (iii) ECG on the chest, and (iv) EMG on the forearm [32], (v) GET EOG sensor worn around human eyes, (vi) Measured EOG signal recorded by GET EOG sensor [4]. (d) Pt-TMD tattoos based on platinum diselenide (PtSe<sub>2</sub>) and platinum ditelluride (PtTe<sub>2</sub>) layered materials for multiple vital sign measurements. (i) Pictures of Pt-TMD device on the skin with polymeric support, (ii-iii) Demonstration for ECG and EEG measurement with PtSe<sub>2</sub> and PtTe<sub>2</sub> electrodes [204].

## 1.6 SCOPE OF RESEARCH

2D materials are indeed an attractive choice for wearable electronics due to their exceptional mechanical, electrical, chemical, and optical properties. More specifically, the remarkable mechanical robustness and excellent electrical/thermal properties make graphene a promising candidate for future flexible, stretchable, and bio-integrated electronics. Yet, there exist more in-depth understandings of the failure mechanisms and the challenges to solve to make those graphene-based sensors to be more practical (i.e., a fully-integrated unobstructive and ambulatory wearable sensor). In Chapter 2, I first briefly introduce our previous innovation of sub-micron-thin graphene e-tattoos (GET), designed as filamentary serpentine and fabricated by a cost- and time-effective “wet transfer, dry patterning” method, and what has been achieved and validated by the GET as a wearable sensor. Next, I provide fundamental insight into the failure of ultrathin polymer-supported graphene (i.e., GET) and its electrical contacts, which is critical for designing future graphene-based soft electronics (Chapter 3). Furthermore, since various conductive overlayers need to directly laminate on graphene to make electrical contacts, I also investigate the mechanical reliability of CVD graphene when it’s interfaced with the overlayers (Chapter 3). In Chapter 4, to improve the venerable interface between GET and rigid back-end-circuits with orders of magnitude mismatch in mechanical stiffness, I introduce the idea of heterogeneous serpentine ribbons (HSPR), which refer to serpentine GET overlapping with a serpentine gold ribbon. Numerical and experimental analyses are used to validate the concept of HSPR. This method offers a remedy for the long-standing interconnect challenges between ultrathin sensors and rigid electronics. Based on the electromechanical characterizations of GET and the novel interface design of HSPR, I manufacture an unobstructive and ambulatory wearable sensor that can continuously monitor electrodermal activity (EDA) on the palm, where a challenging location to place

electrodes due to the frequent motions of hand but psycho-physiologically the most ideal site to monitor EDA (Chapter 5). Finally, conclusions and outlook are provided in Chapter 6.

## Chapter 2: The Invention of Graphene Electronic Tattoos (GET)<sup>4</sup>

In this Chapter, the overview of graphene electronic tattoos (GET) is briefly provided, which will be the foundation of my follow-up electromechanical analysis and sensing applications discussed in the rest of the Chapters. The major contents of this Chapter are reprinted with the permission from S.K. Ameri, R. Ho, H. Jang, L. Tao, Y. Wang, L. Wang, D. Schnyer, D. Akinwande, and N. Lu, Graphene Electronic Tattoo Sensors, ACS Nano, 11, 8, 7634-7641, 2017. Copyright 2017 American Chemical Society.

### 2.1 OBJECTIVE AND OVERVIEW

There exists a high demand for long-term wearable sensors with high-fidelity monitoring of biosignals, which have the potential to be applicable outside of hospital and lab settings to allow for comfortable ambulatory use, including mobile health care, fitness tracking, human-machine interactions (HMI), and so on [205,206]. However, conventional medical-grade devices are too bulky, uncomfortable to wear, expensive, and lack of the multi-functionalities. For example, traditional technologies for electrophysiological measurements use thick, flat electrodes, which are taped to the surface of the skin and have terminal connections to stationary data acquisition facilities.

To enable unobstructive, ambulatory, high-fidelity, and long-term monitoring of biosignals, we invented a graphene electronic tattoo (GET), a chemical vapor deposited (CVD) graphene supported by a polymeric substrate, which has total sub-micron thinness ( $463 \pm 30$  nm), high optical transparency ( $\sim 85\%$ ), and a stretchability ( $\sim 40\%$ ). The GET can be easily transferred on human skin through a temporary tattoo paper and can fully conform to the micro-texture of skin via just van der Waals (vdW) forces. The open-mesh

---

<sup>4</sup>S.K. Ameri, R. Ho, H. Jang, L. Tao, Y. Wang, L. Wang, D. Schnyer, D. Akinwande, and N. Lu, Graphene Electronic Tattoo Sensors, ACS Nano, 11, 8, 7634-7641, 2017.

structure of the GET makes it breathable and its stiffness negligible. As a dry electrode, skin-to-GET interface impedance is comparable to medically used silver/silver-chloride (Ag/AgCl) gel electrodes. Furthermore, GET has been successfully demonstrated to measure electrocardiogram (ECG), electromyogram (EMG), electroencephalogram (EEG), skin temperature, and skin hydration.

## 2.2 MECHANICAL AND OPTICAL CHARACTERIZATIONS

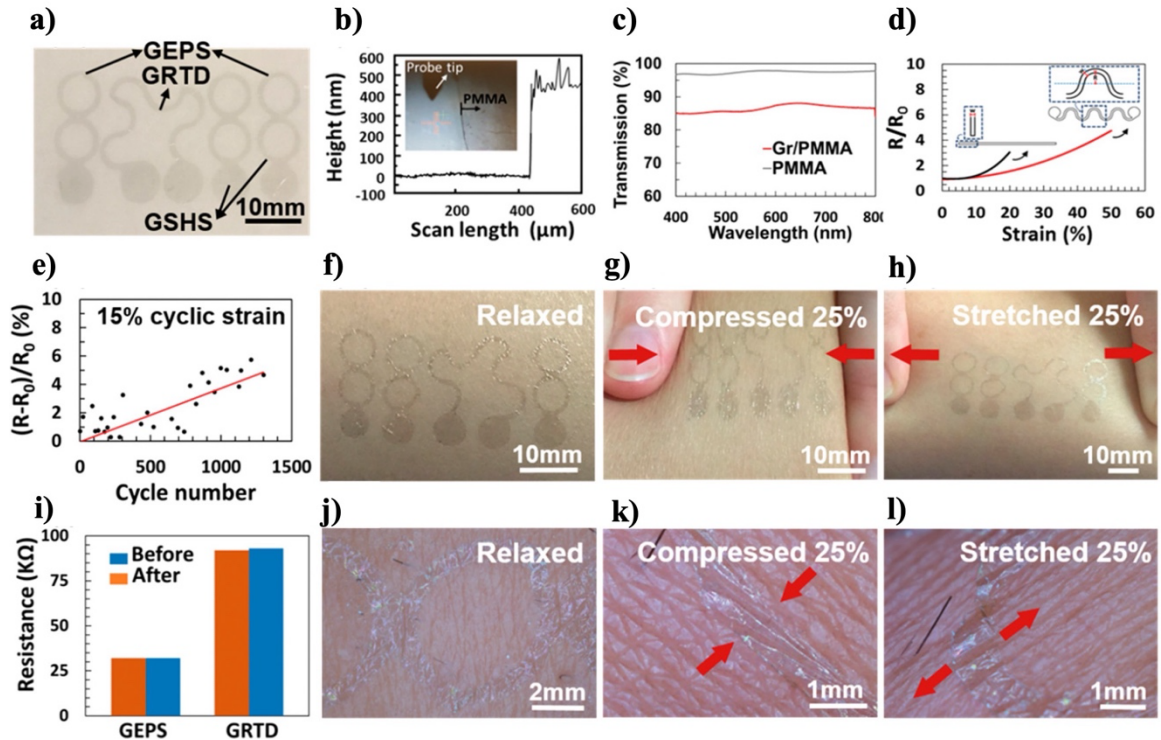


Figure 2.1: Mechanical and optical characterization of the GET [32]. (a) Picture of the as-fabricated GET with a white background, labeled with different sensors including graphene-based electrophysiological sensors (GEPS), a resistance temperature detector (GRTD), and a skin hydration sensor (GSHS). (b) The thickness of PMMA was measured by a profilometer to be  $463 \pm 30$  nm. (c) Optical transparency of bare PMMA and Gr/PMMA. (d) Normalized resistance of the GET versus applied tensile strain. The linear GET ribbon ruptures at 20%, whereas the serpentine-shaped GET can be stretched up to 50%. (e) Less than 6% change in GRTD resistance after 1300 cycles of 15% stretching. (f) GET mounted on skin. (g, h) GET on skin compressed and stretched by 25%, respectively. (i) Change in GEPS and GRTD resistance after all kinds of skin-tolerable deformations. (j to l) Magnified photographs of a GET on relaxed, compressed, and stretched skin, which demonstrate its full conformability even under skin deformation.

A picture of an as-fabricated Gr/PMMA-based GET is shown in Figure 2.1a, in which different types of physiological sensors are labeled: graphene-based electrophysiological sensor (GEPS), resistance temperature detector (GRTD), and skin hydration sensor (GSHS). The GSHS shares one electrode with the GEPS. The total thickness of the GET was measured to be  $463 \pm 30$  nm using a profilometer (Dektak 6 M Stylus) (Figure 2.1b). The optical transmittance of Gr/PMMA was measured by a Cary 5000 UV–vis–NIR spectrometer at five random spots over an area of  $2 \text{ cm} \times 3 \text{ cm}$ . The average transmittance of PMMA and Gr/PMMA in Figure 2.1c indicates that within the wavelength range of 400 to 800 nm the transmittance of bare PMMA is 96.5% to 98%, and the transmittance of GET is 84% to 88% due to additional light absorption by graphene.

The mechanical performance of the GET has been analytically modeled and experimentally measured. Neglecting the sub-nanometer-thin graphene layer, the bending stiffness of the GET is essentially that of the supporting PMMA substrate. With a reported Young's modulus of 3.3 GPa, the 463-nm-thick PMMA has a bending stiffness of  $2.7 \times 10^{-11} \text{ N} \cdot \text{m}$ , which is an order smaller than the bending stiffness of Au- based ultrathin epidermal electrodes (e.g.,  $3.49 \times 10^{-10} \text{ N} \cdot \text{m}$  for 100-nm-thick Au on 700-nm-thick polyimide) [207]. Besides superior flexibility, polymer-supported CVD graphene was reported to have fracture strains around 10%. By performing uniaxial tensile tests on Gr/PMMA with in situ electrical resistance measurement (Figure 2.1d), it is found that the linear Gr/PMMA ribbon ruptures at strains around 20%, while the serpentine-shaped Gr/PMMA ribbon remains electrically conductive up to a strain of 50%, which is well beyond the stretchability of human skin ( $\sim 30\%$ ) [208]. The mechanical stiffness of a freestanding GET serpentine ribbon (463 nm thick, 0.9 mm wide, and 2.7 mm in radius) is calculated to be 1.48 N/m according to our previous analytical models, which is less than half of that of the human epidermis (3.9 N/m) [151,209]. The performance of the GET

under a cyclic tensile strain of 15% is demonstrated in Figure 2.1e. The increase in resistance is within 6% after 1300 cycles (Figure 2.1e).

Figures 2.1f to h offer pictures and a video of the GET on relaxed human skin and skin subjected to various kinds of deformations. Electrical resistance of the GEPS and GRTD was measured before and after arbitrary skin deformation in Figure 2.1i, and no significant change could be identified. According to an analytical model we built previously, the GET has to be thinner than 510 nm to achieve full conformability with human skin [210]. With our GET thickness being just 463 nm, optical micrographs of it on skin (Figures 2.1j–l) confirm the ultra-intimate coupling between the GET and skin, even under severe skin deformation.

### 2.3 ELECTRICAL PERFORMANCE OF GET ON SKIN

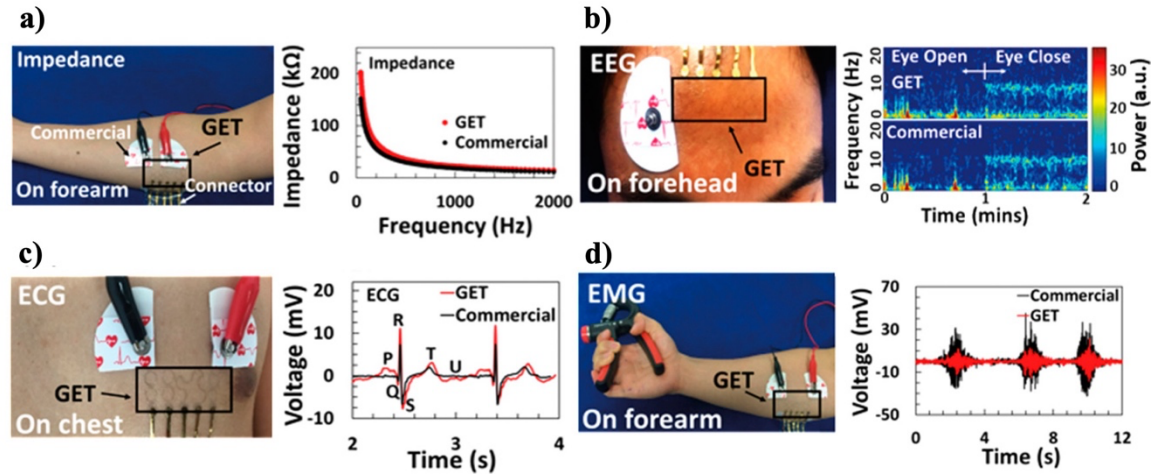


Figure 2.2: Electrical performance of the GET on skin [32]. (a) Without any skin preparation, GET–skin contact impedance is almost on par with that between commercial gel electrodes and skin. (b) EEG sensing on the forehead with both the GET and gel electrodes (left). When the eyes were closed, an  $\alpha$  rhythm of 10 Hz is visible in both spectrograms. (c) ECG measured synchronously by the GET and gel electrodes. Characteristic ECG peaks can be measured by both electrodes. (d) EMG sensing on the forearm with the GET and gel electrodes when the subject squeezed the hand exerciser three times.

Electrode–skin conformability directly dictates the contact impedance. Classical electrical circuit concepts suggest that the electrode–skin interface impedance is inversely proportional to the contact surface area [206]. Since conformal contact increases the effective contact area, it is therefore expected that interface impedance decreases. The GET–skin interface impedance was measured and compared with commercial Ag/AgCl gel– skin interface impedance, the latter of which is considered the gold standard for medical applications. The measurement was performed by laminating a GET on a human forearm without any skin preparation. The GSHS was connected to an LCR meter (Hioki

3532-50) using a customized flexible connector. A pair of Ag/AgCl gel electrodes were placed next to the GSHS with the same interelectrode distance, and the electrodes were connected to the LCR meter by alligator clips, as displayed in Figure 2.2a. The impedance was measured from 42 Hz to 2 kHz. The result shows that the GET–skin interface impedance is comparable with the gel electrode–skin impedance, although the GSHS surface area ( $\sim 0.245 \text{ cm}^2$ ) is more than 10 times smaller than that of the gel electrode ( $\sim 2.6 \text{ cm}^2$ ).

Low contact impedance is essential for a high SNR in electrophysiological measurements [211]. EEG, ECG, and EMG signals were measured using the GET (Figures 2.2b–d). The EEG signal was measured by laminating the GET on the forehead next to a commercial gel electrode, as shown in Figure 2.2b. Reference and ground electrodes were placed on the mastoid bone behind the right ear and on the forearm, respectively. No skin preparation was performed before mounting all the electrodes on the skin. The signal was amplified and recorded using a BrainVision recorder. During EEG measurement, the subject was asked to keep his eyes open for 1 min and then close his eyes for another minute. An alpha rhythm of frequency between 8 and 13 Hz is expected to appear in the EEG when the subject closes his eyes and relaxes. Fast Fourier transforms (FFT) were performed in MATLAB on EEG signals measured by the GET during eye opening and eye closure. The alpha rhythm with a peak at 10 Hz is clearly visible in the eye-closed EEG. It is evident in Figure 2.2b that the spectrograms of EEGs measured by the GET and gel electrodes are almost identical, and the blinks and alpha rhythms are clearly visible in both measurements.

The GET can also be laminated on the human chest to measure an ECG. Figure 2.2c shows the measurement setup and the ECG signal recorded by an AvatarEEG through both a GEPS and commercial gel electrodes, with a 60 Hz digital notch filter applied.

Characteristic ECG peaks (P, Q, R, S, T, and U) were clearly visible in both sets of data, but the GEPS measurement showed slightly higher signal magnitude. The SNR of the ECG measured by the GEPS was found to be 15.22 dB, which is higher than the SNR of the gel electrodes (11 dB). This can be attributed to the higher surface charge density and surface electric displacement field of graphene compared with Ag/AgCl gel, which results in the more efficient capturing of electrical potential [212].

Application of a GET for EMG measurement was demonstrated by laminating a GET on the human forearm. The electrical activity of the forearm flexor muscle was measured using both the GEPS and commercial gel electrodes when the subject was squeezing a handgrip (Figure 2.2d). An AvatarEEG was used to record the signal, and a 60 Hz digital notch filter was applied to both sets of recorded EMGs. The difference between the signals measured by the GET and gel electrodes in Figure 2.2d is attributed to the offset of electrode placement.

#### **2.4 IMPACT BY MOTION ARTIFACTS**

Another disadvantage of conventional dry electrodes lies in their high susceptibility to motion. However, because of the ultimate skin conformability of the GET, it is expected that the dry GET will have motion artifacts comparable with those of gel electrodes. To validate this hypothesis, commercial gel electrodes is placed next to a GEPS on the chest and artificial motions are induced in the skin by poking the chest with a glass rod at equal distances from both pairs of electrodes during ECG measurement, as shown in Figures 2.3a and b. The raw ECG signals recorded using the GET and gel electrodes, displayed in Figure 2.2c, indeed show comparable motion artifacts.

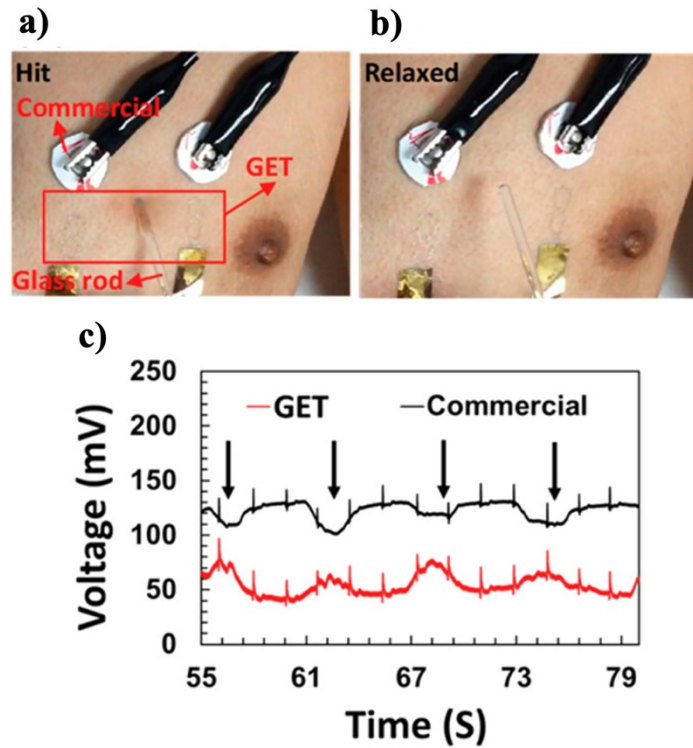


Figure 2.3: Comparison of motion artifacts in GET and gel electrodes [32]. (a, b) The motion was induced by poking the chest using a glass rod. (c) ECG synchronously recorded by a GET and gel electrodes shows comparable susceptibility to motion.

## 2.5 SUMMARY

The invention of a sub-micrometer-thick transparent GET is introduced in this Chapter. The GET can function as a stretchable and noninvasive electronic tattoo for multimodal biometric sensing. Although no adhesive is applied, the GET can fully conform to the microscale morphology of skin and follow arbitrary skin deformation without any fracture or delamination for an extended period of time. The GET was used to measure multiple biosignals including electrode-skin contact impedance, EEG, ECG, and EMG. As dry electrodes, the GET-skin interface impedance is almost as low as that of Ag/AgCl gel

electrodes, which can be attributed to its ultimate conformability. As a result, the GET has achieved comparable SNR with gel electrodes and demonstrated similar susceptibility to motion.

## Chapter 3: Stretchability of Linear GET and of Its Electrical Contacts<sup>5</sup>

In this Chapter, I report intrinsic electromechanical properties of linear graphene electronic tattoo (GET) through *in situ* microstructure and Raman investigations. This Chapter offers fundamental insight into the failure mechanism of linear GET and its electrical contacts, which is crucial for designing future graphene-based ultrathin wearables.

### 3.1 OBJECTIVE AND OVERVIEW

Emerging flexible and stretchable electronics technologies are expected to disrupt many conventional devices such as displays [213], robotics [28,214], wearables [3,22], implantable [2], and energy generators [215], attributing to their thinness, softness, ruggedness and lightweight. Particularly important in this field is to develop materials and structures that can maintain electronic functionality under large, cyclic deformations. Besides structurally designing conventional semiconducting and metallic materials into stretchable shapes [216], intrinsically deformable functional nanomaterials emerge as popular alternatives [2,217]. Nanomaterials used in soft electronics include carbon nanotubes (CNTs) [218,219], metal nanowires (NWs) [220,221], two-dimensional (2D) materials [222,223], and many more. Among them, graphene is the thinnest material (0.34 nm) that is also highly conductive both electrically and thermally, optically transparent, mechanically robust, biocompatible, and potentially low cost [144,224,225]. As a result, graphene has been widely applied as the electrode material in soft electronics, optics, sensors, and energy devices [226,227] as well as the thermal dissipator for power devices [228,229].

---

<sup>5</sup>H. Jang, Z. Dai, K-H. Ha, S.K. Ameri, and N. Lu, Stretchability of PMMA-Supported CVD Graphene and of Its Electrical Contacts, 2D Materials, 7, 014003, 2020.

While each of these applications exploits a different fundamental property of graphene, they all depend on its mechanical integrity for structural reliability and device performances. The mechanical behaviors of suspended graphene have been well studied [224,230,231]. Through nanoindentation, the pioneering work by Lee *et al.* found the pristine monocrystalline graphene to be the strongest material ever measured [224]. Specifically, the Young's modulus of pristine graphene is found to be  $\sim 1$ TPa, with a strength that can approach 130 GPa, and a surprising fracture strain up to 25% [224]. Defective graphene is more commonly used for electronics since graphene made with scalable fabrication techniques inevitably contains defects such as grain boundary, vacancies, and so on [232]. Interestingly, defects such as vacancies and oxygen-containing groups can even make graphene more damage-tolerant at least in the nanoindentation tests [233,234].

Herein, a monolayer CVD graphene was fabricated on 300-nm-thick PMMA substrate, which has been successfully applied as GETs [4,169]. Due to the ultrathin nature of the specimen, the Gr/PMMA ribbon was placed on a soft 3M Tegaderm tape for easier handling. I clamped and stretched four straight Gr/PMMA ribbons uniaxially with *in situ* electrical resistance measurement. Using  $R/R_0 = 20$  as the criterion to extract stretchability, the Gr/PMMA stretchability was measured to be  $14.5\% \pm 1.1\%$ , 45% higher than previously reported stretchability of Gr/PET specimens [235]. For microstructure characterization, *in situ* Raman spectroscopy and a high-power optical microscope were used. Four different stages of deformation and fracture can be clearly identified by combining the electrical resistance measurements and microstructure analysis. To investigate the stretchability of electrical contacts with graphene, gold/polyethylene terephthalate (Au/PET) or Gr/PMMA was laminated over Gr/PMMA and conducted electromechanical measurements and microstructure examination similar to the Gr/PMMA

ribbons. Very distinct behaviors were found for those two different types of electrical contacts. Cyclic tests were carried out on Gr/PMMA under small and large strain levels and the effects of PMMA thickness and Tegaderm adhesive were studied.

### 3.2 STRETCHABILITY OF CVD GRAPHENE ON POLYMER SUBSTRATES – A SURVEY

In practice, graphene is most often supported by a deformable substrate in soft (i.e., flexible and stretchable) electronic devices [227,236]. Therefore, the stretchability of polymer-supported CVD graphene has also been studied. Table 1 summarizes available results in the literature [68,74,235,237–239]. In this table, I only focus on CVD graphene sheets although there exist other forms of CVD graphene, such as graphene foam [240], graphene nanowalls [130], graphene scrolls [241] and graphene woven fabrics [242]. Depending on the type of substrate, the number of graphene layers, the boundary condition, and the criterion to extract stretchability, the reported stretchability of graphene vary significantly, from 2% up to 68%. So far, the easiest method for stretchability measurement involves *in situ* electrical resistance measurement on graphene while stretching the substrate. Stretchability can be identified as the strain when the resistance of deformed graphene normalized by the undeformed graphene ( $R/R_0$ ) reaches 10 or 20. In this study,  $R/R_0 = 20$  was chosen as the stretchability criterion in this study because that was the point where the resistance of GET reaches  $\sim 1$  Mohm where we considered it as non-conductive for wearable electrodes. The biggest discrepancy comes from the different strain quantification methods for graphene. It is well known that generally, graphene has weak interaction with the underlying substrate and hence can easily slide against the substrate when the substrate is deformed [243,244]. As a result, the strain transfer from substrate to graphene can be very limited and vary significantly from case to case [245,246]. The interface sliding may lead to higher apparent stretchability for unclamped graphene when

substrate strain is used to report stretchability [68,74,237]. By contrast, when graphene is clamped end-to-end [72,235] or local strain in graphene is measured using digital image correlation (DIC) method [239], the reported stretchability of graphene is limited to 10%. So far, only polymer substrates with hundred-micron thickness have been used. However, with the emergence of epidermal electronics such as the graphene electronic tattoos (GETs), graphene can be supported by much thinner substrates such as submicron-thick poly(methyl methacrylate) (PMMA) to achieve ultimate conformability and imperceptibility on human skin. The stretchability and failure mechanism of such graphene-on-ultrathin-PMMA are still unclear. Moreover, graphene has to make electrical contacts with other conductors in practice, but the stretchability of such contacts has never been investigated.

Reference	Substrate	# of layers of CVD graphene	Strain quantification method	Criteria of stretchability	Stretchability
Kim <i>et al.</i> , 2009	PDMS	1	Graphene NOT clamped end-to-end	Failure (No $R\sim\epsilon$ curve)	6%
Verma <i>et al.</i> , 2010	50 $\mu\text{m}$ PET	1	Graphene NOT clamped end-to-end	$R/R_0 = 10$	$\sim 42\%$
Lee <i>et al.</i> , 2011	PDMS	3	Graphene clamped end-to-end	Comparable mobilities of electrons and holes (No $R\sim\epsilon$ curve)	5%
Won <i>et al.</i> , 2014	188 $\mu\text{m}$ PET	1	Graphene strain measured by DIC	$(R-R_0)/R_0 = 10$ $R/R_0 = 20$	4.5% 10%
Lee <i>et al.</i> , 2017	188 $\mu\text{m}$ PET	1	Graphene clamped end-to-end	$R/R_0 = 20$	10%
Liu <i>et al.</i> , 2017	0.1 mm SEBS	1 2 3	Specimen mounting and strain definition unclear	$R/R_0 = 20$	$\sim 30\%$ $\sim 58\%$ $\sim 68\%$
Chun <i>et al.</i> , 2017	120 $\mu\text{m}$ PDMS	1	Graphene NOT clamped end-to-end	$\Delta R/R_0 \sim 8.5$	20%
Current work	300 nm PMMA on 47 $\mu\text{m}$ Tegaderm	1	Graphene clamped end-to-end	$R/R_0 = 20$	14.5% $\pm$ 1.1%

Table 3.1: A survey of the stretchability of CVD graphene on different polymer substrates under different strain quantification methods [247].

### 3.3 STRETCHABILITY AND ELECTROMECHANICAL BEHAVIORS OF GET

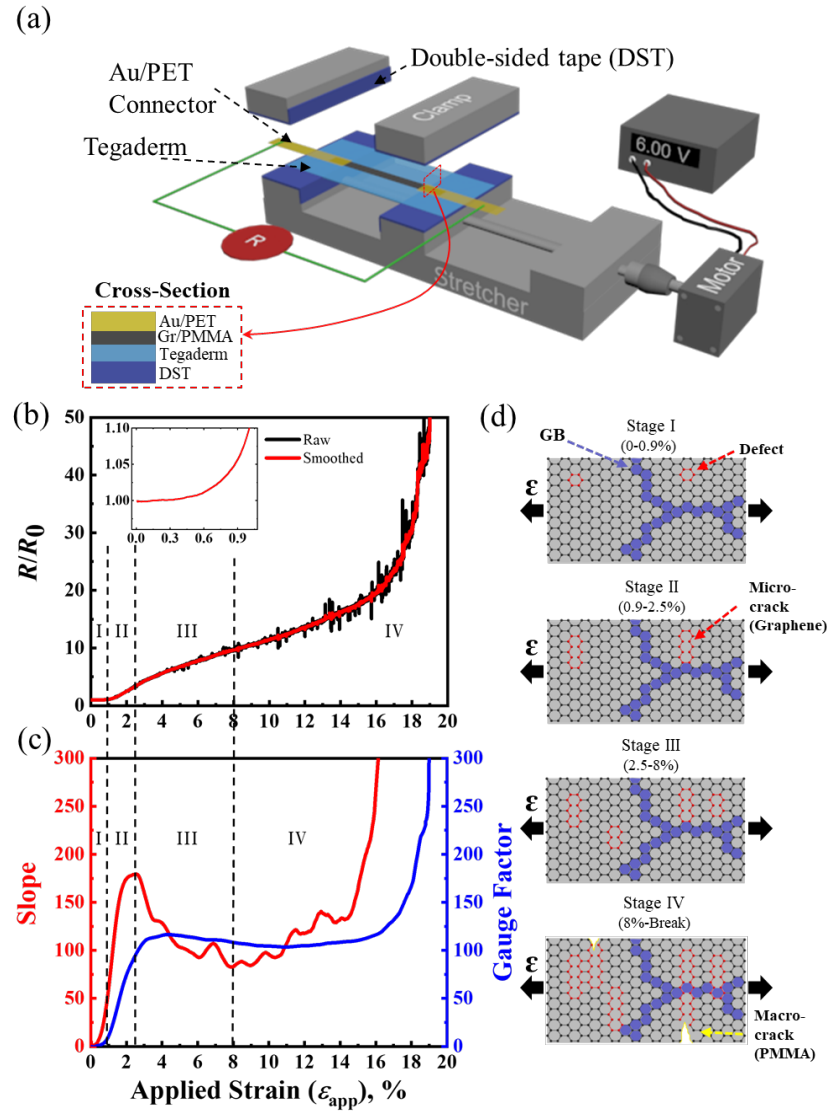


Figure 3.1: Uniaxial tensile test with *in situ* electrical resistance measurement [247]. (a) A schematic of the experimental setup where graphene was covered by Au/PET for electrical contact and fully clamped at the two ends. (b) Representative raw and smoothed curves of measured normalized electrical resistance of graphene ( $R/R_0$ ) as a function of the applied strain ( $\epsilon_{app}$ ). (c) Slope of the curve in (b) ( $d(R/R_0)/d\epsilon_{app}$ ) (red) and the gauge factor ( $GF = (\Delta R/R)/\epsilon_{app}$ ) (blue) as functions of the applied strain. (d) Illustrations of the four-stage deformation and fracture of Gr/PMMA.

To investigate the stretchability and electromechanical behaviors of Gr/PMMA ribbons, a homemade stretcher was used with a gear motor (TS-32GZ370-5300, Tsiny) to apply uniaxial tension and a data acquisition (DAQ) system (NI Elvis II) to measure electrical resistance *in situ* (Figure 3.1a). The Gr/PMMA ribbon supported by a 3M Tegaderm tape was clamped end-to-end to ensure that the applied strain was completely imposed on the ribbon specimen. The metal-based clamps of the stretcher were covered by double-sided tape (DST) for electrical insulation and mechanical buffer between the rigid clamps and the Gr/PMMA ribbon. The adhesive on the DST prevented the slippage of the specimen during tension. Two flexible Au/PET (100-nm-thick Au on 12.7- $\mu\text{m}$ -thick PET) ribbons were clamped together with Gr/PMMA at each end with Au touching graphene and alligator clips directly clipped on the extended parts of the Au/PET ribbons. The gauge length was 25 mm and the Gr/PMMA and Tegaderm width was 2 mm and 25 mm, respectively. The specimen was stretched uniaxially under a strain rate of  $5.2 \times 10^{-4} \text{ s}^{-1}$ . According to a two-dimensional (2D) finite element analysis (FEA) of an assumed intact specimen (with Tegaderm) subjected to applied strains up to 20%, the majority of the Gr/PMMA ribbon undergoes uniform uniaxial strain as large as the applied strain (Figure A1). It implies that such an experimental setup allows almost all applied strains to be imposed on the ribbon specimen if the specimen were not cracking.

The electromechanical results of the uniaxial tensile tests are presented in Figure 3.1b, which plots the electrical resistance of the graphene ribbon normalized by its initial resistance ( $R/R_0$ ) as a function of the applied strain until the ribbon fully fractures, i.e., when the resistance blows up. Raw data is plotted as the black curve. Fluctuations in the raw data could result from cracking in graphene. The raw data represented by the black curve was smoothed out to be the red curve using an adjacent-averaging method. Experimentally measured  $R/R_0$  vs.  $\epsilon_{\text{app}}$  curves of three more specimens are offered in Figure

A2. They show similar characteristics with the curve in Figure 3.1b but have slightly different rupture strains. If stretchability was defined using the criterion  $R/R_0 = 20$ , the average stretchability of the four Gr/PMMA ribbons tested is 14.5% with a standard deviation of 1.1%. It is 45% higher than previously reported Gr/PET specimens under the same criterion [42,43] and the explanation will be offered after examining the microstructures of the deformed specimens. In Figure 3.1c, the slope of the smoothed  $R/R_0$  vs.  $\varepsilon_{app}$  curve defined as  $d(R/R_0)/d\varepsilon_{app}$  is plotted as the red curve and the widely used gauge factor  $GF = (\Delta R/R_0)/\varepsilon_{app}$  is plotted as the blue curve although  $GF$  does not mean much for a nonlinear  $R/R_0$  vs.  $\varepsilon_{app}$  curve. Despite the continuous growth of graphene resistance, the slope of the resistance curve is nonmonotonic. Focusing on the red curve in Figure 3.1c, the slope starts from 0 but grows rapidly until an applied strain of 2.5% where the slope starts to decrease. The slope exhibits a U-shape until an applied strain of 15% where rapid growth kicks in again. Combining the slope analysis and the microstructure analysis in the next section, I have characterized the Gr/PMMA deformation and fracture process into four distinct stages as illustrated in Figure 3.1d. Stage I (0% ~ 0.9%) is the pre-cracking elastic deformation stage and grain boundaries (blue) and defects (red) in graphene are illustrated. Stage II (0.9% ~ 2.5%) is the stage when limited number of micro-cracks appear and grow to a limited length (~ 3  $\mu\text{m}$ ) in graphene and then halted, which is therefore named the “stage of limited micro-cracking in graphene.” Stage III (2.5% ~ 8%) is the stage when many new micro-cracks initiate and grow in graphene, which is therefore called the “stage of extensive cracking in graphene.” Stage IV (> 8%) is the stage of macro-cracking of PMMA and hence graphene until a complete electrical failure. In Stage IV, the raw resistance curve (black curve in Figure 3.1b) exhibits increasing fluctuation possible due to the macro-cracking of PMMA and hence graphene. The argument for Stages II and III comes from a previous stretchability study of monolayer CVD graphene on PET [235].

Through a careful study of how crack length and crack number evolve with strain, it concluded that micro-cracks in graphene start to form at  $\sim 1\%$  and they grow to a critical size ( $\sim 3 \mu\text{m}$ ) at  $\sim 2.5\%$ ; beyond  $2.5\%$ , existing cracks stop growing but new cracks start to initiate and grow; beyond  $8\%$ , many cracks grow beyond  $3 \mu\text{m}$ . In the next section, I will present our own semi-*in situ* Raman and optical micrographs to further justify our proposed four-stage deformation and failure of Gr/PMMA, especially at large strains.

### 3.4 MICROSTRUCTURE ANALYSIS OF GET UNDER DEFORMATION

#### 3.4.1 Raman Mapping under Uniaxial Tension

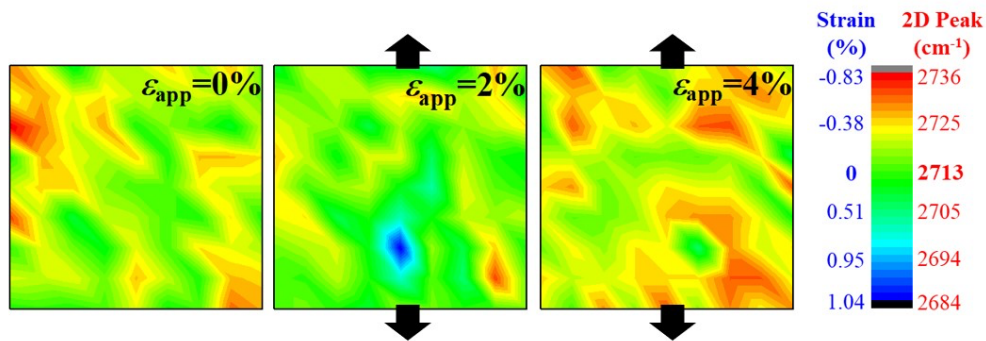


Figure 3.2: Raman mapping over  $20 \mu\text{m} \times 20 \mu\text{m}$  graphene at 0%, 2% and 4% of applied strains [247]. Black arrows indicate the direction of stretching. Blueshift and redshift indicate tension and compression, respectively.

To understand the measured change of resistance during the stretch, first *in situ* microstructure analysis was carried out by Raman mapping. The measurements were performed by placing the specimen on a customized low-profile stretcher directly under Raman spectroscopy. Figure 3.2 offers the Raman mapping results within one grain of the graphene ( $20 \mu\text{m} \times 20 \mu\text{m}$ ) at applied strains 0%, 2% and 4%. The 2D peak position of undeformed graphene was found to be  $2713 \text{ cm}^{-1}$  from Figure A3, and it was used as the

2D peak position at 0% of the applied strain. The 2D peak shift was converted to uniaxial strain using their linear relationship [248] and both are labeled in the color code of Figure 3.2. According to the Raman mapping, redshifts of 2D peak were present on the graphene from the beginning, which corresponds to an average compressive strain of 0.24%. This residual compressive strain could be attributed to the transfer or specimen mounting processes. Under 2% of applied strain, the average strain in graphene became 0.083% in compression and some region of graphene was stretched up to 1.04% of strain in tension, implying that overall the graphene layer was stretched but the applied strain was not fully experienced by the graphene. As graphene was clamped end-to-end, the small strain in graphene can be attributed to three possible mechanisms: 1) flattening of ripples, 2) the micro-cracking in graphene, and 3) graphene sliding against PMMA. As the applied strain further increased, however, average strain in graphene dropped to 0.32% in compression possibly due to more significant sliding.

#### **3.4.2 High-Power Optical Microscopic Analysis**

For optical microscopic analysis, it is first confirmed that graphene near the edges of the grippers did not crack before the central region and thereafter the central region of the specimen was always focused for the observation. At large strains, two distinct types of cracks, the micro-cracks of graphene and the macro-cracks of PMMA, are identified employing the contrast difference in the optical micrographs under high magnifications (Figure 3.3, Figures A4-A7). Among many micrographs with repetitive behaviors, Figure 3.3 showcases the representative micrographs of the Gr/PMMA ribbon under different

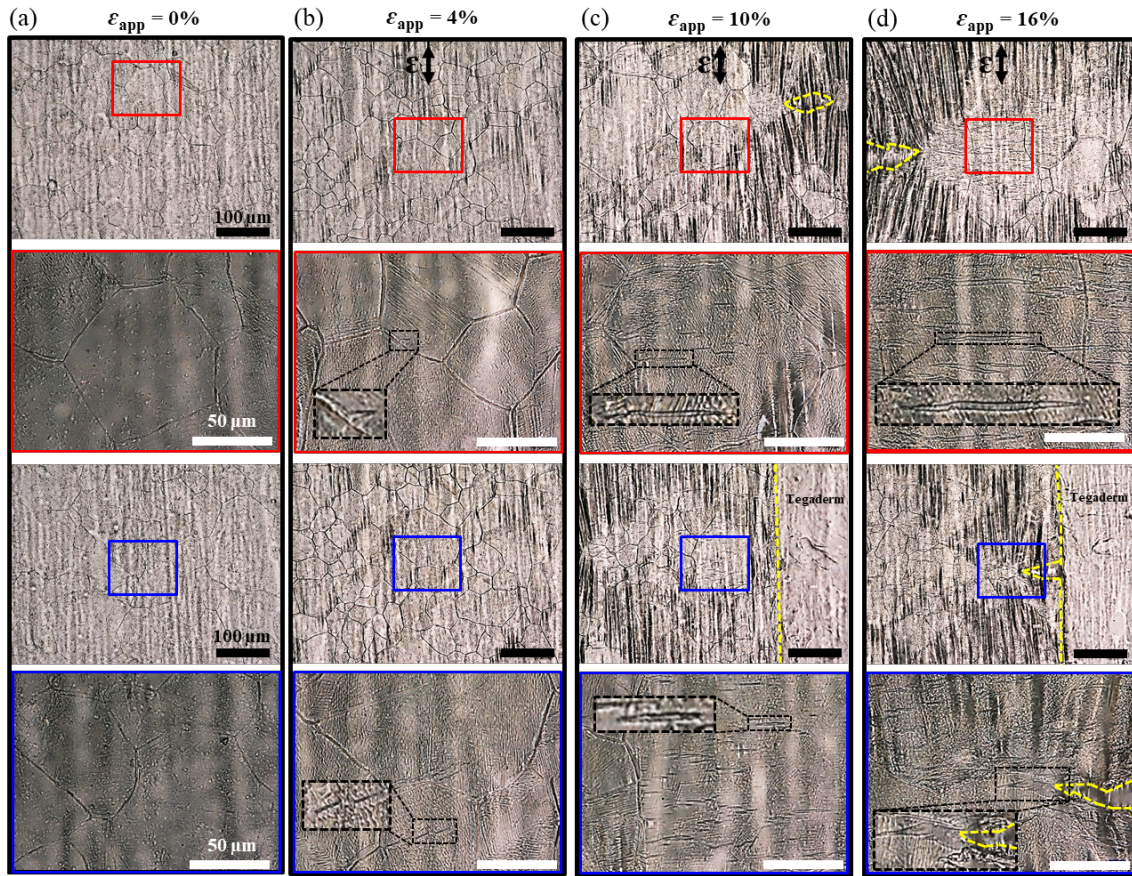


Figure 3.3: High-power optical micrographs of the Gr/PMMA under 500x (first and third rows) and 2000x (second and fourth rows) magnifications at (a) 0%, (b) 4%, (c) 10% and (d) 16% of applied strains ( $\epsilon_{app}$ ) [247]. Tensile strain was applied along the vertical direction of the micrographs. Yellow dashed lines highlight the edges of PMMA. Black boxes offer blown-up views of graphene cracks.

strain levels. Two sets of micrographs of unstretched graphene (0%) are exhibited in Figure 3.3a. The small boxes indicate the regions to be magnified and the corresponding blown-up views are located right below. Although full of ripples inherited from the grain boundaries of the growth Cu foil, no cracks can be observed in graphene at 0%. When the Gr/PMMA ribbon was stretched vertically by 4%, micro-cracks of graphene in the size of

tens of microns became visible in the black dashed boxes within the magnified views (Figure 3.3b). At higher applied strains (10% and 16%), macro-cracks of 300-nm-thick PMMA in the size of sub-millimeters were observable and the yellow dashed lines highlight the macro-crack and edge of PMMA (Figure 3.3c). At a given applied strain, the micro-cracks of the graphene are bigger and denser near the crack tips of PMMA. They further grew with increasing applied strain (Figures 3.3c and 3.3d). As electrical current can still flow through the Gr/PMMA ribbon as long as a conductive path can be found, electrical resistance was still measurable even with those micro- and macro-cracks. Finally, the macro-cracks interconnected with each other, forming a complete transverse rupture of the whole ribbon, which completely cut off the current flow and killed the electrical resistance.

Combining the microstructure analysis with the electromechanical measurement results in Chapter 3.3, the deformation and fracture of the Gr/PMMA ribbon is classified and justified into four distinct stages as illustrated by the schematics in Figure 3.1d. Stage I is before the applied strain reaches 0.9%, up to which point there is no significant change in resistance. It is hypothesized that the compressive residual strain in the unstretched graphene during the wet-etch and transfer process releases in this stage [249] and initial ripples in the specimen get flattened, and therefore the resistance change is insignificant. Although the grain boundaries (GBs) of the graphene are represented by blue hexagons for Stage I schematic in Figure 3.1d, in reality, the GBs should be misoriented and overlapped. Moreover, structural defects such as the non-homogenous size of the carbon hexagons and irregular geometrical shapes (polygons) are not reflected in this schematic. Getting into Stage II, the resistance elevates rapidly up to 2.5% of applied strain possibly due to the formation of similar-sized micro-cracks in graphene as illustrated by the red-highlighted zones in Stage II schematic of Figure 3.1d according to [235]. From 2.5% to 8%, in Stage

III, the slope of  $R/R_0$  vs.  $\epsilon_{app}$  curve decreases as a result of substantial strain relaxation due to sliding, despite the initiation and growth of new micro-cracks as illustrated in Stage III schematic of Figure 3.1d. Beyond 8% is Stage IV, where the slope of  $R/R_0$  vs.  $\epsilon_{app}$  curve starts to increase due to the macro-cracking of PMMA and hence graphene as illustrated by Figure 3.1d Stage IV schematic. This statement is supported by micrographs in Figures 3.3c,d and A4-A7. The resistance increases abruptly beyond 14.5% and the ribbon breaks completely around 19% of the applied strain. Based on a consistent fracture criterion, i.e.,  $R/R_0 = 20$ , the stretchability of our Gr/PMMA ribbon is  $14.5\% \pm 1.1\%$ , 45% higher than that of PET-supported graphene [235]. The enhancement in stretchability can be attributed to the macro-cracks in PMMA. In fact, strategically designed cuts have been intentionally fabricated in kirigami nanocomposites and auxetic metamaterials to enhance their stretchability. This is because the tensile displacement can be accommodated by the opening of the pre-engineered cuts, which helps release strain in the intact region of the specimen. Based on the repeatability test over four different specimens (Figure A2), the strain levels defining the stages vary a bit from specimen to specimen. Such variation can be attributed to the different microscopic and macroscopic defects in graphene caused by the CVD growing process, the metal etching process, the wet transfer process, the push-cut process, the final pasting process and/or the specimen mounting process.

As micro-cracks in graphene initiate at 0.9%, the three  $R/R_0$  vs.  $\epsilon_{app}$  loading-unloading curves in Figure A8 are all irreversible. The extensive sliding between Gr and PMMA at large strains further enlarges the hysteresis in the loading-unloading curves.

### 3.5 STRETCHABILITY OF ELECTRICAL CONTACTS WITH GET

In practice, graphene-based devices such as the graphene e-tattoos (GETs) must connect with readout circuits through electrical contacts. Therefore, the stretchability of the electrical contacts with our Gr/PMMA ribbon is found in this study. Two Au specimens were prepared through thermal evaporation and stretched to find out their intrinsic stretchability before contacting with graphene. The first Au specimen was 100-nm-thick Au on 10-nm-thick Cr on 300-nm-thick PMMA (Au/Cr/PMMA) which is the same PMMA as in the Gr/PMMA specimen. The second Au specimen was 100-nm-thick Au on 13- $\mu$ m-thick PET (Au/PET). Both were prepared to have the same in-plane dimensions as the Gr/PMMA specimens and measured the same way as the Gr/PMMA specimens. Their  $R/R_0$  vs.  $\epsilon_{app}$  curves are plotted together with the Gr/PMMA one in Figure 3.4. It is evident that the Au/Cr/PMMA specimen fully ruptured at 1% whereas the Au/PET specimen failed at ~23%. This is consistent with the previous finding that the thicker and stiffer substrate better spreads the strain in the metal thin film hence affords much higher stretchability. As a result, the Au/PET ribbon was chosen to make electrical contact with Gr/PMMA because it is much more robust than the Au/Cr/PMMA and the Gr/PMMA specimen. Of course one can also use other stretchable electrical connectors based on PEDOT:PSS or polymer doped with AgNWs, CNTs, and metal nanoparticles [53,250].

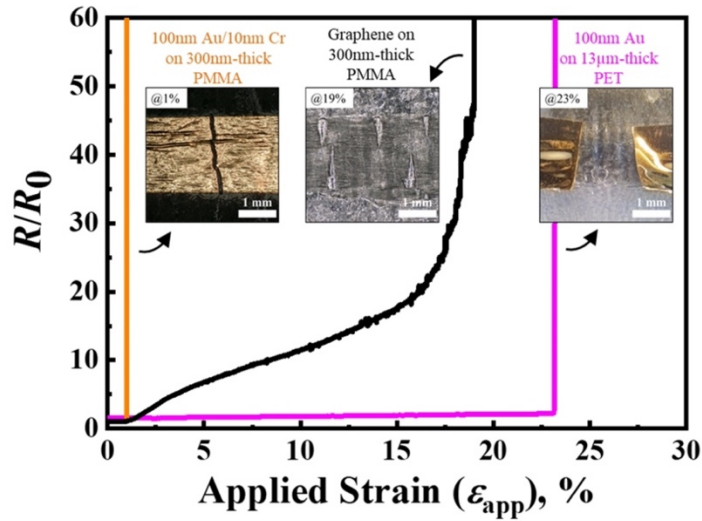


Figure 3.4: Normalized electrical resistance of Gr/PMMA (black), Au/Cr/PMMA (orange), and Au/PET (magenta) ribbons plotted together against the applied strain [247]. The three insets display the center region of the Au/Cr/PMMA, Gr/PMMA and Au/PET specimens at failure.

The stretchability of electrical contacts with Gr/PMMA is presented in Figure 3.5. The 3D inset in Figure 3.5a left panel illustrates the electrical contact between Gr/PMMA and Au/PET. An anisotropic conductive film (ACF, 3M 9703) was applied between graphene and Au for secure bonding. Uniaxial tension with *in situ* resistance measurement was carried out for this hybrid specimen and the  $R/R_0$  vs.  $\epsilon_{app}$  curve is plotted in Figure 3.5a left panel. The micrograph of the interface at the fracture point (2.6%) is provided in the right panel of Figure 3.5a. It is evident that the Gr/PMMA ribbon ruptured along the edge of the Au/PET ribbon due to the significant mismatch in mechanical stiffness – 1.24 N/mm for Gr/PMMA and 46.9 N/mm for Au/PET. To minimize the stiffness mismatch, I chose to apply a Gr/PMMA to bridge two disconnected Gr/PMMA ribbons as illustrated by the inset in Figure 3.5b left panel. The Gr/PMMA ribbon was thin enough to make electrical

contact with another Gr/PMMA ribbon via just van der Waals forces, so no ACF was applied in this case. I will refer this specimen as the bridged Gr/PMMA specimen in the follows. Figure 3.5b plots the raw and smoothed  $R/R_0$  vs.  $\epsilon_{app}$  curves for this specimen together with that of a continuous Gr/PMMA specimen for comparison. Despite the large fluctuation in resistance, the bridged Gr/PMMA specimen exhibits slightly higher stretchability than the continuous Gr/PMMA specimen. Both the fluctuation in resistance and the larger stretchability can be attributed to the sliding between lower and upper graphene. Graphene-graphene sliding is easy to occur and has been widely observed and investigated [251,252]. Both micro- and macro-cracks were visible in the lower Gr/PMMA ribbons and more cracks were concentrated near the edge of the interface as evident in the micrographs offered in the right panel of Figure 3.5b. Once the resistance started to change under applied strains, it was not reversible due to the crack formations (Figure A9). However, compared to the loading and unloading curves of the continuous Gr/PMMA specimen (Figure A8), the loading curves of the bridged Gr/PMMA specimen exhibits larger flat regions, which should result from the sliding between the graphene layers. The improved stretchability for Gr/PMMA to Gr/PMMA contact over Gr/PMMA to Au/PET contact demonstrates that minimizing mechanical stiffness mismatch is the key to enhancing the stretchability of such contacts.

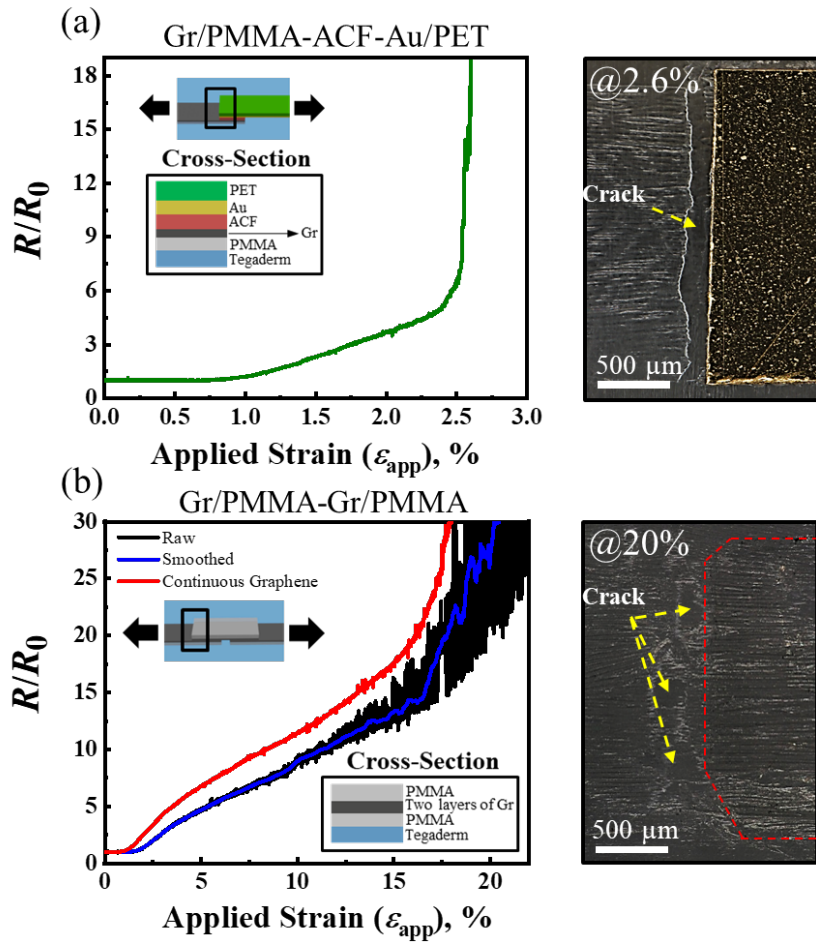


Figure 3.5: The stretchability of electrical contacts with Gr/PMMA [247]. (a) Au/PET and (b) Gr/PMMA overlayer laminated on Gr/PMMA with Au or graphene facing graphene to make electrical contacts. Au/PET was attached to Gr/PMMA through ACF adhesive but nothing was applied between two Gr/PMMA. The left panels plot the normalized end-to-end electrical resistance vs. applied strain. Right panels are micrographs at the edge of the contact taken at the fracture point. Red dashed line in the micrograph of (b) highlights the edge of the top Gr/PMMA.

### 3.6 DISCUSSION

This section provides some additional information regarding the stretchability of Gr/PMMA: the cyclic behavior, the effects of PMMA thickness, and the effect of adhesives at the interface between Gr/PMMA and the substrate.

#### 3.6.1 Cyclic Behaviors of GET

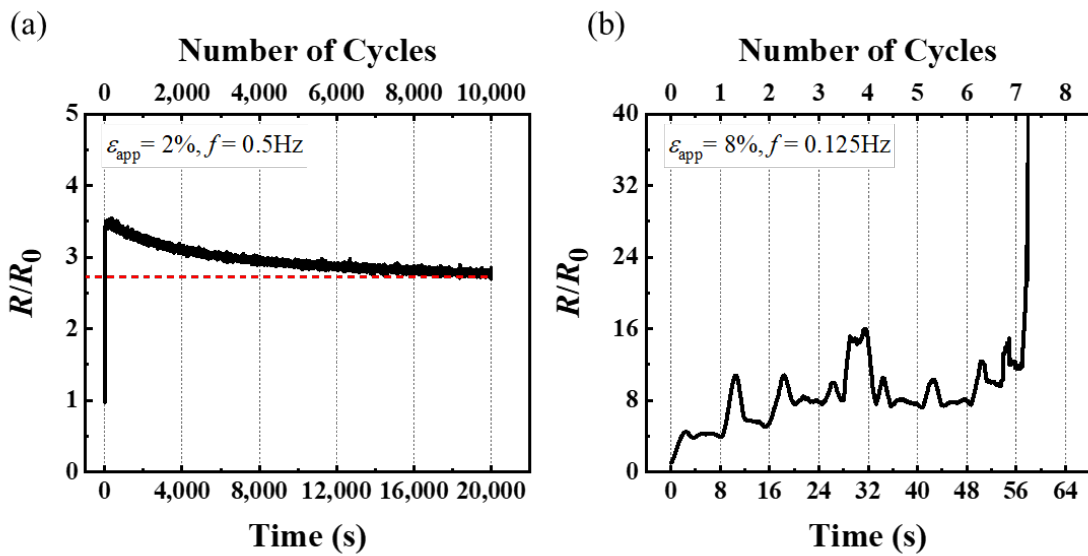


Figure 3.6: Normalized resistance of the Gr/PMMA ribbon under applied cyclic strain of (a) 0-2% at 0.5 Hz and (b) 0-8% at 0.125 Hz [247].

Although the fatigue behavior of graphene composites has been well studied [253,254], the fatigue behavior of graphene on polymer has been rarely discussed. I, therefore, carried out cyclic electromechanical tests on Gr/PMMA ribbons from 0% up to two different strain levels – 2% and 8%. The two strain levels represent two different stages in the deformation and failure process – 2% is in State II when a limited number of micro-cracks appear in graphene, but they tend not to grow beyond  $3\ \mu\text{m}$  [235]; 8% is the

beginning of Stage IV when macro-cracks in PMMA emerge. The same strain rate of  $1 \times 10^{-2} \text{ s}^{-1}$  was applied in both tests. Figure 3.6 plots the normalized resistance as a function of cyclic time (bottom axis) and number of cycles (top axis). For 2% of applied strain, the resistance of graphene exhibited a sharp rise upon first stretch followed by a gradual decay with growing number of cycles up to 10,000 cycles. The reason for such decay in resistance remains elusive for us at this moment. It is speculated that it may have something to do with graphene sliding and buckling during the repetitive loading and unloading process. In contrast, the resistance of graphene continued to grow in the cyclic test up to 8% of applied strain and reached complete failure only after the 8<sup>th</sup> cycle (Figure 3.6b). Multiple macro-cracks in PMMA were observable at the failure point. This is consistent with the known fatigue behavior of PMMA [255].

### 3.6.2 Effect of Polymer Thickness

As a thermoplastic polymer, both ductile and brittle fracture modes exist in PMMA. When the thickness of PMMA is increased, brittle fracture mode is favored. To illustrate the effect of PMMA thickness, the stretchability of monolayer graphene and 100-nm-thick Au supported by a thicker PMMA (1- $\mu\text{m}$ -thick) were also measured, and the results are presented in Figure 3.7. In Figure 3.7a, it is obvious that compared with the stretchability of graphene on 300-nm-thick PMMA (14.5%), the stretchability of graphene on 1- $\mu\text{m}$ -thick PMMA is only 10% and the ribbon was failed by only one straight and brittle crack (inset of Figure 3.7a). However, the effect of PMMA thickness on 100-nm-thick Au ribbon is quite the opposite as shown by Figure 3.7b – the specimen with 300-nm-thick PMMA ruptured at 1% whereas that with 1- $\mu\text{m}$ -thick PMMA ruptured at 1.4%. This is because both strains are way below the brittle fracture strain of the PMMA. Therefore, according

to fracture mechanics of thin films, the thicker PMMA provided more substrate constraint on Au nanomembrane and hence helped enhance its stretchability.

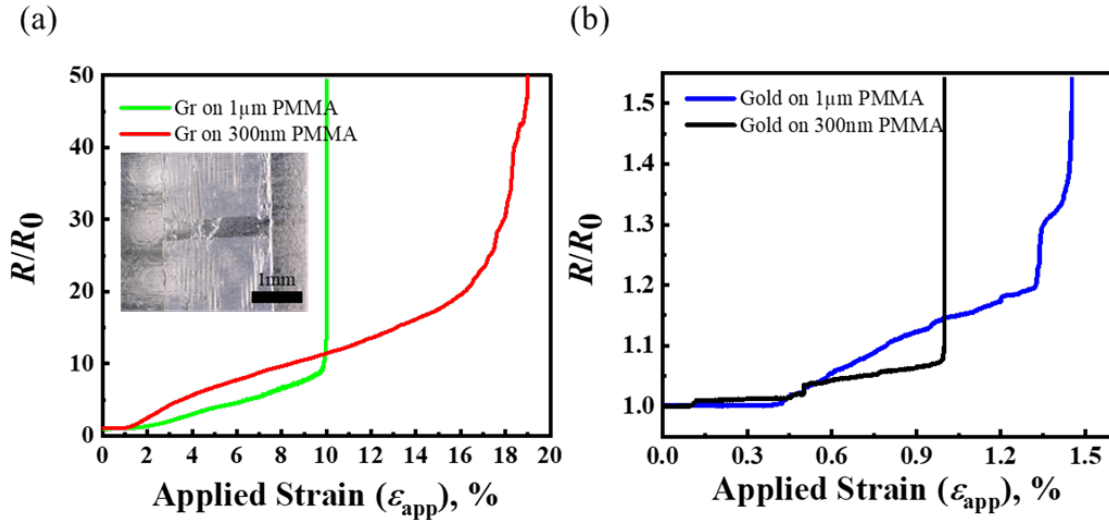


Figure 3.7: PMMA thickness effect on the stretchability of (a) the Gr/PMMA ribbons and (b) Au/PMMA ribbons [247]. The inset in (a) shows the brittle fracture of graphene on 1- $\mu$ m-thick PMMA at the applied strain of 10%.

### 3.6.3 Effect of the Adhesion between GET and Substrate

Because the Gr/PMMA ribbon was placed on the native adhesive of the Tegaderm tape, there could be a concern of the adhesive effect. As a result, a contrast experiment was carried out in which case the Gr/PMMA ribbon was transferred to the non-sticky side of Tegaderm. Figure 3.8a plots the  $R/R_0$  vs.  $\epsilon_{app}$  curves of both cases in one chart, which indicates that the stretchability is independent of the adhesive. This finding can be understood as follows. Although the adhesive force is low on the non-sticky side of Tegaderm, the Gr/PMMA ribbon was still able to well conform to the Tegaderm via van der Waals forces due to its thinness (300 nm). Therefore, there was negligible sliding under

deformation until macro-cracks appeared in PMMA, where delamination between the ribbon and the Tegaderm substrate was clearly observable at the macro-cracks (Figure 3.8b). Because such cracks were sparse, the sliding after such cracking could make very limited contribution to the stretchability.

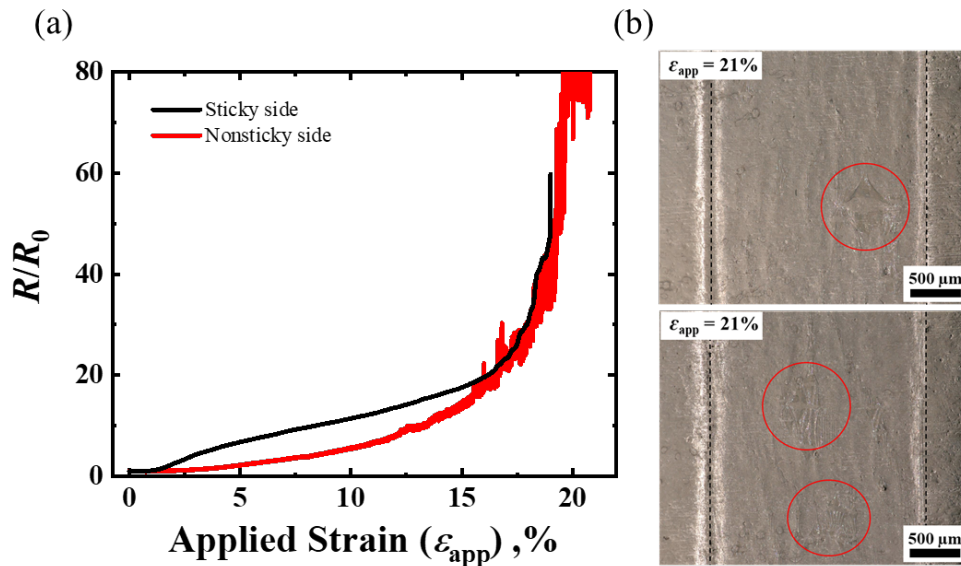


Figure 3.8: Effect of Tegaderm adhesive on Gr/PMMA stretchability [247]. (a) Comparison of the normalized resistance vs. applied strain for Gr/PMMA ribbons transferred on the sticky (black) and non-sticky (red) sides of the Tegaderm. (b) The micrographs at fracture on the non-sticky side. Black dashed lines indicate the edge of the Gr/PMMA ribbon. Red circles highlight the delamination of the Gr/PMMA around the macro-cracks.

### 3.7 SUMMARY

To conclude, 300-nm-thick Gr/PMMA ribbons suitable for the applications of stretchable and wearable electronics were fabricated and measured its stretchability to be  $14.5\% \pm 1.1\%$  according to the criterion of  $R/R_0 = 20$ . The ribbon did not fully rupture until

~19% of the applied strain. Four distinct deformation/fracture stages were successfully identified when combining the electromechanical measurement with the *in situ* microstructure analysis. Micro-cracks in graphene started to emerge at very low applied strains (~0.9%) and form similar-sized cracks until ~2.5% of the applied strain. After 2.5% of the applied strain, more micro-cracks initiated and propagated. Macro-cracks in PMMA developed after an applied strain of ~8%. Both sliding between graphene-PMMA and the macro-cracks in PMMA helped alleviate the tensile stress in graphene, resulting in smaller resistance rise and higher stretchability. But the resistance curves are irreversible due to such cracks. The stretchability of different electrical contacts with the Gr/PMMA specimen was also investigated and concluded that minimizing mechanical stiffness mismatch between the two contacting parts can effectively enhance the stretchability of these contacts. It was found that Gr/PMMA can be highly cyclable up to 2% but not 8%. Although PMMA thickness has a significant effect on Gr/PMMA stretchability, the Tegaderm adhesive does not. This study provides a comprehensive understanding of the stretchability and fracture behaviors of graphene supported by ultrathin polymer substrates and their electrical contacts. Therefore, it offers useful insights for designing future graphene-based soft electronic devices.

## **Chapter 4: Enhancing the Stretchability of GET Electrical Contacts Through Heterogenous Serpentine Ribbons (HSPR)<sup>6</sup>**

In this Chapter, a novel interface design, so-called heterogeneous serpentine ribbons (HSPR) that forms a mechanically reliable interconnection between GET and a rigid back-end circuit, is introduced. This concept is validated by numerical and experimental analysis. This method offers a solution for the long-standing interconnect challenges between ultrathin electrodes and rigid electronics.

### **4.1 OBJECTIVE AND OVERVIEW**

An outstanding challenge is to reliably interface the sub-micron-thin, stretchable GET with millimeter-thick, rigid printed circuit board (PCB) for data acquisition and wireless data transmission. Although GET is stretchable, the sub-micron thinness makes it rupture easily under even a tiny force [247]. Therefore, conventional electrical connections for thin-film sensors such as soldering or z-axis conductive tapes are not applicable to GET. Silver paste and liquid metal have been employed to form a softer electrical contact with graphene [66,68]. However, their liquid-like form factor defeats the concept of solid-state electronics and also adds to the thickness and visibility of the device. In fact, reliable and viable electrical contacts and packaging remain to be an outstanding challenge for other ultrathin flexible and stretchable devices [256–259]. An effective and easy-to-implement terminal connection has to be invented to overcome this longstanding barrier.

Here, we propose using heterogeneous serpentine ribbons (HSPR) to reliably connect serpentine GET on the palm to a rigid EDA watch worn on the wrist. HSPR represents a GET serpentine that partially overlaps with a sub-micron-thin gold-on-

---

<sup>6</sup>H. Jang, K. Sel, E. Kim, S. Kim, X. Yang, S. Kang, K-H. Ha, R. Wang, Y. Rao, R. Jafari, and N. Lu, Graphene E-Tattoos for Ambulatory Electrodermal Activity Sensing on the Palm Enabled by Heterogeneous Serpentine Ribbons, Nature Communications, Under Review, 2022.

polyimide (Au/PI) serpentine which is also laminated on the skin, with graphene facing down and Au facing up so that they make direct electrical contact through just van der Waals (vdW) forces. No adhesive is needed for the HSPR because the GET is too thin to delaminate from the Au even with just vdW adhesion. According to finite element modeling (FEM), the HSPR offers 50 folds of strain reduction at the interface compared to heterogeneous straight ribbons (HSTR), i.e., a straight GET ribbon partially laminated on a straight Au/PI ribbon. Moreover, when the HSPR is clamped end-to-end and stretched, no electrical failure can be detected until 42% of strain.

#### 4.2 FABRICATION PROCESS

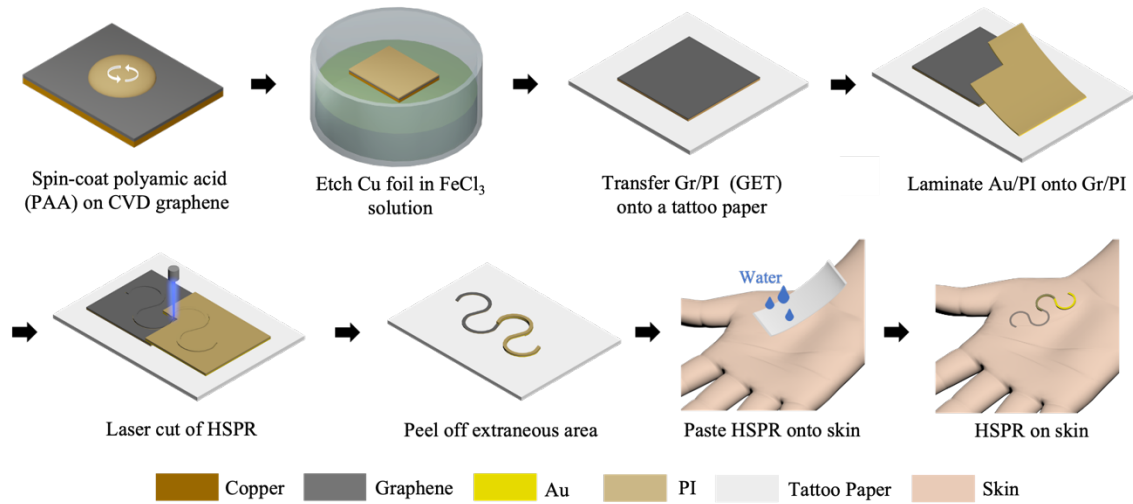


Figure 4.1: Laminate-cut-paste fabrication of HSPR (Arm). Polyimide (PI) precursor – polyamic acid (PAA) is spin-coated on a CVD graphene grown on a Cu foil. The Cu is etched in  $\text{FeCl}_3$  solution, and the PI-supported graphene (Gr/PI) is transferred onto a commercial tattoo paper with graphene facing up. 100-nm-thin Au deposited on 650-nm-thin PI is partially laminated over the GET. A UV laser carves the two sheets into HSPR (Arm) which indicates that the Au/PI terminates at the arm of the serpentine. The patterned HSPR (Arm) can be pasted onto human skin by wetting the tattoo paper.

Our group previously developed a “wet transfer, dry patterning” process to fabricate GET [260]. It involved a conventional wet transfer of large-area CVD graphene through PMMA coating and copper etching but utilized a “cut-and-paste” process [261] to pattern the graphene/PMMA bilayer by mechanical or laser cutting to avoid chemical contaminations on graphene associated with photolithography. To fabricate HSPR, I adopt the same wet transfer process except that we switch the backing layer from PMMA to PI given the better stretchability of PI. Because the serpentine ribbons are hard to align after patterning, it is decided to perform cutting on a heterogeneous sheet of Au/PI-GET where the Au/PI is strategically overlapped with GET, depending on where I want to locate the Au/PI step edge.

Figure 4.1 illustrates the overall “lamine-cut-paste” fabrication process of HSPR starting from forming a 300-nm-thin PI layer over a large-area CVD graphene grown on copper (Grolltex Inc.). The curve of PI on graphene thickness vs. spin-coating speed is reported in Figure A10. After curing the PI layer, the copper foil is etched in ferric chloride ( $\text{FeCl}_3$ ) solution and the graphene/PI bilayer (Gr/PI) is rinsed in DI water. The sheet resistance of monolayer Gr on PI is measured to be 1.2 kOhm/sq. To reduce the resistance, one more CVD graphene layer is added by simply laminating the Gr/PI on another CVD graphene on copper with graphene touching each other and then etching away the copper. The sheet resistance of Gr/PI is reduced 2.9 times to 410 Ohm/sq by forming bilayer graphene. The bilayer graphene supported by a PI is transferred onto a commercial temporary tattoo paper (temporary tattoo paper, Silhouette America Inc.) with graphene facing up.

Next, 750-nm-thin Au/PI bilayer (100-nm Au on 650-nm PI) with a cutaway is laminated on the same tattoo paper with Au facing the graphene and a partial coverage over the Gr/PI. To fabricate the 750-nm-thin Au/PI layer, Polyamic acid (PAA) solution is

diluted with N, N-Dimethylacetamide (DMA) with a 2:1 volume ratio. The diluted PAA solution is spin-coated at 1000 rpm for 45 s on a 25- $\mu\text{m}$ -thick Copper foil and pre-baked at 150°C for 5 min and baked at 250°C for 60 min. The copper foil is etched in ferric chloride ( $\text{FeCl}_3$ ) solution for 2 hours then transferred on a tattoo paper. To improve adhesion between Gold and a polyimide film, 5-nm-thin Chromium is deposited first on the polyimide film and then 100-nm-thin Gold is deposited.

Laser cutting of the HSPR needs to align with the Au/PI cutaway to locate the edge of the Au/PI at the arm of the Gr/PI serpentine. After the extraneous areas are removed, the HSPR on the tattoo paper can be flipped over to paste to a target substrate, such as elastomer or skin. The HSPR can be released effortlessly by wetting the backside of the tattoo paper, leaving a GET over Au/PI HSPR on the skin where the step edge is located at the arm of the GET serpentine. To locate the step edge at the crest of the GET serpentine, no cutaway in the Au/PI is needed and the edge of the Au/PI should align with the crest of the GET serpentine which is defined by the laser patterning.

### 4.3 MECHANICAL CHARACTERIZATIONS OF HSPR

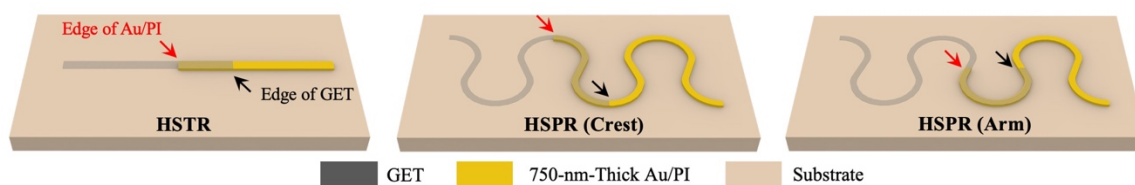


Figure 4.2: Three different heterogeneous configurations (HSTR, HSPR (Crest), HSPR (Arm)) are stretched experimentally and numerically. The red arrow and black arrow highlight the edge of Au/PI and the edge of GET, respectively.

Mechanical characterization and analysis of HSPR are detailed in this section. Two benchmarking cases including the straight GET ribbon (not drawn) and the HSTR (Figure 4.2 left panel) are considered as non-engineered uniform ribbon and non-engineered heterogeneous interface, respectively. Two different HSPR cases - HSPR (Crest) (Figure 4.2 middle panel) and HSPR (Arm) (Figure 4.2 right panel) are investigated. All ribbons are supported by 100- $\mu\text{m}$ -thick Ecoflex 00-30 substrate which mimics the human skin. I always use red arrows to indicate the step edges of Au/PI and black arrows to signify the edges of GET in the heterogeneous ribbons. In this work, a 300-nm-thin GET is interfaced with a 750-nm-thin Au/PI to form HSTR and HSPR. As an electrical connector for GET, the 750-nm-thin Au/PI is chosen because it can satisfy the following requirements. First, the electrical connector should be stretchable more than 45% [262] since it will be placed across the wrist where large skin deformation can occur. Second, according to our previous work [247], a smaller mechanical stiffness mismatch between GET and the interfacing electrical connector yields higher stretchability of the interface. The 750-nm-thin Au/PI is only 2.5 times thicker and 7.7 times stiffer (stiffness is computed as the summation of the multiplication of modulus and thickness of each layer) than GET while it can provide enough stretchability of  $65 \pm 4.9\%$  when it's patterned into a serpentine shape (Figure A11). In contrast, conventionally used 13- $\mu\text{m}$ -thick Au/PI sheets are 37.6 times stiffer than GET, which only achieved a stretchability of 2.6% when forming an HSTR with the GET [247]. It should be noted that electrical connectors other than Au/PI can also be used as long as the above requirements are met.

### 4.3.1 Serpentine Geometry Effect

Once the material properties of HSPR are fixed, another factor that can affect the stretchability of HSPR is the serpentine geometry. To unveil the governing factors, I carry out a parametric study for the configuration of HSPR (Arm) using FEM. For the FEM simulation of HSPR, the commercial software ABAQUS (standard 6.13) was employed. Dynamic implicit step with nonlinear geometry was implemented. The HSPR and the stretching substrate (100- $\mu\text{m}$ -thick Ecoflex) were modeled using a 3D deformable shell with S4R elements. Each layer was partitioned accordingly and assumed that there was no delamination at the interface. For GET, 300-nm-thin PI was assigned as an elastic material with a modulus of 2.5 GPa and Poisson's ratio of 0.34. For Au/PI, 100-nm-thin Au was assigned as an elastic material with a modulus of 79 GPa and Poisson's ratio of 0.42, and 650-nm-thin PI was assigned with the same PI property shown above. Ecoflex was modeled as an incompressible Neo-Hookean hyperelastic material with a modulus of 0.1 MPa. The HSPR was stretched end-to-end with 20% of applied strain and no out-of-plane deformation was allowed. As depicted in Figure 4.3a, our previous work has defined the unit cell of the serpentine geometry by four parameters: the ribbon width  $w$ , the arc radius  $r$ , the arc angle  $\alpha$ , and the arm length  $l$  [263,264]. After normalization, there are three dimensionless parameters  $w/r$ ,  $l/r$ , and  $\alpha$ . Some examples of serpentine shapes are displayed in Figure 4.3b-d. Our FEM results are presented in terms of the strain reduction (i.e., maximum strain in GET over applied strain ( $\epsilon_{max}/\epsilon_{app}$ )) depending on  $w/r$ ,  $l/r$ , and  $\alpha$ . I find that  $w/r$  has the largest impact on the strain reduction – almost three folds when  $w/r$  decreases from 0.8 to 0.2 (Figure 4.3e). Regarding the effects of  $l/r$  and  $\alpha$ , the largest strain reduction occurs when  $l/r$  is between 0 and 0.5, and  $\alpha$  between  $0^\circ$  and  $20^\circ$  (Figure 4.3f,g). In fact, the values of  $l/r$  and  $\alpha$  enabling the largest strain reduction also depend on the level of extension. As skin deformation is generally considered to be around 20%

[265,266], a HSPR shape is chosen with  $w/r = 0.2$ ,  $l/r = 0.5$  and  $\alpha = 20^\circ$  for the following experimental investigation. The ribbon width is fixed to  $w = 1$  mm for easy laser patterning.

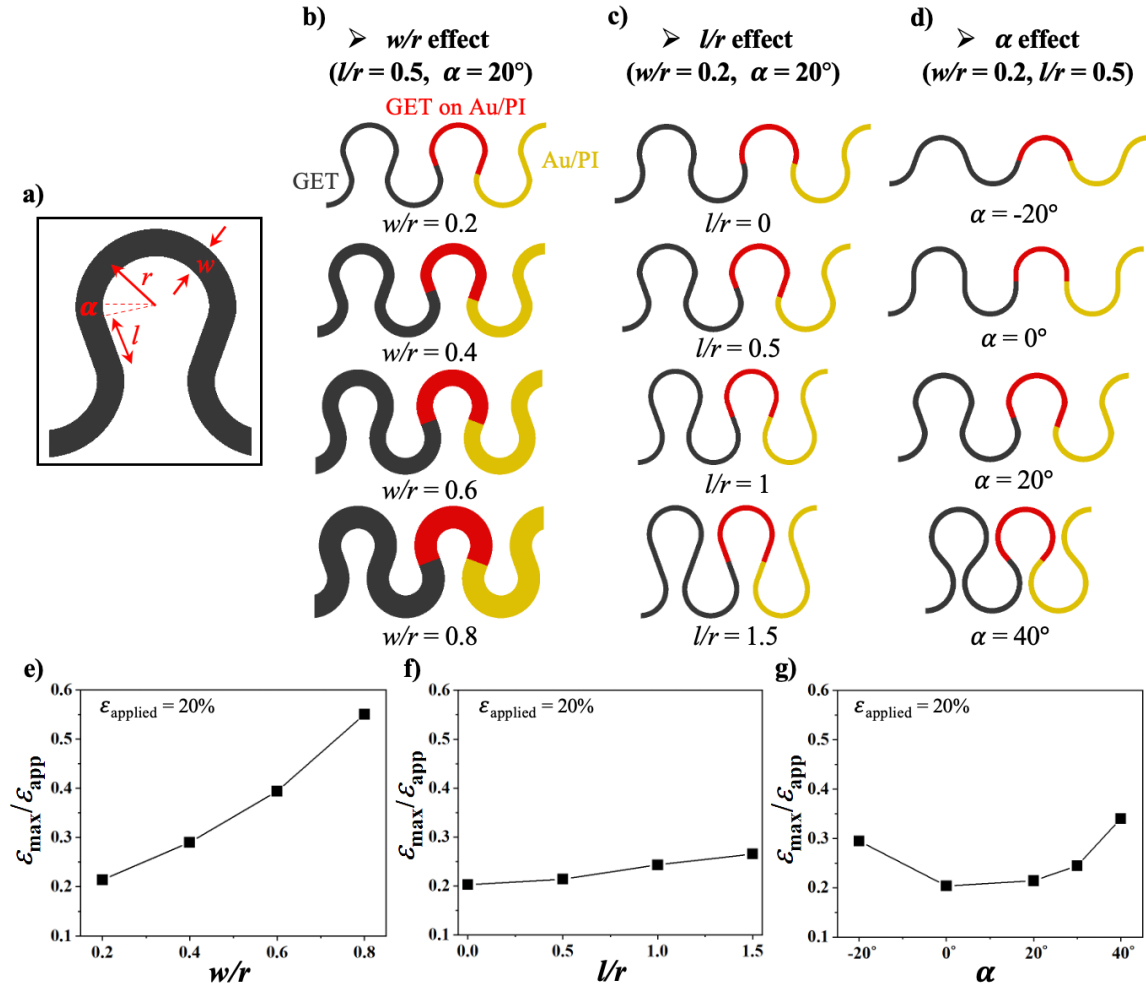


Figure 4.3: Parametric study of HSPR (Arm) geometry. (a) Geometric parameters, (b-d) Schematics of HSPR (Arm) geometry depending on (b)  $w/r$ , (c)  $l/r$ , and (d)  $\alpha$ . Dark grey, red, and yellow indicates GET, GET on Au/PI, and Au/PI, respectively. Strain reduction of HSPR (Arm) depending on (e)  $w/r$ , (f)  $l/r$ , and (g)  $\alpha$ , accordingly.

### 4.3.2 Experimental Stretchability

The widely adopted electrical resistance vs. strain measurements of conductive thin films was used to determine the stretchability. Figure 4.4a displays the end-to-end electrical resistance of ribbons supported by Ecoflex substrates normalized by its initial resistance ( $R/R_0$ ) as a function of the applied uniaxial tensile strain for different types of ribbons including an HSTR (black curve), a straight GET (green curve), an HSPR (Crest) (blue curve) and an HSPR (Arm) (red curve). The two ends of each ribbon are fully clamped to ensure that they are fully subjected to the applied strain. The  $R/R_0$  are measured until the ribbons fully rupture (i.e., when the resistance blows up). The fracture site and the step edge of the Au/PI are highlighted in the corresponding micrographs by red-dashed circles and red arrows, respectively (Figure 4.4a). As expected, fracture occurs at the Au/PI step edge for the HSTR and the HSTR (Crest). For HSPR (Arm), however, fracture happens at the crest of the GET instead of the Au/PI step edge, which implies that the crest of the GET experiences an even larger strain than the GET at the Au/PI step edge. Here, we used more conservative stretchability criteria ( $R/R_0 = 2$ ) because this amount of change is equivalent to the amplitude of electrodermal activity (EDA) signals (tens of kohms) when the HSPR is applied for a wearable EDA sensor. Using  $R/R_0 = 2$  to quantify stretchability, the stretchability of the HSTR is found to be the lowest ( $4.4 \pm 1.1\%$ ), followed by the straight GET ( $9.8 \pm 0.3\%$ ), then the HSPR (Crest) ( $32 \pm 4.7\%$ ), and the highest one is HSPR (Arm) ( $42 \pm 2.6\%$ ). These stretchability results are summarized in a bar chart in Figure 4.4b. The standard deviation is calculated based on three tensile tests on three different specimens of the same configuration. Generally speaking, serpentine ribbons are much more stretchable than straight ones. It is also anticipated that the HSTR would have lower stretchability than the straight homogeneous GET due to the stiffness mismatch at the Au/PI step edge in the HSTR. The stretchability of HSPR (Crest) is lower than that of the HSPR (Arm) is also

reasonable because generally, serpentine inner crests have larger strain than the arms. But with the step edge, this conclusion would require a closer look through FEM. What is out of expectation is that the HSPR (Arm) stretchability is similar to that of a homogeneous serpentine GET ( $48 \pm 3.4\%$ ) (Figure A12). This is because the HSPR (Arm) has the same fracture mode as the homogeneous serpentine GET, i.e., at the crest of the GET away from the Au/PI step edge. It suggests that the anticipated strain concentration at the Au/PI step edge (which is at the serpentine arm) did not exceed the maximum strain of a homogeneous serpentine GET at the crest, which will also need to be validated by FEM.

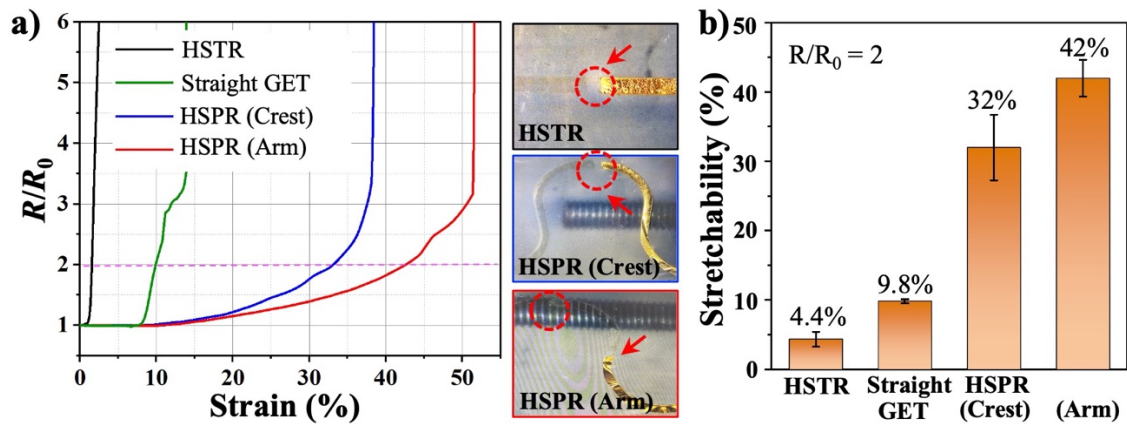


Figure 4.4: (a) The resistance change over strain for the three different configurations in comparison to straight GET. Micrographs at fracture are also shown on the right. Red-dashed circle indicates the location of the fracture. (b) Stretchability comparison for three configurations and straight GET.

The stability of HSPR (Arm) is tested through cyclic strains between 0% to 20% at a frequency of 0.25 Hz. The normalized resistance up to 10,000 cycles are plotted in Figure 4.5. It is noticed that the resistance even decreases slightly with the increasing number of

cycles, which could be attributed to the ribbon-Ecoflex interface delamination under cyclic deformation.

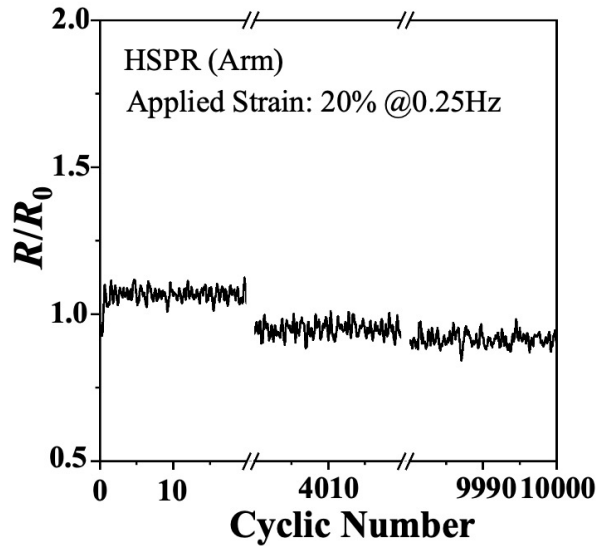


Figure 4.5: Cyclic test of HSPR (Arm) under 20% of applied strain with 0.25 Hz up to 10,000 times.

### 4.3.3 Strain Reduction Validated by FEM Simulation

To explain the experimentally measured stretchability of HSPR, FEM is used to simulate 20% tensile strains applied to the Ecoflex substrate and compare the strain distributions among three different configurations - HSTR, HSPR (Crest), and HSPR (Arm) - as depicted in Figure 4.6a, where the Ecoflex substrate is omitted. The maximum strains of the three configurations are plotted in a bar chart in Figure 4.6b along with the straight GET, which is the same as the applied strain, 20%. It is obvious that the maximum strain in the HSTR is the highest (35%), which is much higher than the applied strain. This

is because the straight Au/PI ribbon is 7.7 times stiffer than the GET, indicating that it is less prone to deformation. As a result, the GET must deform more than the applied strain to accommodate the end-to-end displacement. In contrast, the maximum strain in HSPR (Crest) (6.7%) is much less than the applied strain, which occurs at the inner crest of the GET that also coincides with the Au/PI step edge. The maximum strain in HSPR (Arm) is only 4.3% (highlighted by a pink arrow), which is smaller than that of the HSPR (Crest) (6.7%) although both occur at the crest. Surprisingly, the strain at the step edge is only 0.7%, which best manifests the benefit of HSPR – to locate the step edge at a strategic position of the serpentine such that the strain in GET is insignificant. Compared with the HSTR, the strain in GET at the Au/PI step edge in HSPR (Arm) is reduced by 50 times, simply through geometric engineering of the heterogenous ribbons.

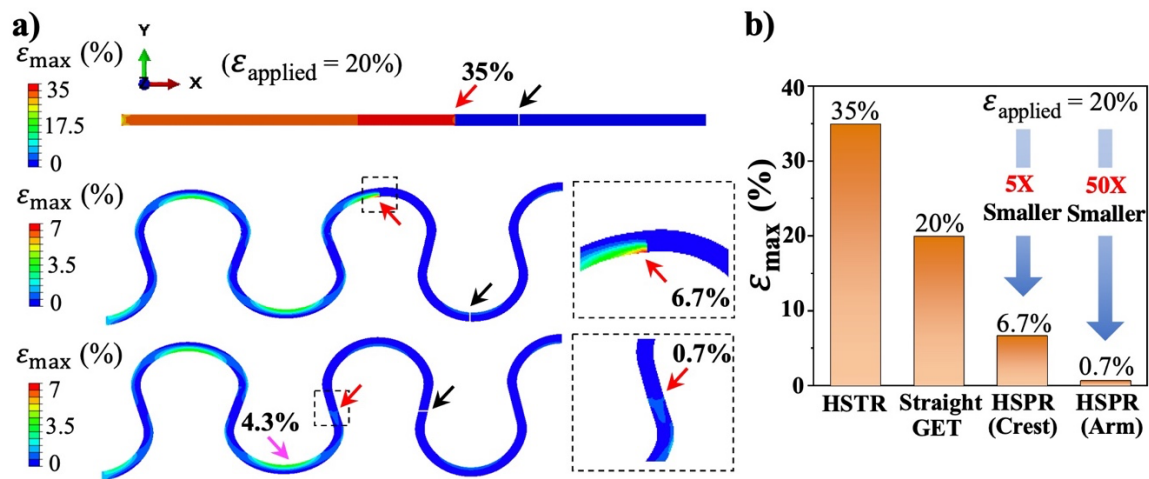


Figure 4.6: (a) FEM results of stretching HSTR, HSPR (Crest), and HSPR (Arm) without showing the Ecoflex substrate. The edge of Au/PI is zoomed in to show the strain in GET at the Au/PI step edge, which is expected to suffer from strain concentration. (b) Comparison of strains at the Au/PI step edge in the heterostructures vs. the homogenous straight GET, which confirms the strain reduction effect in HSPR, especially in HSPR (Arm).

#### 4.3.4 Stretchability Prediction Using FEM Simulation

To quantitatively compare the experimental vs. FEM results, the following brittle fracture criterion [267] is borrowed,

$$\varepsilon_{max}/\varepsilon_{app} = \varepsilon_{cr}/\varepsilon_{app}^{cr} \quad (1)$$

where  $\varepsilon_{max}$  represents the maximum strain calculated in FEM,  $\varepsilon_{app}$  is the applied strain in FEM,  $\varepsilon_{cr}$  is the critical strain-to-rupture of the straight GET measured experimentally (9.8% according to Figure 4.4b), and  $\varepsilon_{app}^{cr}$  is the experimentally determined stretchability. Equation (1) essentially offers a means to compare the FEM result ( $\varepsilon_{max}$ ) with the experimentally measured stretchability ( $\varepsilon_{app}^{cr}$ ), given  $\varepsilon_{app} = 20\%$  and  $\varepsilon_{cr} = 9.8\%$  to be constants. The critical strain-to-rupture of the straight GET is chosen to be  $\varepsilon_{cr}$  because in all the experiments, only GET ruptures, while this behavior is never exhibited by the Au/PI. For the four configurations, Figure 4.7 plots the left of the equation (obtained by FEM) in red, and the right of the equation (obtained experimentally) in blue. The inset is a blown-up view of the black dashed box region. According to previous discussions, HSTR, straight homogeneous GET, and HSPR have  $\varepsilon_{max}/\varepsilon_{app} > 1$ ,  $= 1$ , and  $< 1$ , respectively. While the FEM and experimental results are in good agreement for the straight GET, the HSPR (Crest) and the HSPR (Arm), there is a visible deviation in the case of HSTR. This deviation can be attributed to the limited accuracy in the very small experimentally measured stretchability of HSTR.

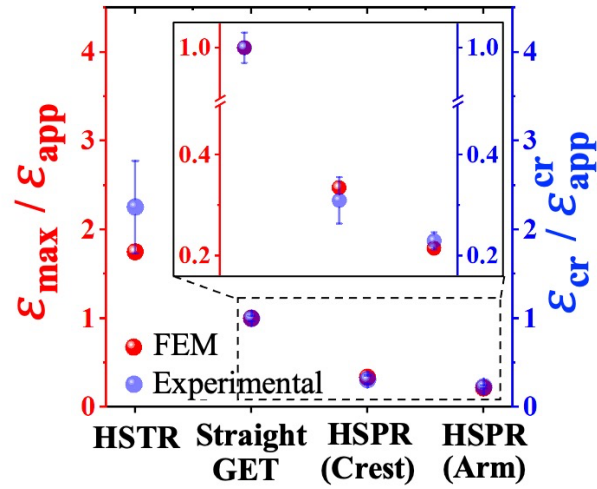


Figure 4.7: Comparison between the normalized maximum strain in FEM and the normalized stretchability in an experiment for different configurations.

### 4.3.5 Stretchability in Transverse Direction

Although it was shown that HSPR especially HSPR (Arm) can significantly alleviate strain in GET under uniaxial strain, it is expected to be much less effective when subjected to transverse strain. To provide a quantitative answer, FEM is carried out and the results are provided in Figure 4.8. When subjected to 20% transverse strain (Figure 4.8a), the maximum strain (in the transverse direction) in both HSPR (Crest) and HSPR (Arm) occur at the new shallow crests with respect to the stretching direction, with very similar values (5.9% vs. 6%) as illustrated in Figure 4.8b,c, respectively. Strains at the Au/PI step edges indicated by the red arrows are only 3.9% and 5.3%, both smaller than 6%. Although the maximum strains are much higher than those appeared under longitudinal stretch, they are still  $\sim 8$  times smaller than HSTR, which means the HSPR designed for longitudinal stretch still has some strain reduction effects even under transverse loading.

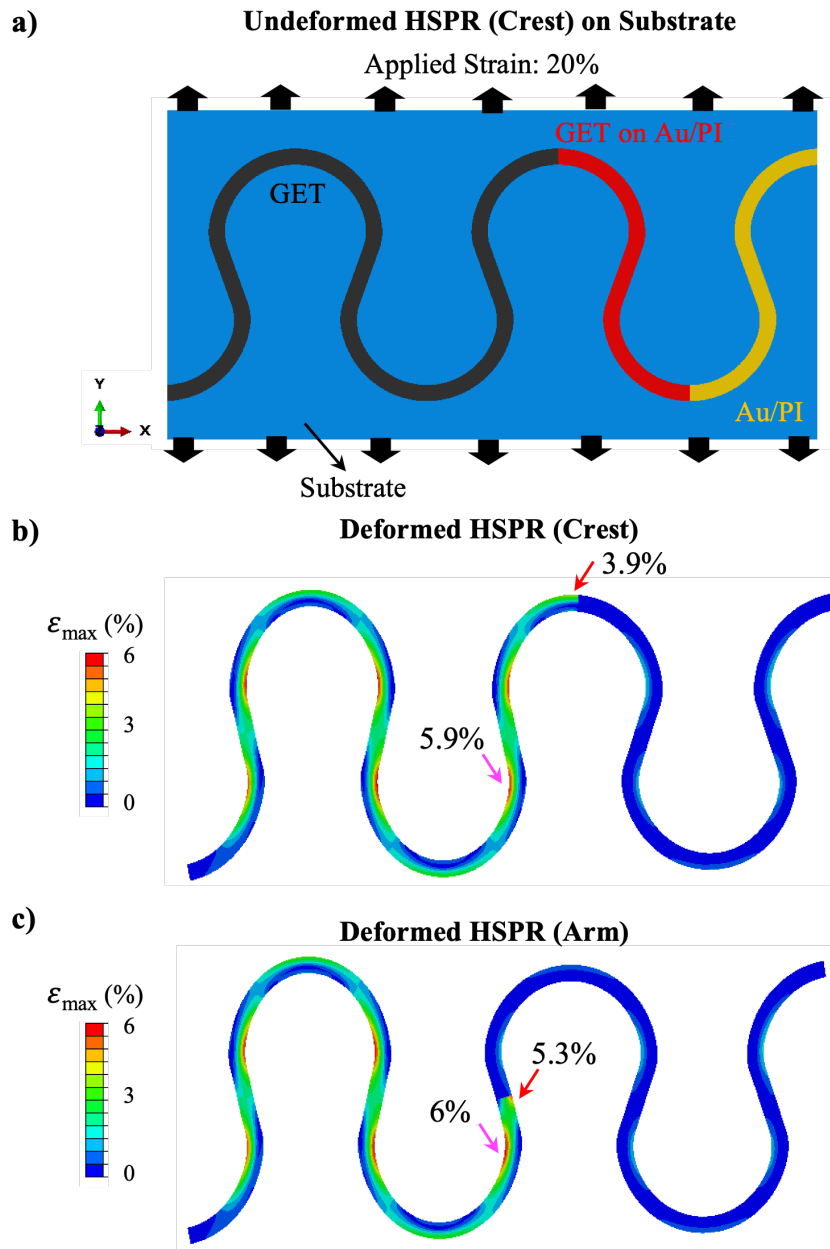


Figure 4.8: Transverse stretching of HSPR in FEM. (a) 300-nm-thin GET is connected to 750-nm-thin Au/PI on a 100- $\mu$ m-thick Ecoflex. 20% of strain is applied in the transverse direction. The FEM simulation results with the edge of contact of Au/PI located at (b) crest and (c) arm of the serpentine are displayed. The pink arrow indicates the global maximum strain, and the red arrow indicates the local maximum strain at the edge of the interface. Ecoflex is not displayed in the simulation results.

### 4.3.6 Stretchability Depending on Stiffness Ratios

The effect of HSPR also depends on the stiffness mismatch between GET and Au/PI. Therefore, FEM is applied to model HSPR (Arm) involving two stiffer electrical connectors of practical use – 13- $\mu\text{m}$ -thick Au/PI and 18- $\mu\text{m}$ -thick Cu, which have a stiffness ratio of 37.6 and 1596 against the 300-nm-thin GET, respectively. Figure 4.9 plots the strain distributions in those two cases along with the 750-nm-thin Au/PI (Figure 4.9a) as a reference, with increasing stiffness mismatch from top to bottom. Interestingly, there is a shift of maximum strain site from the inner crest of GET serpentine to the Au/PI step edge when the stiffness mismatch becomes too high (Figure 4.9c). The corresponding experiments are performed and the results are summarized in Figure 4.10, which plots the stretchability dependence on the stiffness ratio, where the black markers are experimental results, and the red markers are FEM predictions based on Equation (1). The sudden drop of the predicted stretchability for the 18- $\mu\text{m}$ -thick Cu can be attributed to the change of maximum strain site. For this case, there is a larger discrepancy between the experimental and FEM results. It is suspected that this is due to the buckling or delamination of the stiffer electrical connectors in the actual experiments, which is not accounted for in our FEM. Therefore, our current FEM is only applicable to HSPR with relatively small stiffness mismatches, e.g., up to 100.

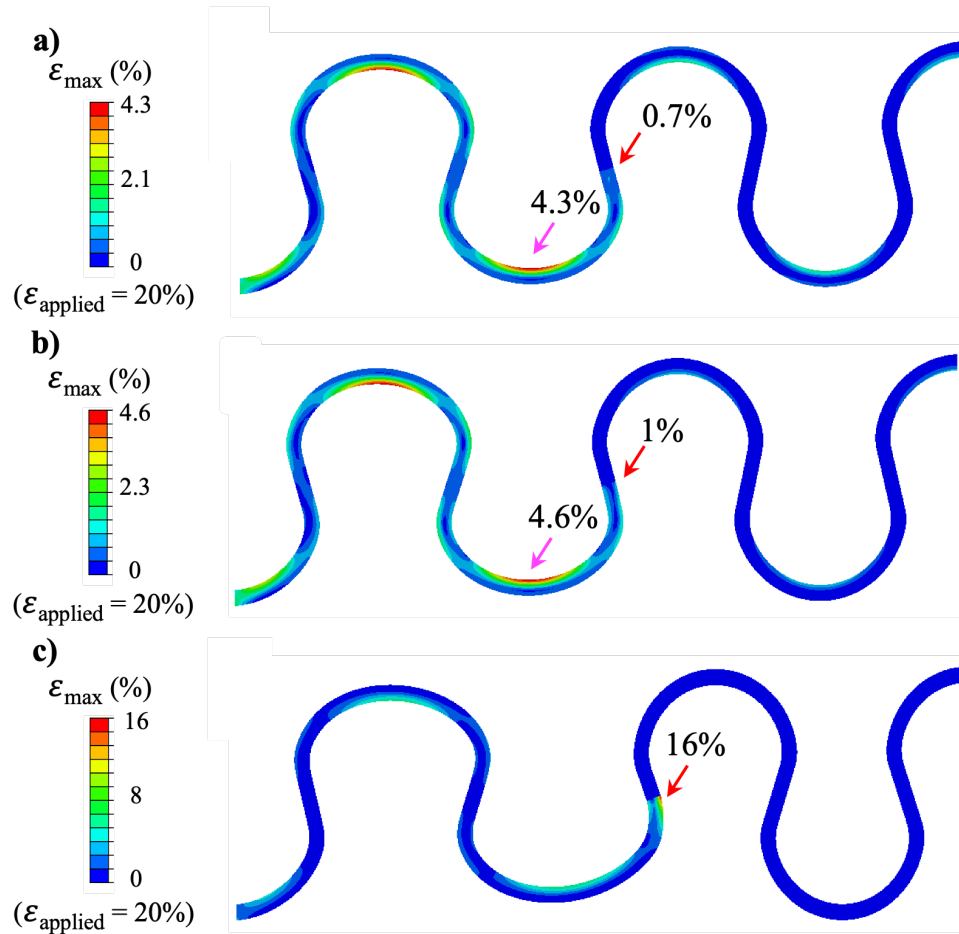


Figure 4.9: The maximum strain on HSPR (Arm) depending on stiffness ratios. The 300-nm-thin GET is connected to (a) 750-nm-thin Au/PI, (b) 13- $\mu\text{m}$ -thick Au/PI, and (c) 18- $\mu\text{m}$ -thick Cu, which has the stiffness ratio of 7.7, 37.6, and 1596, respectively. Red arrows indicate the edge of Au/PI and pink arrows indicate the global maximum strain. The HSPRs are supported by 100- $\mu\text{m}$ -thick Ecoflex, and it is not displayed in the simulation results.

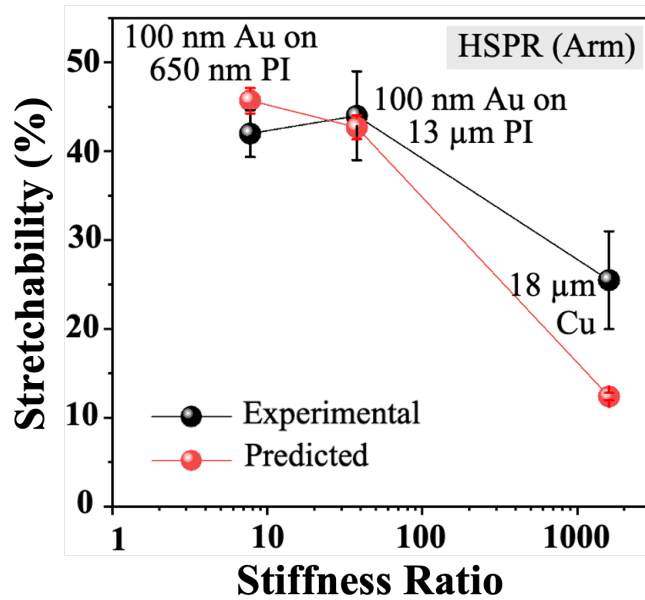


Figure 4.10: Stretchability of HSPR (Arm) with different stiffness ratios.

#### 4.4 SUMMARY

This Chapter introduces the first mechanically robust interface between sub-micron-thin stretchable electrodes and rigid back-end circuits. Using graphene e-tattoos (GET) as an example, heterogeneous serpentine ribbons (HSPR) is applied to significantly reduce the strains in CVD graphene. The HSPR between GET and Au/PI could be simply fabricated using a laminate-cut-paste method. Using finite element modeling (FEM) simulation, the effect of geometric parameters of HSPR is studied. Depending on the relative position of the Au/PI step edge within the serpentine, the HSPR (Arm) offers the most significant strain reduction (50 folds) compared with heterogeneous straight ribbons (HSTR). Moreover, a framework is provided to design or predict the stretchability of HSPR based on FEM. This is a generic method, which can be utilized to reliably connect other

ultrathin electronics (e.g., Au nanomeshes [268], ultrathin AgNWs/PDMS [269], and PEDOT:PSS-based tattoo electrodes [259]) to rigid back-end-circuit. However, the following limitations of this research should be reminded. First, the current FEM does not account for the buckling of HSPR. Second, the prediction of HSPR stretchability does not work when the stiffness mismatch is beyond 100.

## Chapter 5: GET for Ambulatory Long-Term EDA Sensing<sup>7</sup>

Based on the novel interface design, so-called heterogeneous serpentine ribbons (HSPR) introduced in the previous Chapter, an ambulatory wearable sensor based on GET is manufactured. Along with the aid of a soft interlayer, long-term and unobstructive monitoring of electrodermal activity (EDA) on the palm is achieved. The overall sensor design is introduced and validated by numerical and experimental analysis in this Chapter. Furthermore, throughout the EDA detection algorithm and the corresponding statistical analysis, high correlation between GET-based EDA sensor and the gold standard is confirmed. This approach resolves a long-standing challenge of continuous monitoring of EDA on the palm with comfort and minimized motion artifacts.

### 5.1 OBJECTIVE AND OVERVIEW

As COVID-19 caused worldwide social isolation, mental stress and stress management are put in the spotlight. In fact, even before the outbreak of COVID-19, the American Institute of Stress reported 77% of Americans are under mental stress, impacting their physical health [270]. Moreover, based on the statistics by the National Alliance on Mental Illness, 1 in 5 adults in the US have a mental illness [271]. Depression, extreme evasion, and suicidal tendency are posing increasing threats to our population [272]. Therefore, it is critical to continuously monitor the stress level of high-risk patients so that stressful events can be immediately identified, and timely interventions can be offered.

For decades, electrodermal activity (EDA), a.k.a. galvanic skin response (GSR), has been widely used as a quantitative index of mental stress [273–275]. EDA represents the change of skin conductance caused by autonomic sympathetic arousals as 1) the sweat

---

<sup>7</sup>H. Jang, K. Sel, E. Kim, S. Kim, X. Yang, S. Kang, K-H. Ha, R. Wang, Y. Rao, R. Jafari, and N. Lu, Graphene E-Tattoos for Ambulatory Electrodermal Activity Sensing on the Palm Enabled by Heterogeneous Serpentine Ribbons, Nature Communications, Under Review, 2022.

ducts of eccrine sweat glands are filled due to emotion-evoked sweating, then 2) multiple low-resistance pathways are formed, which increases the skin conductance, and finally 3) the skin conductance is recovered as the sweat is reabsorbed or dissipated away [276]. Psychophysiological, the palm is the most recommended site to monitor EDA, specifically the thenar and hypothenar eminences and the medial and distal phalanges of the fingers [277]. It is because the palm has the highest density of eccrine sweat glands which are filled up under psychological stimuli, such as mental stress, primarily [278,279]. Commercial wearable EDA sensors connect silver/silver chloride (Ag/AgCl) gel electrodes placed on the palm to wristband housing measurement circuits through dangling wires. However, this setup poses two major problems for long-term EDA monitoring. First, both gel electrodes and wires are obtrusive to daily activities and cause social stigma. Second, the electrode-to-skin impedance rises as the gel electrodes dehydrate over time and even delaminate from the skin, which degrades the EDA signals. To overcome such limitations, EDA sensors based on dry electrodes have been developed. They tend to measure EDA from different locations on the body, such as the wrists [280–283], the forearms [284], the shoulders [280], and even the back [285]. However, when measured off the palm, the EDA signal can be interrupted by accumulative sweat secreted from the apocrine sweat glands due to the thermo-regulation of our bodies, an effect that is only negligible at the palmar and the plantar regions [286]. Even though a dry and wireless EDA sensor has been applied on the hand in one study [287], its thickness of one centimeter (including FPCB and chips) makes it no less obstructive than commercial gel electrodes. Therefore, an unobstructive and less perceptible palm sensor for mobile EDA monitoring is highly desired.

Ultrathin, tattoo-like wearable sensors have demonstrated superior skin-conformability, imperceptibility, and long-term stability for monitoring various physiological signals, such as ECG, EMG, EEG, skin hydration, and temperature as well

as touch and pressure [256,260,268,269,288–292]. Furthermore, low electrode-to-skin impedance can be achieved due to its high conformability to skin surface textures at the microscale. In fact, the contact impedance between sub-micron-thin dry electrodes and skin is comparable or even lower than that between commercial Ag/AgCl gel electrodes and skin [260,268,292]. Moreover, graphene e-tattoo (GET) with monolayer CVD (chemical vapor deposited) graphene supported by sub-micron-thin PMMA (poly(methyl methacrylate)) can be highly transparent and can match skin stretchability when patterned into serpentine shapes [247]. Therefore, serpentine-shaped GET is an ideal candidate for palm EDA sensing.

Throughout the novel interface design, heterogeneous serpentine ribbons (HSPR), the serpentine-shaped GET is connected to a rigid EDA watch. The Au terminals from the HSPR are enlarged to interface with the rigid electrodes on the EDA watch through a reusable soft interlayer with soft conductive vias. As the watch tightens on the wrist, the soft interlayer is pressed between the watch and the Au terminals so that this contact is also mechanically secured without any adhesive. The mechanical robustness of the soft interlayer is numerically modeled and experimentally validated. An equivalent circuit model for the HSPR-skin interface is established to verify that GET-skin interface impedance is the governing EDA signal compared to Au/PI-skin and Au-graphene interface impedance. A strong correlation of EDA measured with Ag/AgCl electrode and GET is confirmed through statistical analysis. Finally, the unobstructive GET has successfully completed ambulatory EDA monitoring for 15 hours including studying, exercising, driving, sleeping, and so on.

## 5.2 DESIGN AND WORKING PRINCIPLES OF GET-BASED EDA SENSOR

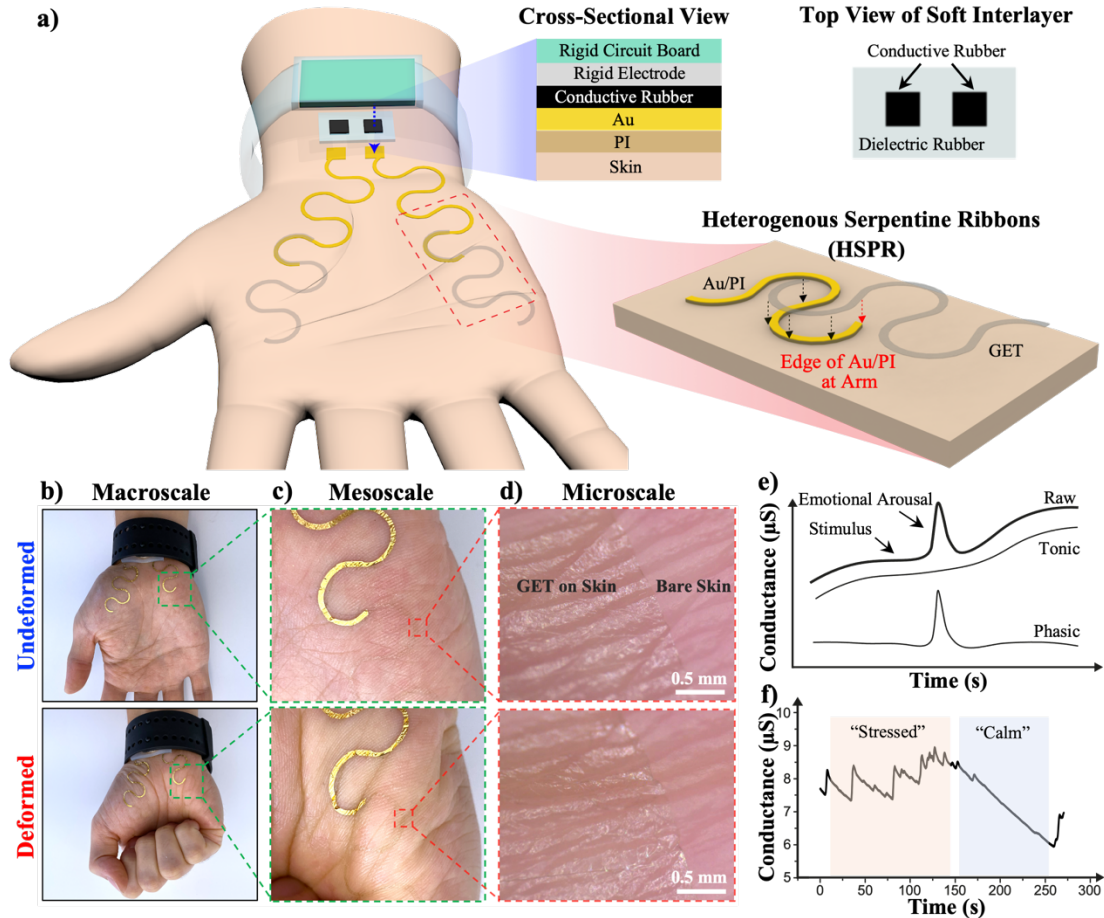


Figure 5.1: A wireless palm electrodermal activity (EDA) sensor based GET connecting to a rigid E4 wristband through HSPR and soft interlayer. (a) An overall device schematic where the detailed structures of the HSPR and the soft interlayer are illustrated in blown-up views. The HSPR is composed of GET serpentine ribbon overlapping with Au/PI serpentine ribbon via just van der Waals forces. The cross-sectional view along the blue dashed arrow illustrates how the Au layer is connected to the rigid electrode built into the wristband through a conductive rubber. (b-d) Photographs showing GET EDA sensor on the palm when the hand is undeformed and deformed in macroscale, mesoscale, and microscale, highlighting two main features of GET – transparency and skin-conformability. (e) A representative EDA signal with both low-frequency tonic component and high-frequency phasic component illustrated. (f) Example EDA signals.

Figure 5.1a displays a schematic of the proposed GET-watch interface through HSPR and a vertically conductive soft interlayer. As a generic illustration, Figure 5.1a draws a conventional wristwatch that comes with rigid electrodes on the bottom of the crown enclosing a rigid circuit board. Two GET serpentine are resting on the thenar and hypothenar eminences of the palm with graphene directly touching the skin. To connect the GET to the two rigid electrodes, the GET is partially laminated over an Au/PI serpentine ribbon with graphene touching the Au, forming the HSPR. As the GET and Au/PI have similar sub-micron thickness, they can laminate on the skin and with each other just through vdW interactions. An exploded view of the red-dashed-line-boxed HSPR is offered at the lower right. Note that GET is on top of Au/PI such that there is a step edge under the GET where the Au/PI ribbon terminates. The amount of strain reduction depends on the specific location of this step edge, which will be quantified through experiment and FEM later. The other terminal of the Au/PI located on the wrist is patterned into a square shape with Au facing up. A silicone-based soft interlayer with two separate conductive rubber zones as illustrated in the upper right is added as a mechanical buffer layer between the Au nanomembranes and the rigid electrodes on the wristband, to prevent Au from experiencing excessive stresses directly from the rigid electrodes. The cross-sectional view along the blue-dashed arrows is expanded to illustrate the vertical lamination of different materials, starting from the rigid circuit board on the top down to the skin (thickness is not drawn to scale).

Figures 5.1b to d are photographs of GET EDA sensor on the palm without and with deformation in macroscale, mesoscale, and microscale, respectively. The rigid electrodes from a commercial EDA watch (E4 wristband, Empatica Inc.) are connected to Au/PI through the soft interlayer. It is evident that the GET and even the HSPR are not obvious on the palm given the transparency of GET and the narrow (1-mm-wide) Au/PI

serpentine. The thinness of GET (300 nm) and Au/PI (750 nm) makes them mechanically imperceptible and unobstructive to the motion of the hand. Furthermore, the microscale images in Figure 5.1d validate that GET is fully conformable to the microscopic surface morphology of skin even under deformation. Figure 5.1e illustrates that when psychological or physiological arousal is present, the skin conductance exhibits an abrupt increase followed by a swift recovery. Such high-frequency signals constitute the phasic components of the skin conductance, which are called the skin conductance response (SCR) [274]. The low-frequency change in skin conductance is called the tonic response, which comes from autonomous arousals and is considered much less meaningful in stress analysis than SCR [293]. By examining the SCR signals over time, as illustrated in Figure 5.1f, the stress level can be quantitatively determined [278,280].

## 5.3 STRAIN ISOLATION BY SOFT INTERLAYER

### 5.3.1 Experiment

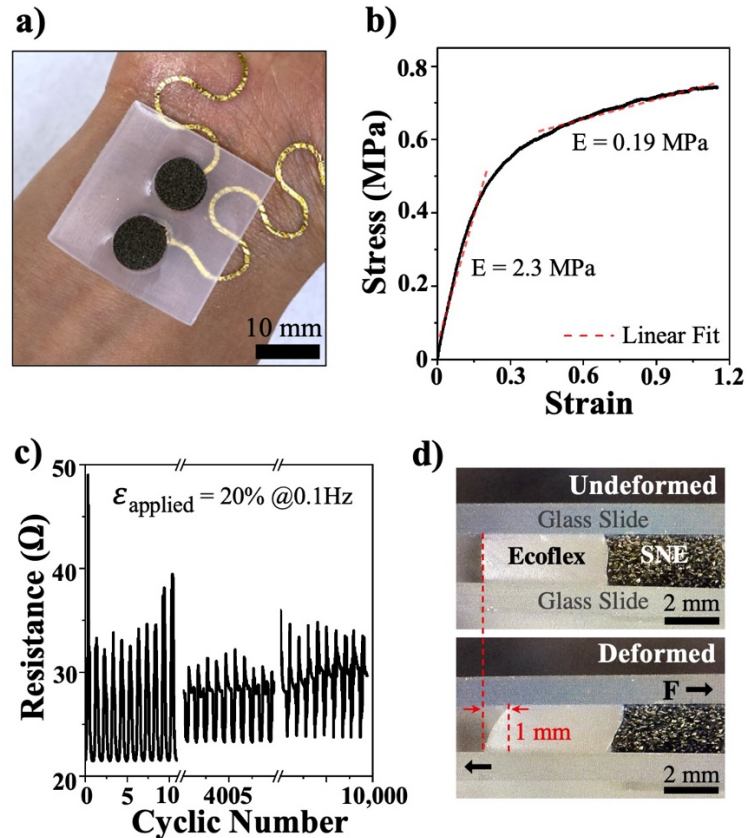


Figure 5.2: Experimental characterization of the soft interlayer. (a) Photograph of soft interlayer covering the Au/PI laminated on the human wrist. (b) Stress-strain curve of the commercial conductive silicone rubber (SNE-553). (c) Cyclic test of SNE-553 under 20% of compressive strain with 0.1 Hz to confirm the stability of resistance. (d) Side-view of Ecoflex and SNE-553 sandwiched by glass slides before and after a shear displacement of 1 mm.

While the HSPR is very effective in limiting strains in the GET, 100-nm-thin Au on 650-nm-thin PI is also mechanically fragile. Because 100-nm-thin Au is nanocrystalline,

it is prone to brittle fracture. In fact, our previous experiment has confirmed that its stretchability is only 1% when supported by 300-nm-thin PMMA [247]. Moreover, given the limited adhesion between Au and PI, the Au layer is easy to flake off when it is in direct contact and scrubbed by any rigid object. To achieve a mechanically reliable interface with rigid electrodes on the crown of the wristband, it is proposed to insert a soft Ecoflex interlayer embedded with two black conductive rubber disks of 8-mm diameter, as displayed in Figure 5.2a, in between the Au and the watch. The conductive rubber disks (SNE-553, Stockwell Elastomerics Inc.) are made out of silicone doped with Ni nanoparticles coated with graphite. They are tested to have low modulus (2.3 MPa, Figure 5.2b) and low vertical resistance ( $< 50$  Ohms) under 20% of compressive strain, even up to 10,000 cycles (Figure 5.2c). The resistance change due to cyclic compression is only about 10 Ohms, which is insignificant compared to the resistance change due to EDA (tens of kOhms).

### 5.3.2 FEM Simulation

Through FEM, it is validated that the soft interlayer is effective in isolating the strain induced in the Au by the movement of the wristband. For the FEM simulation of the soft interlayer, the commercial software ABAQUS (standard 6.13) was used and a general static step with nonlinear geometry was implemented. Ecoflex, SNE-553, and PI were modeled as 2D deformable planes and Au was modeled as a 1D beam. Ecoflex was modeled as a nearly incompressible Neo-Hookean hyperelastic material with a modulus of 0.1 MPa and Poisson's ratio of 0.475. SNE-553 was modeled as a nearly incompressible Neo-Hookean hyperelastic material with a modulus of 2.2 MPa and Poisson's ratio of 0.475. PI was modeled the same as described in the section above. The bottom of PI was

fixed, and the displacement was applied on the top edge of Ecoflex and SNE-553 to find the strain distribution on the structure due to the shear lag. First, the soft interlayer is sandwiched between two rigid glass slides and apply a shear force by hand to estimate an attainable shear displacement (1 mm as shown in Figure 5.2d). We apply this shear displacement to our 2D cross-sectional FEM as illustrated in Figure 5.3a, in which two red arrows point to two material discontinuity points. The soft interlayer to Au interface is assumed to be perfectly bonded. The corresponding FEM result is plotted in Figure 5.3b. The red-dashed box highlights the strain concentration points which correspond to the two discontinuity points. The two magnified views clearly indicate the maximum strains in Au are negligibly small (0.00028% and 0.0049%) compared to the yield strain of Au (~0.2%). In contrast, the strain induced in Au would reach 1% (fracture strain of Au) under very tiny displacement (2.5  $\mu\text{m}$ ) without the soft interlayer (Figure 5.4). In addition to previous examples where soft interlayers were used to isolate substrate strain from stiff functional device islands [294,295], this is another embodiment of strain isolation through the shear lag mechanism.

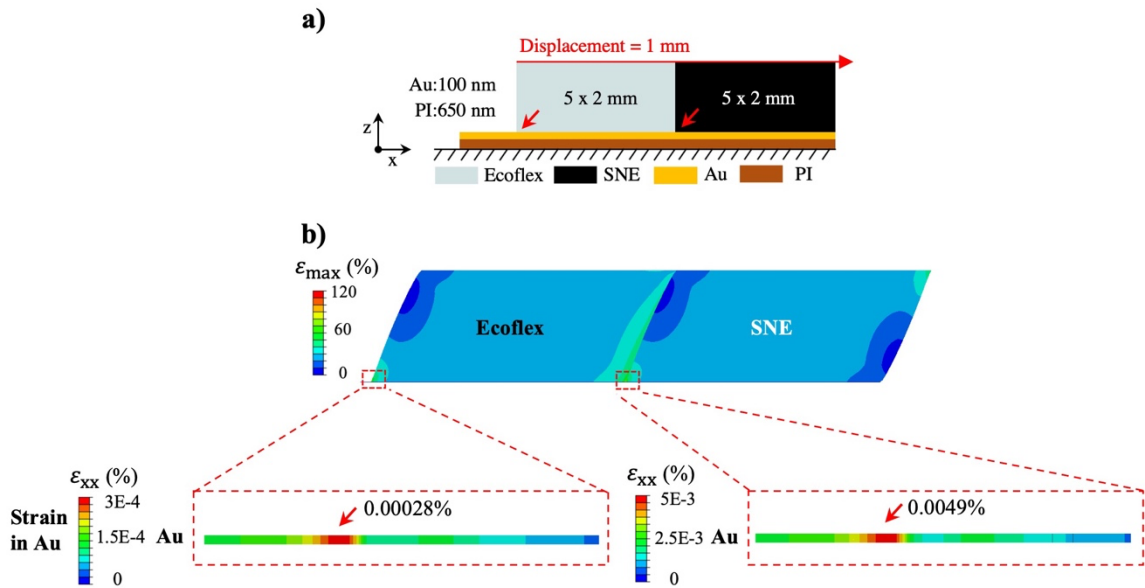


Figure 5.3: Strain isolation effect of the soft interlayer. (a) FEM schematic to validate the strain isolation by the soft interlayer. Red arrows indicate the areas of interest with potential strain concentration. (b) FEM results showing the overall strain distribution and zoomed-in strain in Au at the areas of interest.

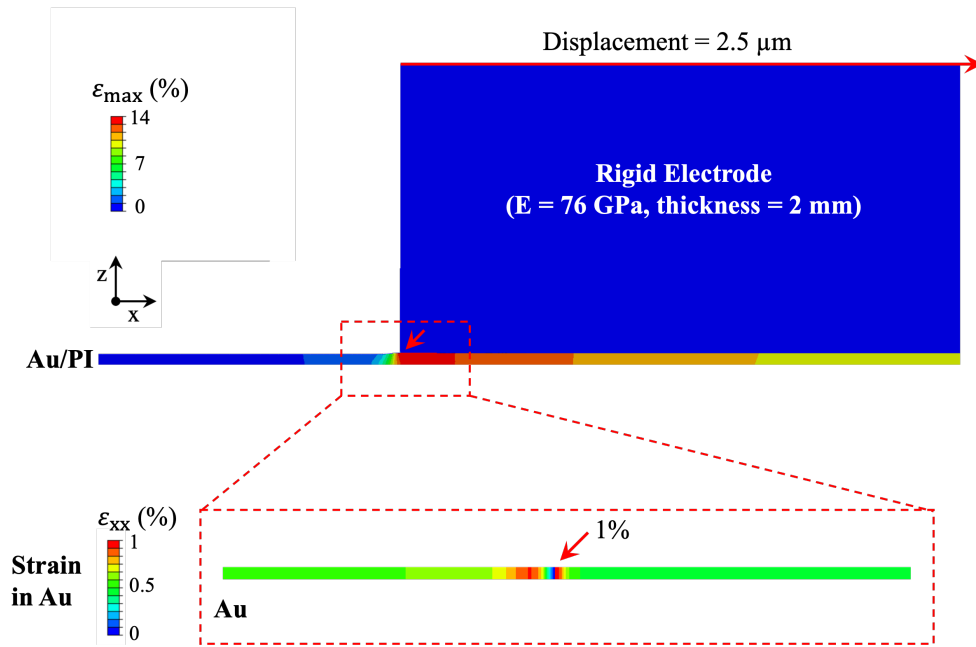


Figure 5.4: FEM simulation results showing the maximum strain in Au without the soft interlayer.

## 5.4 ELECTRODE-TO-SKIN INTERFACE CHARACTERIZATIONS

### 5.4.1 Electrode-to-Skin Impedance Measurements

Before carrying out EDA measurement with GET, it is crucial to develop a thorough understanding of the electrode-to-skin interface impedance to use GET for EDA because many components are added between the wristband and the skin to use GET for EDA monitoring. Figure 5.5a exhibits an HSPR GET sensor and a commercial gel-based reference sensor attached to the same palm. For a fair comparison, both sensors are connected to the same type of hardware (E4 wristband) to acquire the EDA signals. It is obvious in Figure 5.5a that the gel electrodes and the dangling wires are more visible and obstructive than the GET sensor. Using a HIOKI 3532-50 LCR meter, the electrode-to-skin impedance is measured from 42 Hz to 1000 Hz, using rectangle GET and circular gel electrodes of the same size of 1.5 cm<sup>2</sup>. The results in Figure 5.5b clearly suggest that given the same apparent size, the GET could achieve lower contact impedance with the skin than the gel electrodes, which is consistent with our previously published results on GET [260]. This phenomenon is attributed to the perfect conformability of the GET to the microscopically rough skin surface. Moreover, it should be noted that we didn't characterize noise effect for the electrode-to-skin impedance measured by GET. However, we expect that most of the noises will come from the non-ideality induced by the mismatch of two electrodes at the electrode-to-skin interface, and it would be negligible due to 1) identical electrode size, 2) AC current injection, 3) same dermatome for the placement of both electrodes, and 4) perfect conformability of the electrodes on the skin.

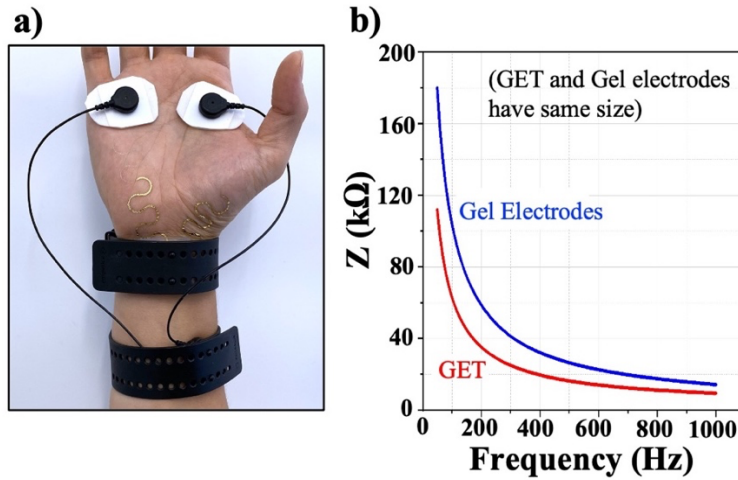


Figure 5.5: Electrode-skin interface impedance characterization. (a) A photograph of HSPR and gel electrodes connected to two identical E4 wristbands. (b) Impedance vs. frequency measured for GET (blue) and gel electrodes (red) of the same diameter.

#### 5.4.2 Modeling Conformability

Such conformability can be analytically confirmed based on our previous mechanics models [210,296] and GET parameters [260]. For a typical skin texture which is assumed to be sinusoidal with wavelength  $\lambda = 250 \mu\text{m}$  and semi-amplitude  $h_0 = 50 \text{ mm}$ , given a 2D plane strain modulus of the skin ( $\bar{E}_s = 130 \text{ kPa}$ ) and a weak electrode-skin interface adhesion ( $\gamma = 18 \text{ mJ/m}^2$ ), a membrane with  $\bar{E}_m = 2.83 \text{ GPa}$  has to be thinner than 475 nm to fully conform to the skin (Figure 5.6a). In fact, this is why we choose the GET to be 300 nm thin. In contrast, the 750-nm-thin Au/PI is beyond the critical conformability thinness and hence can barely conform to the skin. The two micrographs of GET on the skin and Au/PI on the skin in Figure 5.6b qualitatively confirm this analytical prediction.

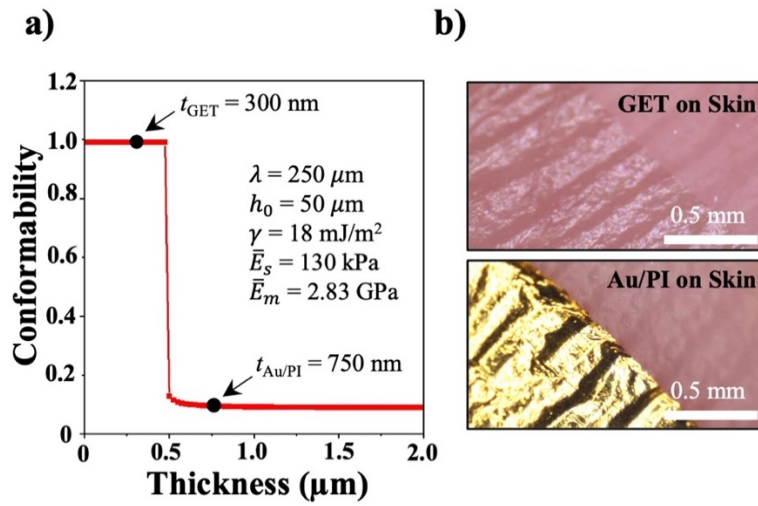


Figure 5.6: (a) Analytical prediction of conformability of PI on the skin depending on its thickness. (b) Micrographs of 300-nm-thin GET (top) and 750-nm-thin Au/PI (bottom) laminated on human skin. It is obvious that only GET can fully conform to the skin, which is consistent with the analytical prediction.

### 5.4.3 Established Equivalent Circuit Model

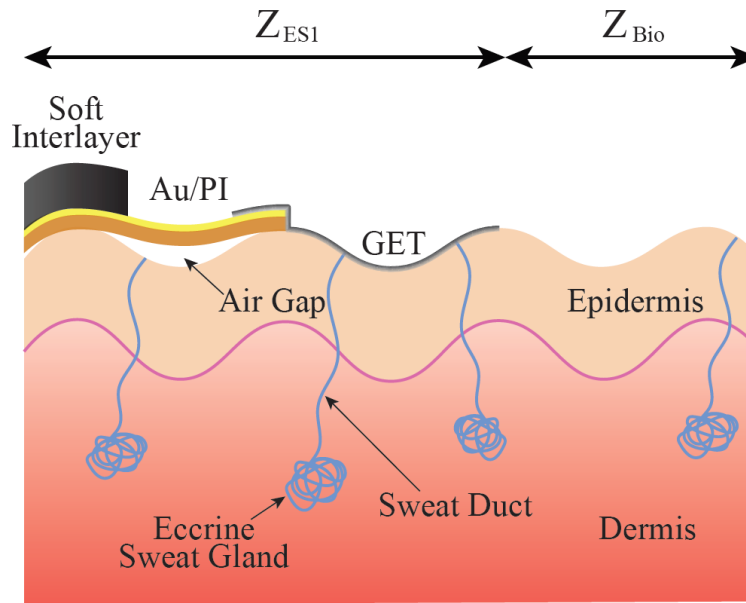


Figure 5.7: Schematic of electrode-skin interface cross-section.

Based on the conformability information, a cross-sectional schematic is built to illustrate the complete electrode-to-skin interface in Figure 5.7. Note that this drawing only displays one single electrode-to-skin interface and in real EDA measurement, one more identical electrode is needed to complete the circuit. In Figure 5.7, the skin is simplified into an epidermis-dermis bilayer where eccrine sweat glands are embedded in the dermis layer and connected to the surface of the epidermis through sweat ducts. From right to left, GET fully conforms to the wavy surface of the epidermis, and Au/PI partially conforms to the epidermis and hence air gaps exist between Au and skin. The soft interlayer covers the Au and connects to a rigid electrode on the E4 wristband (not drawn).

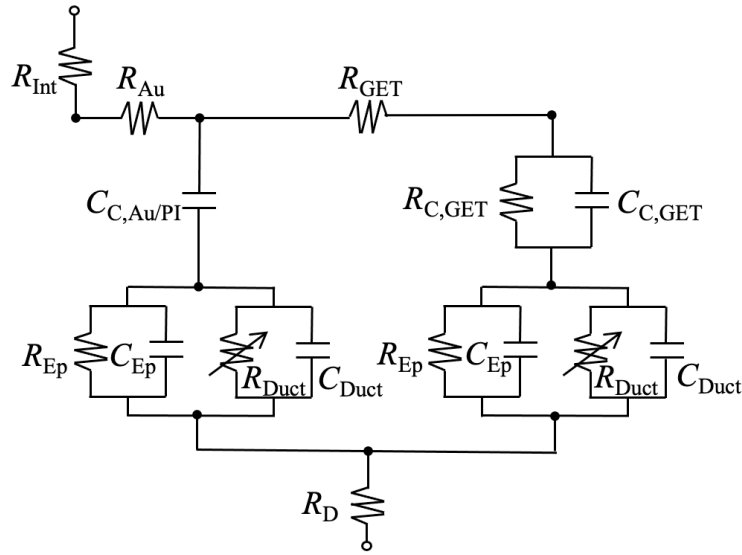


Figure 5.8: The corresponding circuit models to the schematic of electrode-skin interface cross-section.

Parameters	Value	Parameters	Value
$R_{\text{int}} (\Omega)$	30	$C_{\text{C,GET}} (\text{nF})$	1400
$R_{\text{Au}} (\Omega)$	5	$R_{\text{Ep}} (\text{k}\Omega)$	145.6
$C_{\text{C,Au/PI}} (\text{nF})$	7.6	$C_{\text{ep}} (\text{nF})$	21.4
$R_{\text{GET}} (\text{k}\Omega)$	40	$\Delta R_{\text{Duct}} (\text{k}\Omega)$	20 – 100*
$R_{\text{C,GET}} (\text{k}\Omega)$	87.2	$R_{\text{D}} (\Omega)$	326*

Table 5.1: Values of circuit parameters either from literature (indicated by \*) or from our own measurements.

According to this schematic, an equivalent circuit is built in Figure 5.8 starting from the conductive soft interlayer to Au/PI, GET, epidermis, and dermis to help determine which components play a significant role in the EDA measurement. In this circuit model, the contact resistance between GET and Au/PI is ignored since the contact resistance between graphene and Au becomes negligible ( $< 1$  Ohm) when the contact area is in the  $\text{mm}^2$  scale [297,298]. Furthermore, we ignored the half-cell potential at the interface between GET and the skin since the potential difference between the two electrodes will be negligible because both electrodes are placed on the same palm (same dermatome) and AC is injected. The Au-skin interface is separated by the dielectric PI layer, so it is modeled as a contact capacitor ( $C_{C, \text{Au/PI}}$ ). In contrast, the graphene is in direct contact with the skin, so this interface is modeled to have parallel ohmic and capacitive components ( $R_{C, \text{GET}} || C_{C, \text{GET}}$ ). Epidermis and dermis are represented as an RC circuit ( $R_{\text{Ep}} || C_{\text{Ep}}$ ) and a resistor ( $R_{\text{D}}$ ), respectively. Finally, sweat ducts are modeled as a varying resistor parallel with a constant capacitor ( $R_{\text{Duct}} || C_{\text{Duct}}$ ), and the change in the resistance ( $\Delta R_{\text{Duct}}$ ) due to EDA is known to be 20 – 100 kOhms [299]. To determine the rest of the parameters in this simplified circuit model, varying frequencies are applied to find one component at a time. The detailed measurement and calculation methods can be found below, and the results of the parameters are listed in Table 5.1.

Two electrodes are used to measure skin conductance through the skin and assume these two electrodes are identical. Also, the impedance through the deep skin or dermis is negligibly smaller than the electrode-to-skin impedance. Therefore, it can be defined the total impedance as follows:

$$|Z_{\text{total}}| = |Z_{\text{ES1}} + Z_{\text{Bio}} + Z_{\text{ES2}}| = |Z_{\text{ES1}} + Z_{\text{ES2}}| = |2Z_{\text{ES1}}| \quad (2)$$

where  $Z_{\text{total}}$  means the total impedance,  $Z_{\text{Bio}}$  denotes impedance of dermis,  $Z_{\text{ES1}}$  and  $Z_{\text{ES2}}$  indicate electrode-to-skin impedance for electrode 1 and electrode 2, respectively. To find the parameters of the equivalent circuit model as shown in Figure 5.8, first the circuit model is simplified for epidermis and dermis as an equivalent RC circuit to find the  $R_{\text{Ep}}$  and  $C_{\text{Ep}}$  using two Ag/AgCl gel electrodes. Now the simplified circuit model looks as shown Figure 5.9.

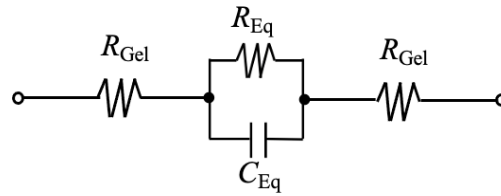


Figure 5.9: The simplified equivalent circuit model between gel electrodes and the skin.

First, to find  $R_{\text{Gel}}$ , an infinitely high frequency (we used 1MHz) was applied, and the impedance was measured. Second, to find the  $R_{\text{Ep}}$ , DC (0Hz) was applied, and initial impedance was recorded to avoid the impact of the polarization. Finally, a frequency in the working range of EDA measurement ( $<100\text{Hz}$ , we used 42Hz) was applied to find  $C_{\text{Ep}}$  by using the following equation:

$$|Z_{\text{total}}| = 2 * R_{\text{Gel}} + \frac{1}{\sqrt{\left(\frac{1}{R_{\text{Ep}}}\right)^2 + (2\pi f C_{\text{Ep}})^2}} \quad (3)$$

where  $f$  is the applied frequency (42 Hz). After  $R_{\text{Ep}}$  and  $C_{\text{Ep}}$  were found, Au/PI electrode was applied on the same location of skin and now the equivalent circuit becomes as illustrated in Figure 5.10.

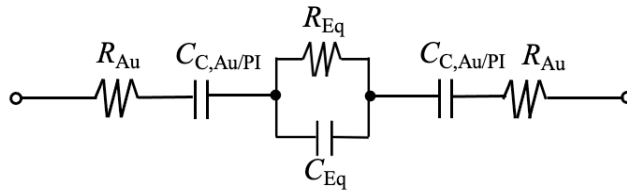


Figure 5.10: The simplified equivalent circuit model between Au/PI and the skin.

To find  $C_{C, Au/PI}$ , we applied 42 Hz and measured the total impedance. Then, the following equation was used to deduce the value of  $C_{C, Au/PI}$ :

$$|Z_{total}| = 2 * R_{Au} + 2 / \sqrt{(2\pi f C_{C,Au/PI})^2} + \frac{1}{\sqrt{\left(\frac{1}{R_{Eq}}\right)^2 + (2\pi f C_{Eq})^2}} \quad (4)$$

where  $f$  is the applied frequency (42 Hz). Finally, GET is laminated on the skin to form HSPR and now the equivalent circuit becomes as shown in Figure 5.11.

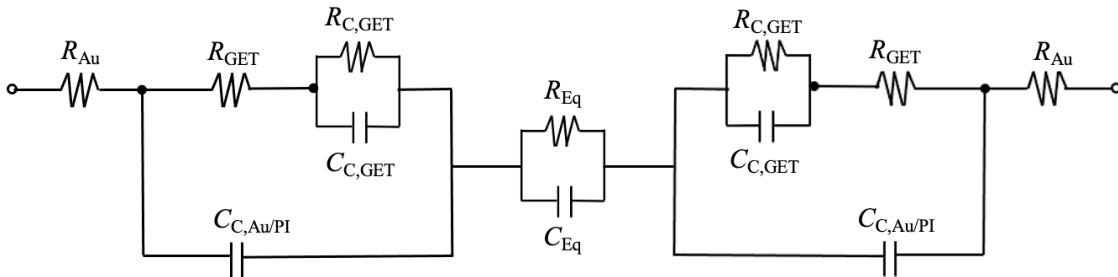


Figure 5.11: The simplified equivalent circuit model between HSPR and the skin.

Same as the first step to find the  $R_{Ep}$  and  $C_{Ep}$ , DC (0 Hz) was first applied to find the  $R_C$ ,  $R_{C, GET}$ , and 42 Hz was applied to find the  $C_{C, GET}$ .

It should be noted that all capacitances are obtained at the frequency of 42 Hz, which is well within the frequency range of EDA (< 100 Hz). The measured  $R_{Ep}$  is comparable to the known reference value (100 kOhms) and  $R_D$  is taken from a reference.<sup>[49]</sup> The GET-skin interface resistance ( $R_{C, GET}$ ) is found to be 87.2 kOhms. As the contact capacitance of GET ( $C_{C, GET}$ ) is found to be ~180 times higher than that of Au/PI ( $C_{C, Au/PI}$ ), it is confirmed that the Au/PI-skin contact impedance is much higher than that of the GET-skin. Thus, it is concluded that the GET is the only sensing electrode of EDA in our measurement setup.

## 5.5 EDA MEASUREMENT AND STATISTICAL ANALYSIS

### 5.5.1 EDA Testing Protocol

Session #	(1)	(2)	(3)	(4)	(5)
<b>Duration</b>	30 s	200 s	30 s	400 s	120 s
<b>Mental State</b>	“Expectation”	“Uncontrolled” Emotional	-	“Controlled” Emotional	“Habituation”
<b>Content</b>	Instruction	Blank image	-	Scaled affective pictures	An affective picture
<b>Detail</b>	Explain structure of the test	Subject-induced random mental arousals	-	10s of exposure and 30s of recovery (total 10 pictures)	10s of exposure and 30s of recovery (3 times)

Table 5.2: An EDA testing video consisting of five different sessions – Expectation, “Uncontrolled” Emotional, Expectation (identical as session #1), “Controlled” Emotional, and “Habituation.”

After the sensor design, fabrication, and theoretical verification, GET is ready to be applied for EDA sensing. The EDA was measured simultaneously with the GET sensor and the gel sensor for statistical comparison. To collect EDA signals from human subjects, a 13-minute testing video consisting of 5 different sessions is built and summarized in

Table 5.2. The video contains two brief introductions about the testing procedure (Sessions (1) and (3) in Table 5.2) and three main EDA testing sessions: “uncontrolled” emotional, “controlled” emotional, and “habituation”. During the 200-second “uncontrolled” emotional session, the human subjects were presented with a blank screen, so their thoughts were unaffected, which resulted in random mental arousals. During the 400-second “controlled” emotional session, the participants were presented with a series of scaled affective pictures. Those scaled affective pictures are taken from the EmoMadrid database [300] and the details about each picture used are listed in Table A1. Finally, during the “habituation” session, a single affective picture was shown three times to study whether the arousal level decreases as the number of repetitive exposure increases. Human subjects were watching the testing video in a quiet room alone while wearing both GET and gel sensors on the same palm. However, it should be remarked that the EDA signals are complex autonomous emotional regulations, which cannot be controlled by people’s consciousness. Therefore, the EDA responses from untrained human subjects exhibit some randomness. In this study, the EDA tests are carried out purely for the purpose of device validation, instead of physiological assessment or stress level quantification.

### 5.5.2 EDA Measurement

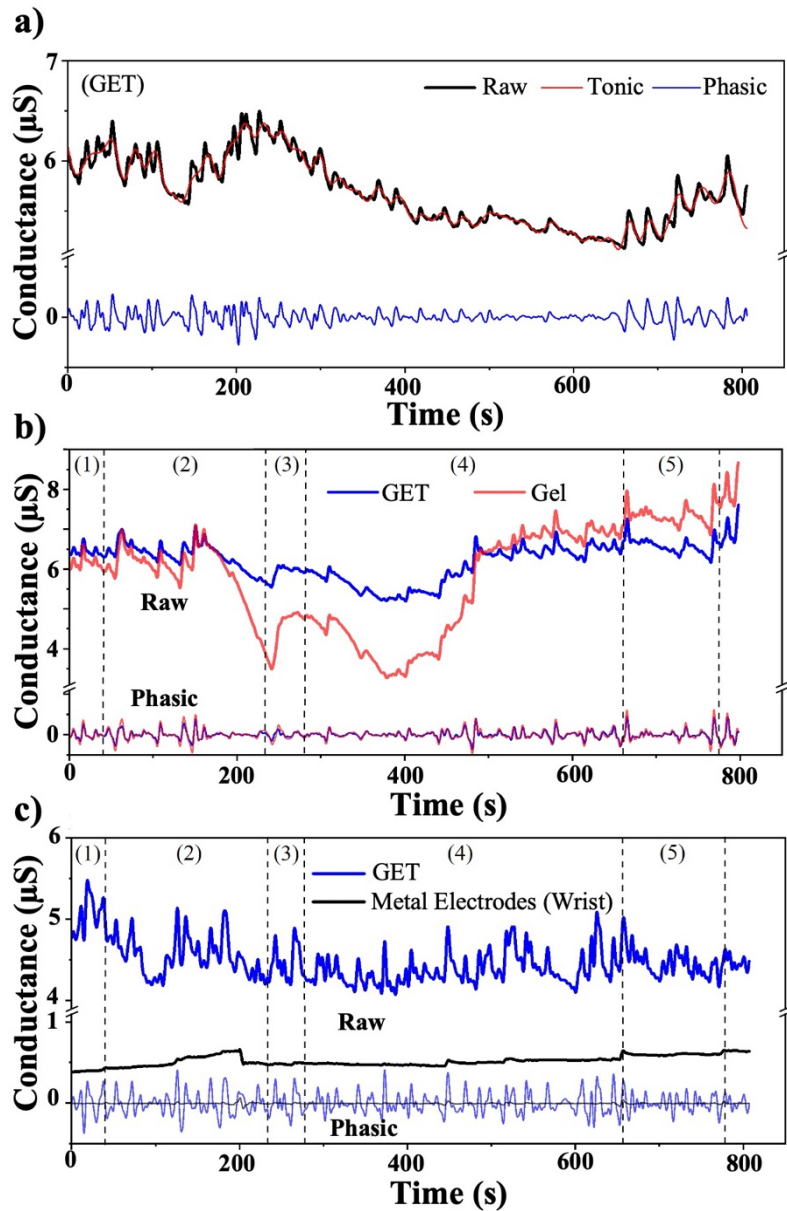


Figure 5.12: (a) Raw data and decomposed data of EDA measured by the GET sensor. (b) Comparison of EDA measured by GET (blue) vs. gel electrodes (red) on subject #1. (c) Comparison of EDA measured by GET on the palm (blue) vs. dry metal electrodes on the wrist (black).

Figure 5.12a plots 800 seconds of raw EDA signals measured by GET sensor (black), and its decomposition into the tonic component (skin conductance level (SCL), red) and the phasic component (skin conductance response (SCR), blue). Only the SCR is considered as event-related EDA responses caused by mental or physical stress. To compare GET-measured EDA signals with gel-measured ones, a total of five EDA tests were conducted with five different human subjects (subject #1 - #5) and the results are given in Figure 5.12b and Figure A13, where blue curves are GET-measured EDA and red curves represent gel-measured EDA. In general, the GET-measured EDA has much less fluctuation in the tonic component (i.e., SCL), but is almost indistinguishable in the phasic component (i.e., SCR), compared with the gel-measured EDA. For the “habituation” session, no correlation between EDA responses and the number of repetitive exposures was observed. Perhaps, the random arousal from the human subjects dominates the EDA signals during this session. This indicates that the performance of our EDA GET sensor is comparable to the gold standard. The rigid electrodes built in the E4 wristband was also used to measure EDA from the wrist. However, no meaningful phasic components could be found, as indicated by the black curves in Figure 5.12c. Therefore, only gel electrodes placed on the palm connected to the E4 watch can obtain EDA signals comparable to that measured by our GET sensor.

### **5.5.3 SCR Detection Algorithm and Statistical Analysis**

To statistically compare GET-measured and gel-measured EDA signals, an algorithm is built to detect and select good SCRs for the correlation analysis. Figure 5.13 provides a flow chart to illustrate our SCR selection process. Firstly, the EDA raw signals acquired by GET and gel electrodes are synchronized by aligning their overall shapes. Also, a 6<sup>th</sup> order Butterworth low-pass filter at 0.2 Hz is applied to mitigate high-frequency

noise from the synchronized signals. As highlighted in Steps (i) and (ii) of Figure 5.13, the trough-to-peak (TTP) method is used to detect the onset of candidate SCRs for the statistical analysis, and a band-pass filter (0.045 – 0.2 Hz) is applied to extract the phasic component of the raw signals. Candidate SCRs are then sent to the event selection policy to count the total number of the SCRs and select only good SCRs which meet the threshold (e.g., 10% of max amplitude and 90% of recovery), as highlighted in Step (iii) of Figure 5.13. A minimum of  $0.05 \mu\text{S}$  SCR threshold amplitude is selected to avoid incorrect measurements due to motion artifacts and other noise contributions. The output of the Ledalab marks the time values of all candidate SCR event onsets. This onset timing information is used in conjunction with the phasic EDA signals to identify SCR events that will be used in statistical analysis.

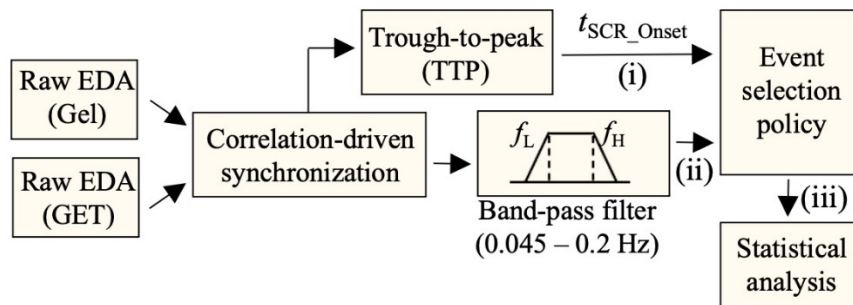


Figure 5.13: SCR detection algorithm for the correlation analysis.

For the SCR selection, we pick good EDA signals from gel measurement first, then compare them with the corresponding GET signals so that we don't bias the analysis by choosing better GET signals than the gel signals. The details of the event selection policy are as shown below.

Input: Synchronized and band-pass filtered EDA readings from the gel and GET  $v(t) = [SCR_{gel}(t), SCR_{get}(t)]$ , and the SCR event locations extracted with TTP,  $t_{SCR\_onset}[j]$ .

Output: clean marked SCR events,  $SCRc\{t, j\}$

1. *for*  $j = 1$  to  $\tau$  *do*: // segmentation,  $\tau = \#$  of detected candidate events with TTP.
2.  $v_{segmented}[t, j] = v(t)$  where  $v(t) \geq t_{SCR\_onset}[j]$  and  $v(t) < t_{SCR\_onset}[j + 1]$ .
3.  $\Delta SCR[j] = \max v_{segmented}[t, j] - v_{segmented}[1, j]$  // amplitude of each candidate event.
4.  $\Delta SCR_{max} = 95^{th}$  percentile of  $\Delta SCR$  // maximum SCR amplitude detected.
5. *for*  $j = 1$  to  $\tau$  *do*: // process each candidate event.
6.  $flag[j] = 0$ ; // initiate the flag array, 0 means a clean event.
7. if the duration of  $v_{segmented}[t, j] < 2sec$ , then  $flag[j] = 1$ ; // too short for a clean event.
8. if  $\Delta SCR[j] < 0.1 \cdot \Delta SCR_{max}$ , then  $flag[j] = 1$ ; // not enough SCR amplitude.
9.  $v_{rise}[t, j] = v_{segmented}[1:i_{max}, j]$ , where  $i_{max}$  is the timestamp index for the maximum of SCR events.
10.  $v_{recovery}[t, j] = v_{segmented}[i_{max}:end, j]$ , where  $end$  is the last timestamp index for the SCR event.
11. if  $\min v_{recovery}[t, j] > 0.1 \cdot \Delta SCR[j] + v_{rise}[1, j]$ , then  $flag[j] = 1$ ; // response did not recover more than 90% of the initial level before the next SCR event.
12. if  $flag[j] == 0$ , then  $SCRc\{t, j\} = append(v_{rise}[t, j], v_{recovery}[1:i_{10p-down}, j])$  // mark the event as a clean event,

where trim down the part of the recovery that drops below 10% of the initial SCR location.

if  $flag[j] == 1$ , then  $SCRc\{t, j\} = \{\}$  // exclude the event from further analysis.

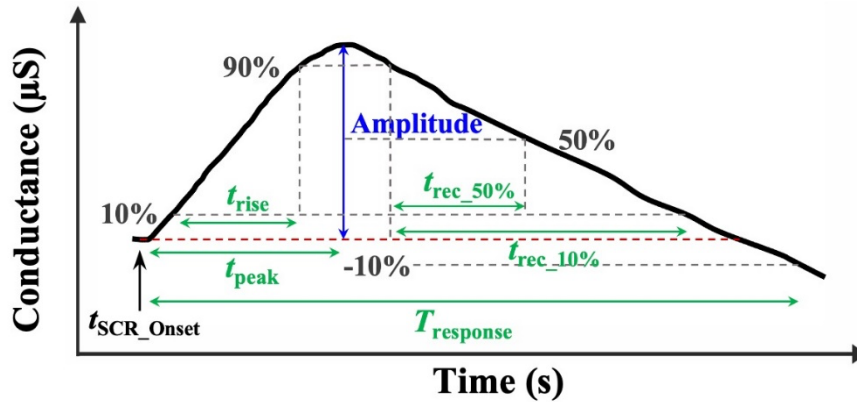


Figure 5.14: Parameters of an EDA signal used in the statistical analysis to validate the correlation between GET and gel.

For the correlation analysis, multiple parameters of the SCR are compared, including amplitude, peak time ( $t_{peak}$ ), response time ( $t_{response}$ ), rise time ( $t_{rise}$ ), and recovery time ( $t_{rec\_50\%}$  and  $t_{rec\_10\%}$ ), as defined in Figure 5.14. When the total number of candidate SCRs (i.e., the total number of events) are counted, as evident in Figure 5.15, the numbers of the two measurements are comparable for all five human subjects. Two datasets among the five (subjects #4 and #5) are discarded due to the insufficient number of SCR satisfying the event selection policy. The calculated parameter values for the three datasets are listed in Table A2-4. In general, the results indicate a strong correlation of SCRs between GET-measured and gel-measured signals as the  $p$ -values are all greater than 0.05. For all three datasets, the maximum number of SCRs ( $N$ ) are determined during the “controlled”

emotional session and discover that the N for the “controlled” session is very similar to the total number of applied stimulations (i.e., the number of affective pictures). Therefore, it is concluded that our GET-based EDA sensor is thoroughly validated by the gel-based gold standards for EDA measurements.

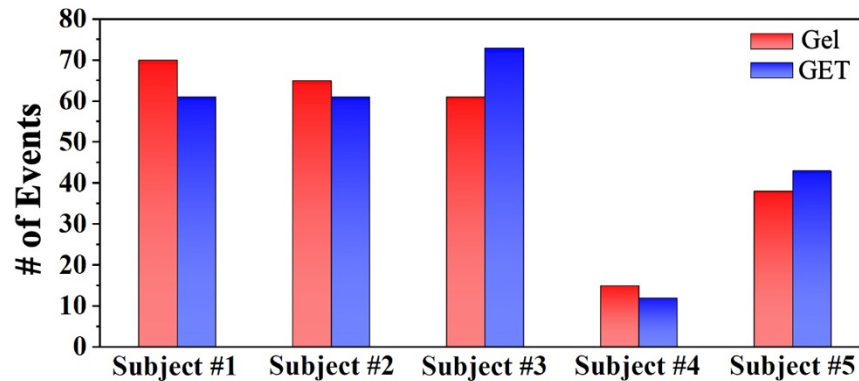


Figure 5.15: A total number of events measured by GET (blue) and gel electrodes (red) on five different subjects.

## 5.6 WEARABILITY OF GET-BASED EDA SENSOR

### 5.6.1 Impact by Motion Artifacts

A well-known disadvantage of dry electrodes is their susceptibility to motion artifacts. This is mainly because the contact between conventional rigid dry electrodes and skin is unsecured during motion. However, it has been validated that dry GET electrodes have comparable levels of motion artifacts to gel-based wet electrodes due to the perfect conformability on the skin. For EDA sensing on the palm, the GET sensors are subjected to constant motions due to hand movement. Therefore, it is critical to examine the EDA signal quality during motion. Figure 5.16 presents the EDA signals simultaneously

measured by GET and gel electrodes on the palm during various types of motions. In this study, the GET was covered by a  $\mu\text{m}$ -thin transparent protection layer (Nexcare liquid bandage spray, 3M). The amplitude of GET-measured conductance is found to be lower than that of the gel because the size of the exposed GET serpentine ( $0.6 \text{ cm}^2$ ) is 2.5 times smaller than the size of a circular gel electrode ( $1.5 \text{ cm}^2$ ). At first, three SCRs were produced without any motion by applying thermal stimulations (i.e., placing the other hand different from the EDA measurement on a hot plate of  $55 \text{ }^\circ\text{C}$  for 1 second) inspired by Posada-Quintero *et al* [301]. Next, different types of movements such as hand clenching, wrist bending, cellphone grabbing, and poking, were implemented three times each as indicated by dashed lines in Figure 5.16. Comparing the two SCR signals, it is validated that despite being dry electrodes, the GET has slightly smaller motion artifacts than the gel electrodes. This can be attributed to the perfect skin conformability as well as the absence of dangling wires. Also, the motion artifacts appear to be completely different shapes from the SCR signals, which means they can be easily identified and removed through either visual inspections or our event selection algorithms.

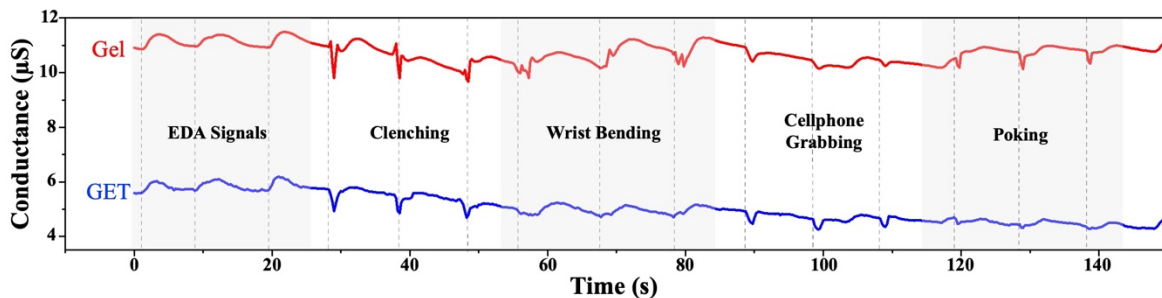


Figure 5.16: Comparison of the motion artifacts in GET- and gel-measured EDA signals when subjected to hand clenching, wrist bending, cell phone grabbing, and finger poking.

## 5.6.2 Short-Term Wearability

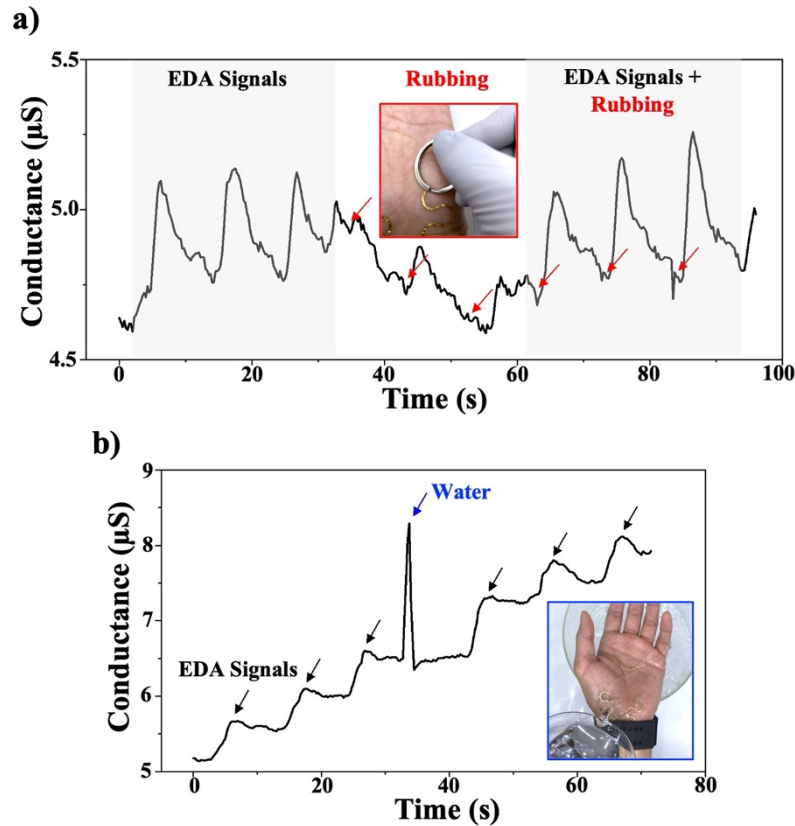


Figure 5.17: (a) Rubbing GET by a metal key ring only produces negligible artifacts compared with the EDA signal. (b) EDA quickly spikes and recovers when GET undergoes a quick exposure to water.

In addition to motions, our palms could touch various surfaces or liquids. Therefore, we also tested the performance of GET under representative incidents such as metal rubbing (Figure 5.17a) or water exposure (Figure 5.17b). In Figure 5.17a, firstly, three SCR signals were generated by applying thermal stimulation. Then, the GET was rubbed by a metal key ring three times. Lastly, three SCR signals were produced while the GET was

rubbed. It is evident that rubbing the GET produces a small dip of the conductance, but it has a negligible impact on the SCR signal. In addition, we confirm the survivability of the GET sensor under momentary exposure to water. In Figure 5.17b, three SCR signals were produced as benchmarks. While a spike in EDA was observed when water was poured on the GET, the conductance quickly recovered, and SCR signals can be detected again by the GET without any signal degradation.

### 5.6.3 Long-Term Wearability

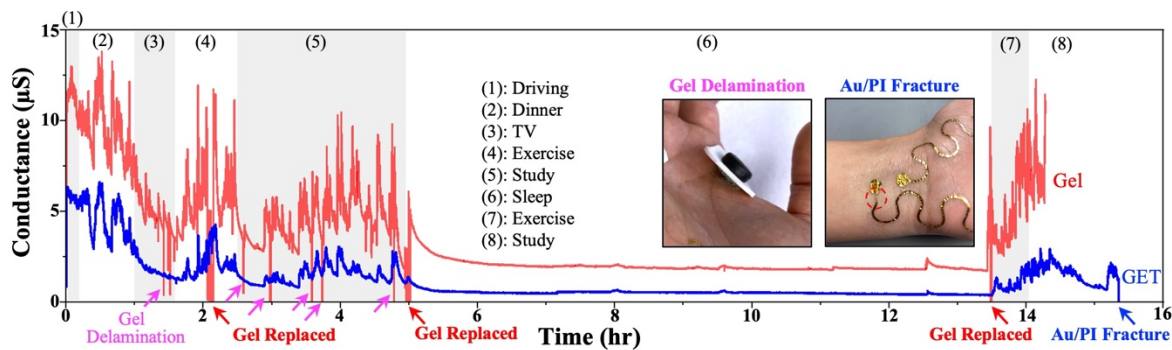


Figure 5.18: Long-term, ambulatory EDA sensing using GET (blue) and gel electrodes (red) during driving, dinner, watching TV, exercise, study, sleep, exercise, and study. Gel electrodes were frequently delaminated and had to be replaced three times. Insets show the photographs of gel electrode delamination and Au/PI rupture beneath the soft interlayer.

Ultimately, it is demonstrated that GET on the palm connected to an E4 wristband through HSPR and a soft interlayer can be successfully applied for long-term, ambulatory EDA sensing. Gel electrodes were used as a reference although it is uncomfortable, obstructive, and stigmatizing to wear for long-term. One subject reported social stigma concerns when wearing the gel electrodes during grocery shopping. Figure 5.18 shows

long-term, ambulatory EDA data taken from human subject #6. Note that the gel electrodes were replaced multiple times due to constant delamination (highlighted by red arrows). On the contrary, the GET finished three (see the other two in Figure A14) more than 15-hour long nonstop ambulatory EDA measurement sessions without needing any replacement. When EDA stopped recording, mechanical failures were not found in the GET but the Au/PI beneath the soft interlayer (Figure 5.18). Interestingly, the Au/PI rupture site is identical to the location of Au with the maximum strain from the shear of the soft interlayer. The long-term EDA data indicates that EDA is mostly inactive during sleep for subject #6 as depicted in Figure 5.18. However, for subject #3 (Figure A14a), the so-called EDA storm [302] was observed by the GET sensor. The gel electrodes on subject #3 failed to detect the EDA storm due to the partial delamination which happened during sleep. Unlike Figure 5.18 and Figure A14a (Supporting Information), Figure A14b shows delamination of GET which produced noises (highlighted by blue arrows). This occurred when the GET was covered by a relatively thick overlay (47- $\mu\text{m}$ -thick Ecoflex). The thick Ecoflex can induce GET delamination from the skin. It emphasizes that the substrate-free design of the GET sensor is crucial to perform reliable long-term EDA monitoring on the palm with minimized noise.

## 5.7 SUMMARY

This work introduces the first mechanically robust interface between sub-micron-thin stretchable electrodes and mm-thick rigid circuit boards. Using graphene e-tattoos (GET) connecting to a rigid wristband as an example, heterogeneous serpentine ribbons (HSPR) and soft interlayer are applied to significantly reduce the strains in graphene and Au nanomembrane. The soft interlayer serves dual purposes of both a vertical via and a mechanical buffer layer between the Au/PI and a commercially available rigid E4

wristband for EDA sensing. Combining HSPR and the soft interlayer, a wireless, unobstructive palm EDA sensor is constructed. Through a simplified circuit model, it is confirmed that the EDA is only measured through the GET although there are many intermediate components linking the GET to the E4 electrodes. Through correlation analysis, it is confirmed that the GET-based EDA sensor has a similar event detection capability as the gel electrodes. Moreover, GET has slightly smaller motion artifacts than the wet gel electrodes. Because of the combined mechanical robustness and high signal quality of the GET EDA sensors, up to 15 hours of continuous ambulatory EDA signals were successfully obtained.

## Chapter 6: Conclusions and Outlook

Graphene electronic tattoos (GET) has been successfully demonstrated as a next-generation wearable to monitor biosignals imperceptibly with a comparable performance to a bulky gel-based gold standard. GET is designed as filamentary serpentine and fabricated by a cost- and time-effective “wet transfer, dry patterning” method. Several concluding remarks of this dissertation are shown below.

1. The failure mechanisms of GET are revealed first and found that there exist four distinct failure stages due to the micro-cracking of graphene and macro-cracking of the supporting polymer.
2. The interface of its electrical contacts is vulnerable to the mechanical deformation due to the mechanical stiffness mismatch. This provides the fundamental insights to design future graphene-based soft electronics.
3. A novel interface design, so-called heterogeneous serpentine ribbons (HSPR), is introduced to improve this vulnerable interface of its electrical contacts. Throughout FEM analysis, 50 folds of strain reduction in GET using HSPR vs. a non-engineered interface (i.e., heterogeneous straight ribbons (HSTR)) have been confirmed. Furthermore, a significantly larger stretchability is obtained for the case of HSPR according to the experiments. This method offers a generic solution for the long-standing interconnect challenges between ultrathin sensors and rigid electronics.
4. An unobstructive GET-based EDA sensor is manufactured based on the HSPR and a soft interlayer and demonstrated more than 15 hours of continuous ambulatory monitoring of EDA.

However, the following limitations of this research should be reminded. First, the current FEM does not account for the buckling of HSPR. Second, the prediction of HSPR stretchability does not work when the stiffness mismatch is beyond 100. Therefore, there is more room to explore in-depth regarding the establishment of FEM analysis for more complex conditions. Third, it turns out that the ultrathin Au/PI is more prone to fracture under the soft interlayer than the GET connected through the HSPR, which needs to be engineered to further extend the wearability of the whole system in ambulatory settings.

As one of the exciting future research directions, a more in-depth theoretical analysis of the electro-mechanical behavior of GET would be a very interesting topic. So far, the electro-mechanical behaviors of GET are understood based on the experiments. However, more theoretical investigations will help to reveal governing physics of the fracture mechanism, such as when and how graphene crack is started and why multiple cracks are generated and propagated instead of a single channel crack.

Moreover, an interconnection design for packaging various soft electronics has many interesting challenges to be solved further. For example, current HSPR has a relatively low strain reduction in transverse stretching compared to longitudinal stretching. To overcome this issue, a similar interfacing method to HSPR but utilizing fractal serpentine structure instead of just serpentine structure can be implemented and studied further.

Furthermore, more electro-chemical understanding of the unique GET-to-skin interface is required so that we can fully understand how this interface can be implemented in different applications beyond measuring EDA. I strongly believe that my dissertation work can help to solve the above-mentioned challenges and demonstrate the potential of the GET-based wearable sensor and ultimately provide insights for the future-generation wearables.

## **Appendices**

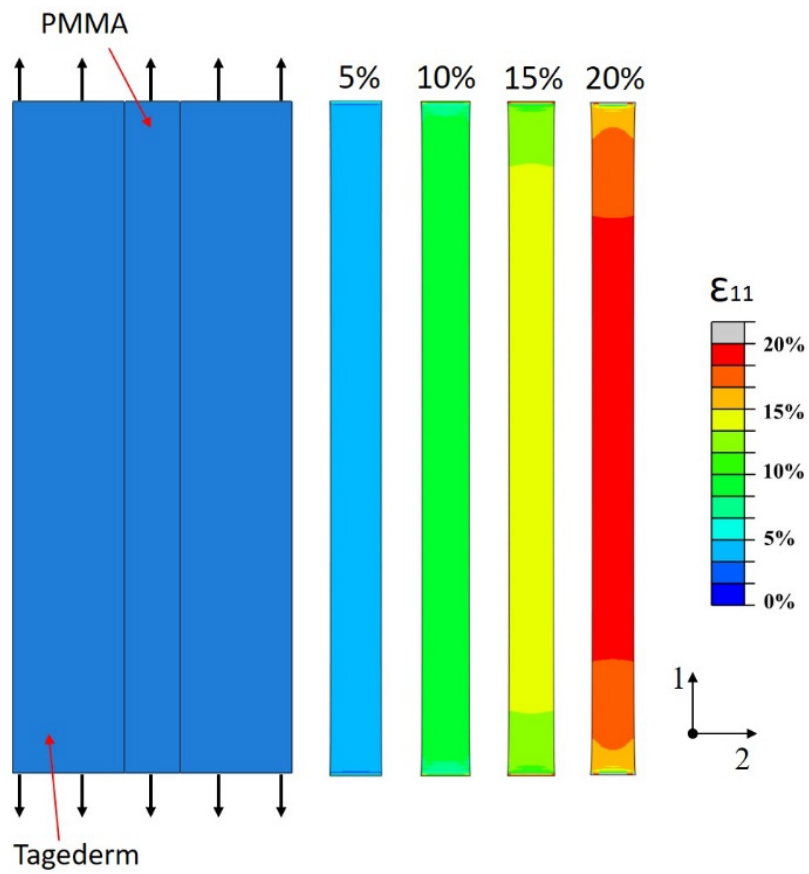


Figure A1: Finite element analysis results of the normal strain in the stretching direction ( $\epsilon_{11}$ ) in the Gr/PMMA ribbon. Note that most of the Gr/PMMA ribbon experiences  $\epsilon_{11}$  similar to the applied strain.

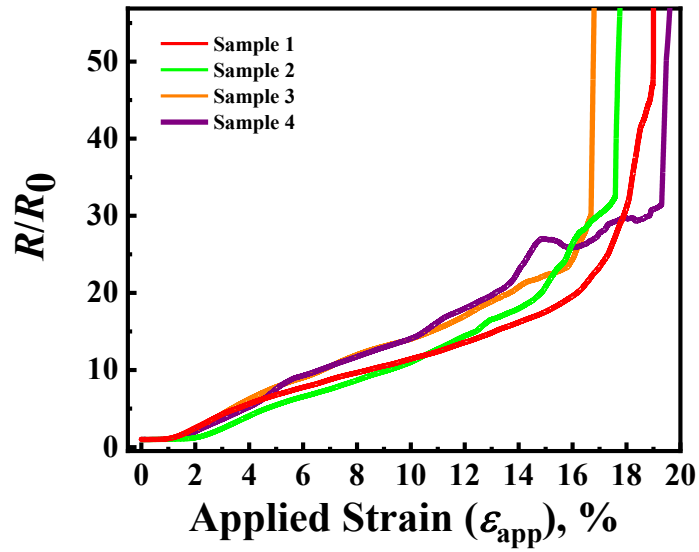


Figure A2: Repeatable electromechanical behavior of four Gr/PMMA ribbons on 3M Tegaderm tapes under tension.

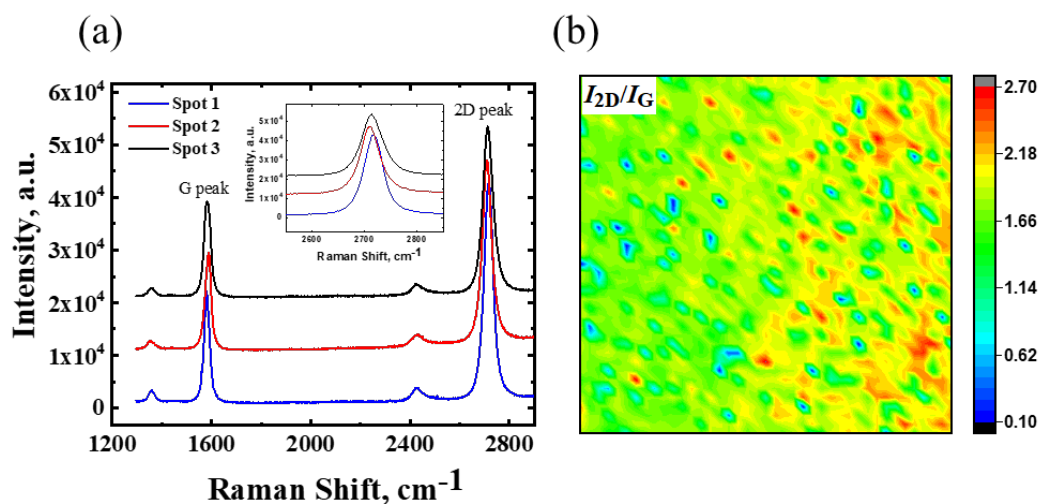


Figure A3: Characterization of commercial CVD-grown graphene under Raman spectroscopy. (a) Three random spots were chosen, and the characteristic peaks of the graphene (2D peak and G peak) were measured. The inset figure shows a zoomed-in view of the 2D peaks. (b) Raman mapping was performed within an area of  $80 \mu\text{m} \times 80 \mu\text{m}$  of the CVD graphene to construct a contour plot of the ratio of 2D peak intensity over G peak intensity ( $I_{2D}/I_G$ ).

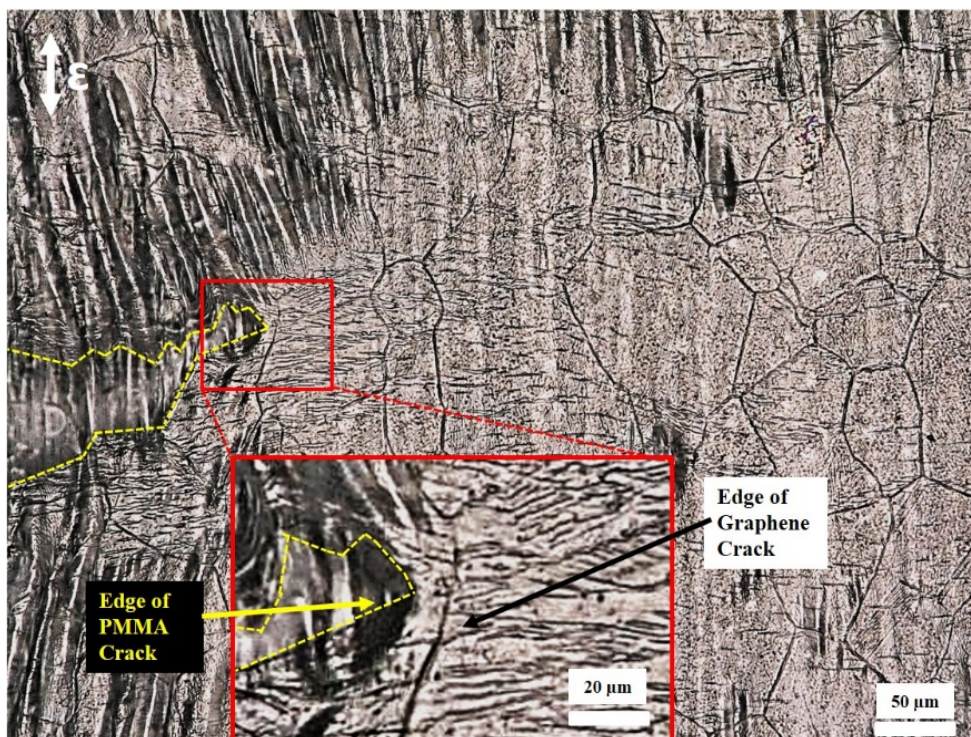


Figure A4: A micrograph of Gr/PMMA on a 3M Tegaderm tape at 16% of applied strain. Macro-cracks of PMMA were generated from the edge and graphene near the PMMA crack tip contained many micro-cracks due to crack tip strain concentration. In contrast, graphene far from the macro-crack of PMMA has fewer and smaller micro-cracks.

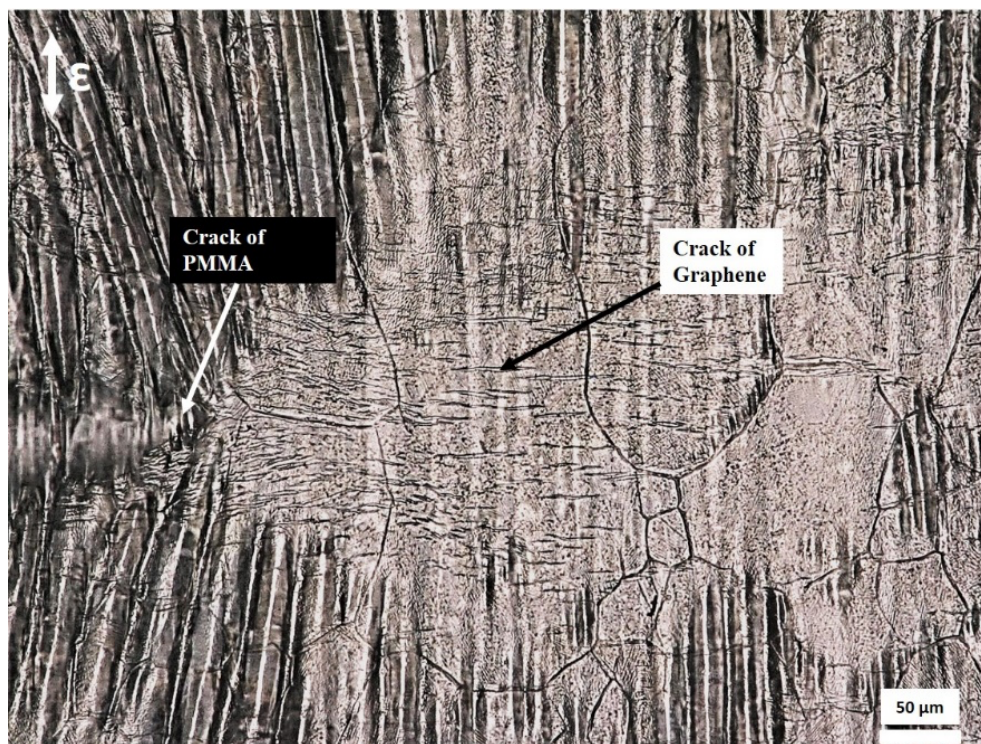


Figure A5: Additional micrograph of Gr/PMMA on a 3M Tegaderm tape at 16% of applied strain.

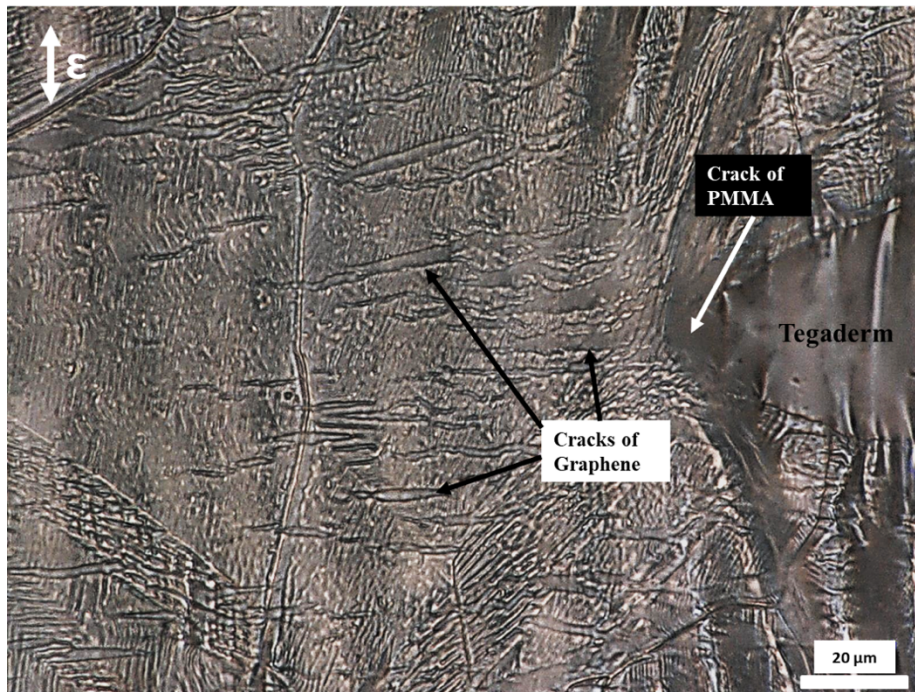


Figure A6: Additional micrograph of Gr/PMMA on a 3M Tegaderm tape at 16% of applied strain.



Figure A7: A global view of a Gr/PMMA ribbon on a 3M Tegaderm tape at fracture (18% of applied strain). Many macro-cracks transverse to the stretching direction is visible.

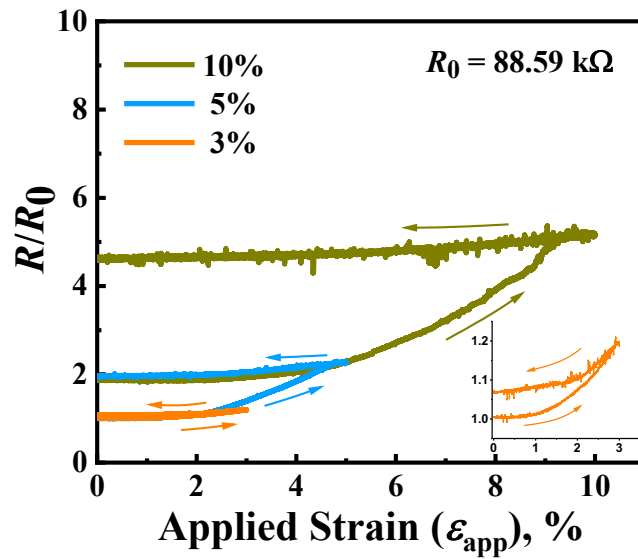


Figure A8: Loading and unloading tests on a Gr/PMMA ribbon supported by a 3M Tegaderm tape at different applied strains. The inset displays the zoomed-in view for the case when loading up to 3% and unloading.

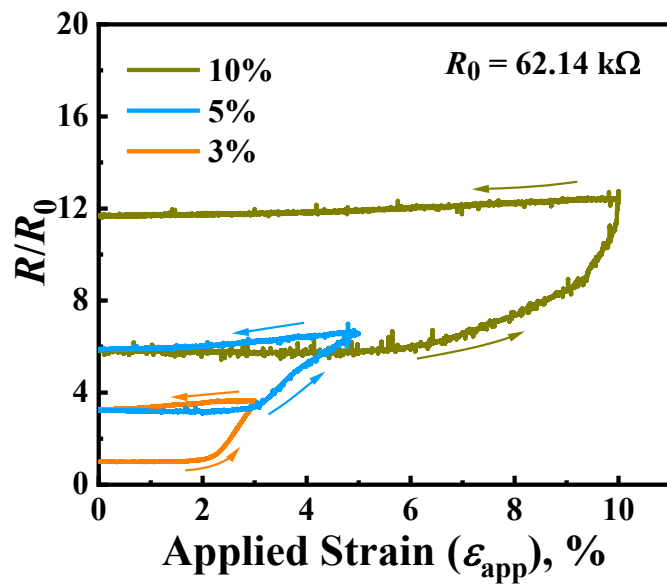


Figure A9: Loading and unloading tests on the bridged Gr/PMMA supported by a 3M Tegaderm tape at different applied strains.

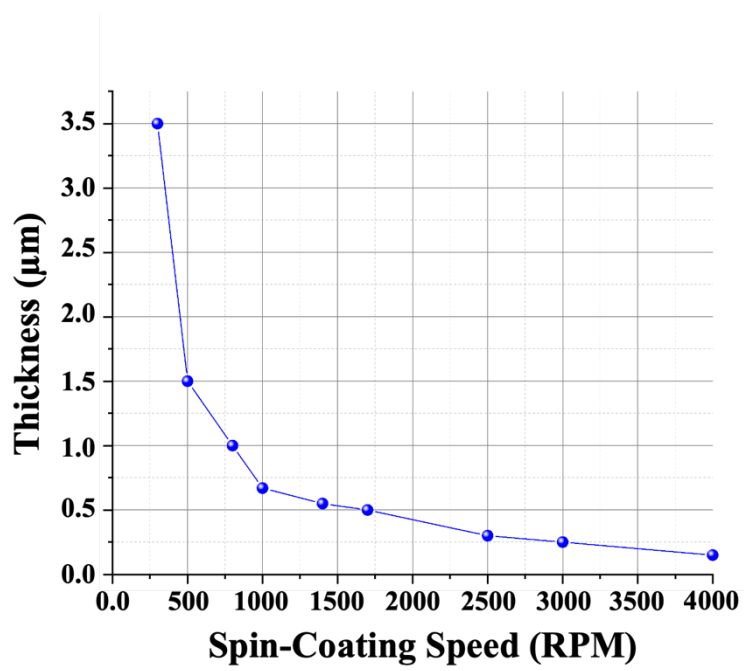


Figure A10: The thickness of diluted PI depending on spin-coating speed.

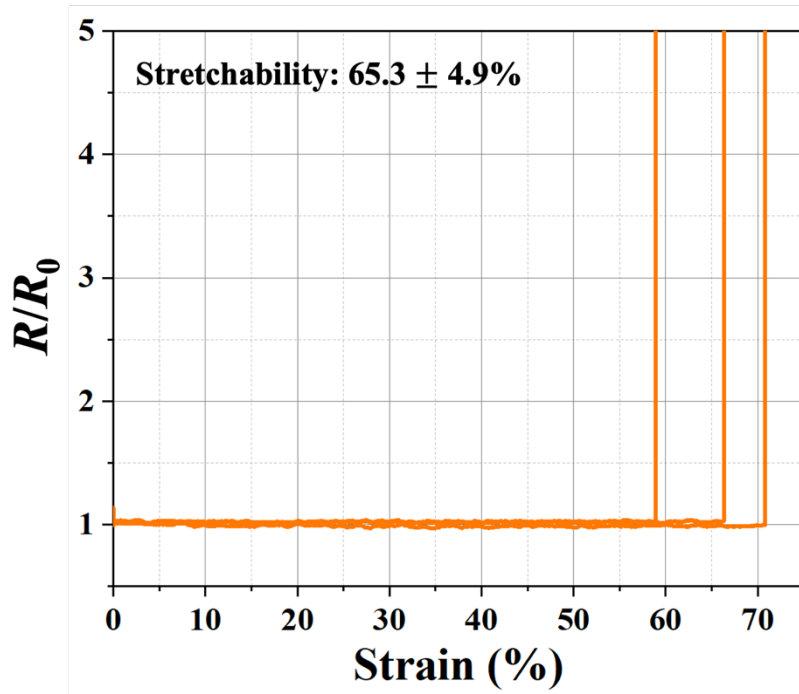


Figure A11: Stretchability of 750-nm-thin Au/PI. Each orange line indicates a different experimental trial.

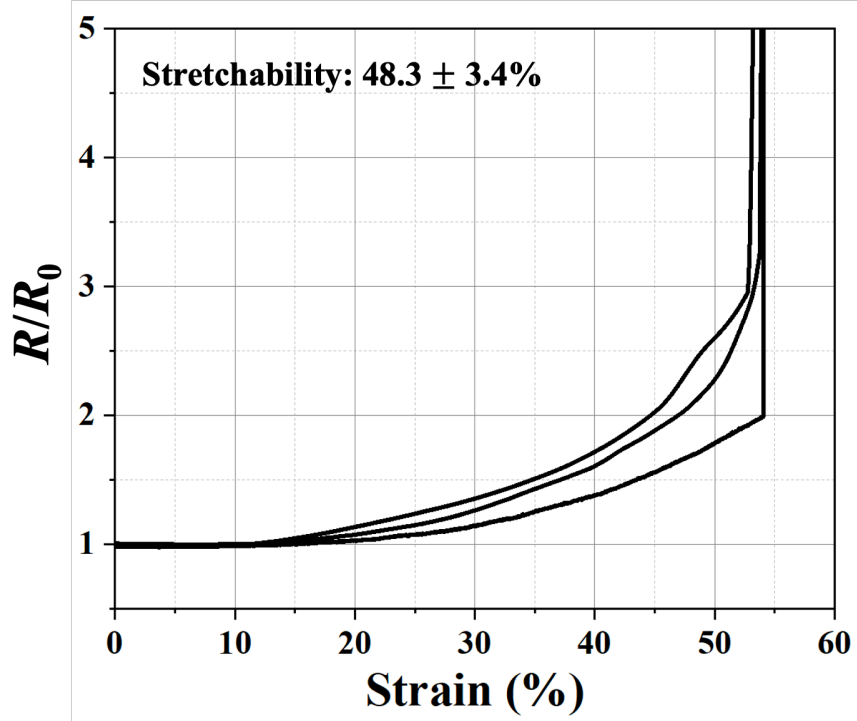


Figure A12: The stretchability of 300-nm-thin serpentine GET. Each black line indicates a different experimental trial.

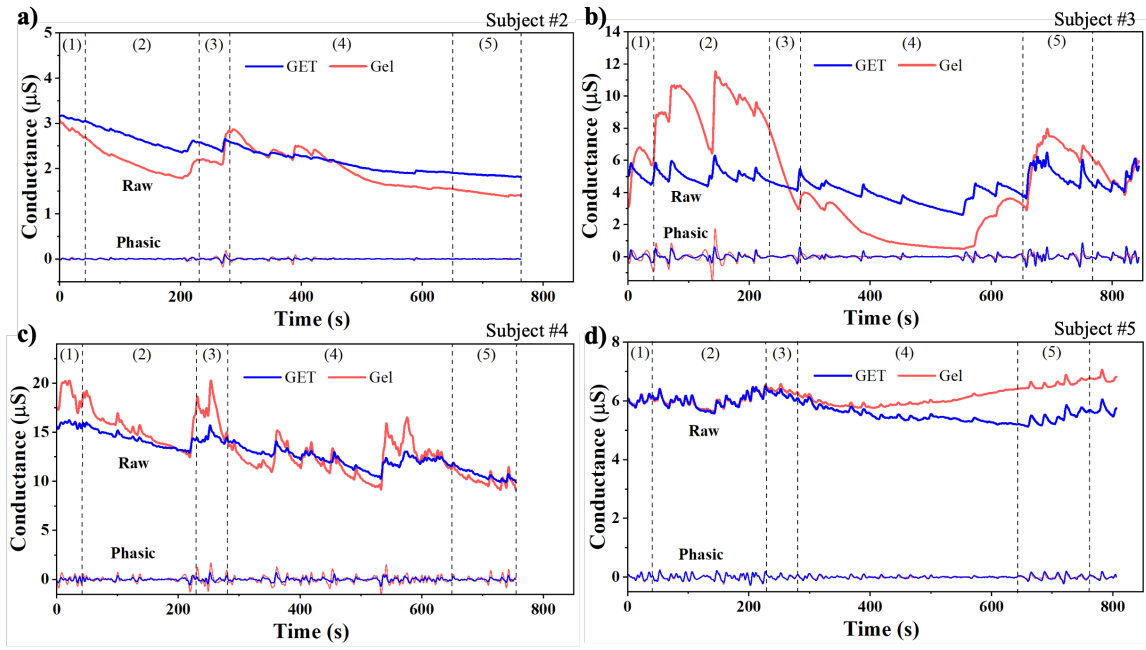


Figure A13: EDA measurement. a-d) EDA data from different human subjects (#2 - #5, respectively).

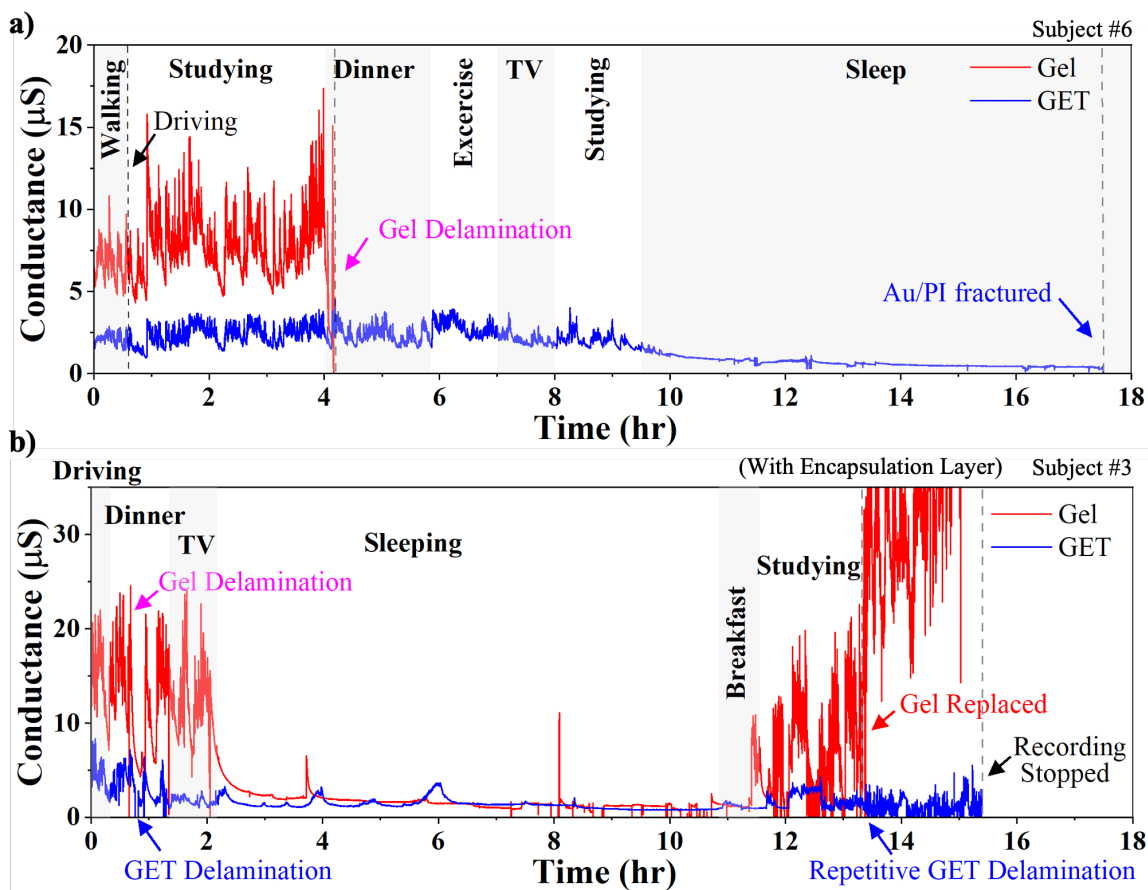


Figure A14: EDA long-term monitoring data. a) Long-term wearability test on subject #6. Ag/AgCl gel electrodes were not replaced after delamination. b) Another long-term wearability tests. This time, GET was encapsulated by a 47- $\mu\text{m}$ -thick overlay (Tegaderm, 3M).

No.	EM Code	Mean	SD
1	506	0	0.43
2	736	1.75	0.46
3	453	1.15	0.59
4	710	1.86	0.35
5	728	1.8	0.4
6	411	0.83	0.56
7	597	1.65	0.51
8	158	0.02	0.41
9	361	0.94	0.55
10	56	0.01	0.46
11	618	1.84	0.37

Table A1: Index of the affective pictures used from the EmoMadrid database. Mean values are scaled from 0 (neutral) to 2 (maximum arousal) by EmoMadrid. Images from No. 1 – 10 are used for session (4) and No. 11 is used for session (5).

Session		Mean (Gel)	Mean (GET)	Mean Error (ME)	95% CI of ME	<i>p</i> -value	N
(2)	<b>Amplitude</b> [ $\mu$ S]	0.305	0.214	0.092	0.101	0.149	5
	$t_{\text{peak}}/T_{\text{response}}$	0.52	0.547	-0.027	0.024	0.098	5
	$t_{\text{rise}}$ [ms]	1016	916	100	160	0.288	5
	$t_{\text{rec, 50\%}}$	644	620	24	101	0.666	5
	$t_{\text{rec, 10\%}}$	1242	1034	208	373	0.336	5
(4)	<b>Amplitude</b> [ $\mu$ S]	0.174	0.154	0.019	0.022	0.108	13
	$t_{\text{peak}}/T_{\text{response}}$	0.6	0.59	0.01	0.032	0.572	13
	$t_{\text{rise}}$ [ms]	859	996	-137	204	0.212	13
	$t_{\text{rec, 50\%}}$	370	412	-42.3	38.9	0.055	13
	$t_{\text{rec, 10\%}}$	710	792	-81.5	91.8	0.108	13
(5)	<b>Amplitude</b> [ $\mu$ S]	0.321	0.229	0.092	0.066	0.033	7
	$t_{\text{peak}}/T_{\text{response}}$	0.527	0.568	-0.041	0.028	0.028	7
	$t_{\text{rise}}$ [ms]	763	798	-35.7	59.8	0.287	7
	$t_{\text{rec, 50\%}}$	393	472	-78.6	125	0.265	7
	$t_{\text{rec, 10\%}}$	884	801	82.8	88.0	0.115	7

Table A2: EDA correlation score for human subject #1.

Session		Mean (Gel)	Mean (GET)	Mean Error (ME)	95% CI of ME	<i>p</i> -value	N
(2)	<b>Amplitude</b> [ $\mu$ S]	0.697	0.410	0.287	0.115	0.04	3
	$t_{\text{peak}}/T_{\text{response}}$	0.458	0.568	-0.111	0.13	0.238	3
	$t_{\text{rise}}$ [ms]	796.7	853.3	-56.7	219.8	0.664	3
	$t_{\text{rec, 50\%}}$	390	656.7	-266.7	455.79	0.370	3
	$t_{\text{rec, 10\%}}$	786.7	803.3	-16.7	313.26	0.926	3
(4)	<b>Amplitude</b> [ $\mu$ S]	0.572	0.248	0.324	0.169	<0.005	12
	$t_{\text{peak}}/T_{\text{response}}$	0.523	0.494	0.030	0.046	0.231	12
	$t_{\text{rise}}$ [ms]	697.5	661.7	35.8	68.4	0.327	12
	$t_{\text{rec, 50\%}}$	445	544.2	-99.2	184.5	0.315	12
	$t_{\text{rec, 10\%}}$	779.2	970	-190.8	263.9	0.184	12
(5)	<b>Amplitude</b> [ $\mu$ S]	0.762	0.227	0.535	0.442	0.254	2
	$t_{\text{peak}}/T_{\text{response}}$	0.385	0.438	-0.052	0.238	0.742	2
	$t_{\text{rise}}$ [ms]	840	725	115	29.4	0.083	2
	$t_{\text{rec, 50\%}}$	530	480	50	254.8	0.766	2
	$t_{\text{rec, 10\%}}$	1650	855	795	676.2	0.261	2

Table A3: EDA correlation score for human subject #2.

Session		Mean (Gel)	Mean (GET)	Mean Error (ME)	95% CI of ME	<i>p</i> -value	N
(2)	<b>Amplitude</b> [ $\mu$ S]	0.115	0.105	0.01	0.028	0.49	8
	$t_{\text{peak}}/T_{\text{response}}$	0.572	0.574	-0.002	0.022	0.869	8
	$t_{\text{rise}}$ [ms]	652.5	668.75	-16.25	89.28	0.732	8
	$t_{\text{rec, 50\%}}$	312.5	312.5	0	34.94	1	8
	$t_{\text{rec, 10\%}}$	630	607.5	22.5	41.21	0.32	8
(4)	<b>Amplitude</b> [ $\mu$ S]	0.074	0.114	-0.039	0.014	<0.005	10
	$t_{\text{peak}}/T_{\text{response}}$	0.479	0.465	0.015	0.045	0.533	10
	$t_{\text{rise}}$ [ms]	1013	1015	-2	178.1	0.983	10
	$t_{\text{rec, 50\%}}$	532	840	-308	208.8	0.018	10
	$t_{\text{rec, 10\%}}$	1209	1721	-512	352.8	0.019	10
(5)	<b>Amplitude</b> [ $\mu$ S]	0.097	0.231	-0.134	0.026	0.01	3
	$t_{\text{peak}}/T_{\text{response}}$	0.536	0.525	0.011	0.059	0.749	3
	$t_{\text{rise}}$ [ms]	910	1583.3	-673.3	1056.4	0.338	3
	$t_{\text{rec, 50\%}}$	466.7	980	-513.3	351.04	0.103	3
	$t_{\text{rec, 10\%}}$	960	1766.7	-806.7	492.3	0.085	3

Table A4: EDA correlation score for human subject #3.

## References

- [1] Bao Z and Chen X 2016 Flexible and Stretchable Devices *Adv. Mater.* 28 4177–9
- [2] Choi S, Lee H, Ghaffari R, Hyeon T and Kim D-H 2015 Recent Advances in Flexible and Stretchable Bio-Electronic Devices Integrated with Nanomaterials *Adv. Mater.* 28 4203–18
- [3] Stoppa M and Chiolerio A 2014 Wearable Electronics and Smart Textiles: A Critical Review *Sensors* 14 11957–92
- [4] Ameri S K, Kim M, Kuang I A, Perera W K, Alshiekh M, Jeong H, Topcu U, Akinwande D and Lu N 2018 Imperceptible electrooculography graphene sensor system for human–robot interface *Npj 2D Mater. Appl.* 2
- [5] Guo Y, Zhong M, Fang Z, Wan P and Yu G 2019 A Wearable Transient Pressure Sensor Made with MXene Nanosheets for Sensitive Broad-Range Human–Machine Interfacing *Nano Lett.* 19 1143–50
- [6] Roh E, Hwang B-U, Kim D, Kim B-Y and Lee N-E 2015 Stretchable, Transparent, Ultrasensitive, and Patchable Strain Sensor for Human–Machine Interfaces Comprising a Nanohybrid of Carbon Nanotubes and Conductive Elastomers *ACS Nano* 9 6252–61
- [7] Lim S, Son D, Kim J, Lee Y B, Song J-K, Choi S, Lee D J, Kim J H, Lee M, Hyeon T and Kim D-H 2015 Transparent and Stretchable Interactive Human Machine Interface Based on Patterned Graphene Heterostructures *Adv. Funct. Mater.* 25 375–83
- [8] Jung S, Kim J H, Kim J, Choi S, Lee J, Park I, Hyeon T and Kim D-H 2014 Reverse-Micelle-Induced Porous Pressure-Sensitive Rubber for Wearable Human–Machine Interfaces *Adv. Mater.* 26 4825–30
- [9] Polat E O, Mercier G, Nikitskiy I, Puma E, Galan T, Gupta S, Montagut M, Piqueras J J, Bouwens M, Durduran T, Konstantatos G, Goossens S and Koppens F 2019 Flexible graphene photodetectors for wearable fitness monitoring *Sci. Adv.* 5 eaaw7846
- [10] Yao S, Swetha P and Zhu Y 2018 Nanomaterial-Enabled Wearable Sensors for Healthcare *Adv. Healthc. Mater.* 7 1700889
- [11] Liu Y, Pharr M and Salvatore G A 2017 Lab-on-Skin: A Review of Flexible and Stretchable Electronics for Wearable Health Monitoring *ACS Nano* 11 9614–35

- [12] Yao S, Ren P, Song R, Liu Y, Huang Q, Dong J, O'Connor B T and Zhu Y 2020 Nanomaterial-Enabled Flexible and Stretchable Sensing Systems: Processing, Integration, and Applications *Adv. Mater.* 32 1902343
- [13] Wang L, Chen S, Shu T and Hu X 2020 Functional Inks for Printable Energy Storage Applications based on 2 D Materials *ChemSusChem* 13 1330–53
- [14] Huang L, Su J, Song Y and Ye R 2020 Laser-Induced Graphene: En Route to Smart Sensing *Nano-Micro Lett.* 12 157
- [15] Wang C, Xia K, Wang H, Liang X, Yin Z and Zhang Y 2019 Advanced Carbon for Flexible and Wearable Electronics *Adv. Mater.* 31 1801072
- [16] Kim K, Park Y, Hyun B G, Choi M and Park J 2019 Recent Advances in Transparent Electronics with Stretchable Forms *Adv. Mater.* 31 1804690
- [17] Li L, Lou Z, Chen D, Jiang K, Han W and Shen G 2018 Recent Advances in Flexible/Stretchable Supercapacitors for Wearable Electronics *Small* 14 1702829
- [18] Papageorgiou D G, Kinloch I A and Young R J 2017 Mechanical properties of graphene and graphene-based nanocomposites *Prog. Mater. Sci.* 90 75–127
- [19] Zhang H 2015 Ultrathin Two-Dimensional Nanomaterials *ACS Nano* 9 9451–69
- [20] Lin J, Zhu Z, Cheung C F, Yan F and Li G 2020 Digital manufacturing of functional materials for wearable electronics *J. Mater. Chem. C* 8 10587–603
- [21] Pang Y, Yang Z, Yang Y and Ren T 2020 Wearable Electronics Based on 2D Materials for Human Physiological Information Detection *Small* 16 1901124
- [22] Das T, Sharma B K, Katiyar A K and Ahn J-H 2018 Graphene-based flexible and wearable electronics *J. Semicond.* 39 011007
- [23] Akinwande D, Brennan C J, Bunch J S, Egberts P, Felts J R, Gao H, Huang R, Kim J-S, Li T, Li Y, Liechti K M, Lu N, Park H S, Reed E J, Wang P, Yakobson B I, Zhang T, Zhang Y-W, Zhou Y and Zhu Y 2017 A review on mechanics and mechanical properties of 2D materials—Graphene and beyond *Extreme Mech. Lett.* 13 42–77
- [24] Kang P, Wang M C and Nam S 2016 Bioelectronics with two-dimensional materials *Microelectron. Eng.* 161 18–35
- [25] Amjadi M, Kyung K-U, Park I and Sitti M 2016 Stretchable, Skin-Mountable, and Wearable Strain Sensors and Their Potential Applications: A Review *Adv. Funct. Mater.* 26 1678–98

- [26] Yeo J C, Yap H K, Xi W, Wang Z, Yeow C-H and Lim C T 2016 Flexible and Stretchable Strain Sensing Actuator for Wearable Soft Robotic Applications *Adv. Mater. Technol.* 1 1600018
- [27] Agarwal G, Besuchet N, Audergon B and Paik J 2016 Stretchable Materials for Robust Soft Actuators towards Assistive Wearable Devices *Sci. Rep.* 6
- [28] Rus D and Tolley M T 2015 Design, fabrication and control of soft robots *Nature* 521 467–75
- [29] Bollella P, Fusco G, Tortolini C, Sanzò G, Favero G, Gorton L and Antiochia R 2017 Beyond graphene: Electrochemical sensors and biosensors for biomarkers detection *Biosens. Bioelectron.* 89 152–66
- [30] Wessendorf A M and Newman D J 2012 Dynamic Understanding of Human-Skin Movement and Strain-Field Analysis *IEEE Trans. Biomed. Eng.* 59 3432–8
- [31] Maiti R, Gerhardt L-C, Lee Z S, Byers R A, Woods D, Sanz-Herrera J A, Franklin S E, Lewis R, Matcher S J and Carré M J 2016 In vivo measurement of skin surface strain and sub-surface layer deformation induced by natural tissue stretching *J. Mech. Behav. Biomed. Mater.* 62 556–69
- [32] Kabiri Ameri S, Ho R, Jang H, Tao L, Wang Y, Wang L, Schnyer D M, Akinwande D and Lu N 2017 Graphene Electronic Tattoo Sensors *ACS Nano* 11 7634–41
- [33] Miyamoto A, Lee S, Cooray N F, Lee S, Mori M, Matsuhisa N, Jin H, Yoda L, Yokota T, Itoh A, Sekino M, Kawasaki H, Ebihara T, Amagai M and Someya T 2017 Inflammation-free, gas-permeable, lightweight, stretchable on-skin electronics with nanomeshes *Nat. Nanotechnol.* 12 907–13
- [34] Son D, Lee J, Qiao S, Ghaffari R, Kim J, Lee J E, Song C, Kim S J, Lee D J, Jun S W, Yang S, Park M, Shin J, Do K, Lee M, Kang K, Hwang C S, Lu N, Hyeon T and Kim D-H 2014 Multifunctional wearable devices for diagnosis and therapy of movement disorders *Nat. Nanotechnol.* 9 397–404
- [35] Yang S, Chen Y-C, Nicolini L, Pasupathy P, Sacks J, Su B, Yang R, Sanchez D, Chang Y-F, Wang P, Schnyer D, Neikirk D and Lu N 2015 “Cut-and-Paste” Manufacture of Multiparametric Epidermal Sensor Systems *Adv. Mater.* 27 6423–30
- [36] Nur R, Matsuhisa N, Jiang Z, Nayeem M O G, Yokota T and Someya T 2018 A Highly Sensitive Capacitive-type Strain Sensor Using Wrinkled Ultrathin Gold Films *Nano Lett.* 18 5610–7

- [37] Tai Y, Mülle M, Aguilar Ventura I and Lubineau G 2015 A highly sensitive, low-cost, wearable pressure sensor based on conductive hydrogel spheres *Nanoscale* 7 14766–73
- [38] Cai G, Wang J, Qian K, Chen J, Li S and Lee P S 2017 Extremely Stretchable Strain Sensors Based on Conductive Self-Healing Dynamic Cross-Links Hydrogels for Human-Motion Detection *Adv. Sci.* 4 1600190
- [39] Lei Z, Wang Q, Sun S, Zhu W and Wu P 2017 A Bioinspired Mineral Hydrogel as a Self-Healable, Mechanically Adaptable Ionic Skin for Highly Sensitive Pressure Sensing *Adv. Mater.* 29 1700321
- [40] Liao M, Wan P, Wen J, Gong M, Wu X, Wang Y, Shi R and Zhang L 2017 Wearable, Healable, and Adhesive Epidermal Sensors Assembled from Mussel-Inspired Conductive Hybrid Hydrogel Framework *Adv. Funct. Mater.* 27 1703852
- [41] Liu S, Zheng R, Chen S, Wu Y, Liu H, Wang P, Deng Z and Liu L 2018 A compliant, self-adhesive and self-healing wearable hydrogel as epidermal strain sensor *J. Mater. Chem. C* 6 4183–90
- [42] Yin M, Zhang Y, Yin Z, Zheng Q and Zhang A P 2018 Micropatterned Elastic Gold-Nanowire/Polyacrylamide Composite Hydrogels for Wearable Pressure Sensors *Adv. Mater. Technol.* 3
- [43] Park Y-L, Majidi C, Kramer R, Bérard P and Wood R J 2010 Hyperelastic pressure sensing with a liquid-embedded elastomer *J. Micromechanics Microengineering* 20 125029
- [44] Tabatabai A, Fassler A, Usiak C and Majidi C 2013 Liquid-Phase Gallium–Indium Alloy Electronics with Microcontact Printing *Langmuir* 29 6194–200
- [45] Fassler A and Majidi C 2013 3D structures of liquid-phase GaIn alloy embedded in PDMS with freeze casting *Lab. Chip* 13 4442–50
- [46] Choi D Y, Kim M H, Oh Y S, Jung S-H, Jung J H, Sung H J, Lee H W and Lee H M 2017 Highly Stretchable, Hysteresis-Free Ionic Liquid-Based Strain Sensor for Precise Human Motion Monitoring *ACS Appl. Mater. Interfaces* 9 1770–80
- [47] Dickey M D 2017 Stretchable and Soft Electronics using Liquid Metals *Adv. Mater.* 29
- [48] Pan C, Kumar K, Li J, Markvicka E J, Herman P R and Majidi C 2018 Visually Imperceptible Liquid-Metal Circuits for Transparent, Stretchable Electronics with Direct Laser Writing *Adv. Mater.* 30 1706937

- [49] Kim S, Lee J and Choi B 2015 Stretching and Twisting Sensing With Liquid-Metal Strain Gauges Printed on Silicone Elastomers *IEEE Sens. J.* 15 6077–8
- [50] Qian Y, Zhang X, Xie L, Qi D, Chandran B K, Chen X and Huang W 2016 Stretchable Organic Semiconductor Devices *Adv. Mater.* 28 9243–65
- [51] Sim K, Rao Z, Ershad F and Yu C 2020 Rubbery Electronics Fully Made of Stretchable Elastomeric Electronic Materials *Adv. Mater.* 32 1902417
- [52] Wang S, Xu J, Wang W, Wang G-J N, Rastak R, Molina-Lopez F, Chung J W, Niu S, Feig V R, Lopez J, Lei T, Kwon S-K, Kim Y, Foudeh A M, Ehrlich A, Gasperini A, Yun Y, Murmann B, Tok J B-H and Bao Z 2018 Skin electronics from scalable fabrication of an intrinsically stretchable transistor array *Nature* 555 83–8
- [53] Wang Y, Zhu C, Pfattner R, Yan H, Jin L, Chen S, Molina-Lopez F, Lissel F, Liu J, Rabiah N I, Chen Z, Chung J W, Linder C, Toney M F, Murmann B and Bao Z 2017 A highly stretchable, transparent, and conductive polymer *Sci. Adv.* 3 e1602076
- [54] Fan X, Wang N, Yan F, Wang J, Song W and Ge Z 2018 A Transfer-Printed, Stretchable, and Reliable Strain Sensor Using PEDOT:PSS/Ag NW Hybrid Films Embedded into Elastomers *Adv. Mater. Technol.* 3 1800030
- [55] Ershad F, Thukral A, Yue J, Comeaux P, Lu Y, Shim H, Sim K, Kim N-I, Rao Z, Guevara R, Contreras L, Pan F, Zhang Y, Guan Y-S, Yang P, Wang X, Wang P, Wu X and Yu C 2020 Ultra-conformal drawn-on-skin electronics for multifunctional motion artifact-free sensing and point-of-care treatment *Nat. Commun.* 11 3823
- [56] Yao S and Zhu Y 2014 Wearable multifunctional sensors using printed stretchable conductors made of silver nanowires *Nanoscale* 6 2345–52
- [57] Hong S, Lee H, Lee J, Kwon J, Han S, Suh Y D, Cho H, Shin J, Yeo J and Ko S H 2015 Highly Stretchable and Transparent Metal Nanowire Heater for Wearable Electronics Applications *Adv. Mater.* 27 4744–51
- [58] Joo Y, Byun J, Seong N, Ha J, Kim H, Kim S, Kim T, Im H, Kim D and Hong Y 2015 Silver nanowire-embedded PDMS with a multiscale structure for a highly sensitive and robust flexible pressure sensor *Nanoscale* 7 6208–15
- [59] Lee S, Shin S, Lee S, Seo J, Lee J, Son S, Cho H J, Algadi H, Al-Sayari S, Kim D E and Lee T 2015 Ag Nanowire Reinforced Highly Stretchable Conductive Fibers for Wearable Electronics *Adv. Funct. Mater.* 25 3114–21

- [60] Darabi M A, Khosrozadeh A, Wang Q and Xing M 2015 Gum Sensor: A Stretchable, Wearable, and Foldable Sensor Based on Carbon Nanotube/Chewing Gum Membrane *ACS Appl. Mater. Interfaces* 7 26195–205
- [61] Liu Z, Qi D, Guo P, Liu Y, Zhu B, Yang H, Liu Y, Li B, Zhang C, Yu J, Liedberg B and Chen X 2015 Thickness-Gradient Films for High Gauge Factor Stretchable Strain Sensors *Adv. Mater.* 27 6230–7
- [62] Suzuki K, Yataka K, Okumiya Y, Sakakibara S, Sako K, Mimura H and Inoue Y 2016 Rapid-Response, Widely Stretchable Sensor of Aligned MWCNT/Elastomer Composites for Human Motion Detection *ACS Sens.* 1 817–25
- [63] He X, Zi Y, Guo H, Zheng H, Xi Y, Wu C, Wang J, Zhang W, Lu C and Wang Z L 2016 A Highly Stretchable Fiber-Based Triboelectric Nanogenerator for Self-Powered Wearable Electronics *Adv. Funct. Mater.* 27 1604378
- [64] Giffney T, Bejanin E, Kurian A S, Travas-Sejdic J and Aw K 2017 Highly stretchable printed strain sensors using multi-walled carbon nanotube/silicone rubber composites *Sens. Actuators Phys.* 259 44–9
- [65] Ho D H, Sun Q, Kim S Y, Han J T, Kim D H and Cho J H 2016 Stretchable and Multimodal All Graphene Electronic Skin *Adv. Mater.* 28 2601–8
- [66] Kang M, Kim J, Jang B, Chae Y, Kim J-H and Ahn J-H 2017 Graphene-Based Three-Dimensional Capacitive Touch Sensor for Wearable Electronics *ACS Nano* 11 7950–7
- [67] Bae S-H, Lee Y, Sharma B K, Lee H-J, Kim J-H and Ahn J-H 2013 Graphene-based transparent strain sensor *Carbon* 51 236–42
- [68] Chun S, Choi Y and Park W 2017 All-graphene strain sensor on soft substrate *Carbon* 116 753–9
- [69] Chun S, Kim Y, Oh H-S, Bae G and Park W 2015 A highly sensitive pressure sensor using a double-layered graphene structure for tactile sensing *Nanoscale* 7 11652–9
- [70] Khan U, Kim T-H, Ryu H, Seung W and Kim S-W 2017 Graphene Tribotronics for Electronic Skin and Touch Screen Applications *Adv. Mater.* 29 1603544
- [71] Choi M K, Park I, Kim D C, Joh E, Park O K, Kim J, Kim M, Choi C, Yang J, Cho K W, Hwang J-H, Nam J-M, Hyeon T, Kim J H and Kim D-H 2015 Thermally Controlled, Patterned Graphene Transfer Printing for Transparent and Wearable Electronic/Optoelectronic System *Adv. Funct. Mater.* 25 7109–18

- [72] Lee S-K, Kim B J, Jang H, Yoon S C, Lee C, Hong B H, Rogers J A, Cho J H and Ahn J-H 2011 Stretchable Graphene Transistors with Printed Dielectrics and Gate Electrodes *Nano Lett.* 11 4642–6
- [73] Lipani L, Dupont B G R, Doungmene F, Marken F, Tyrrell R M, Guy R H and Ilie A 2018 Non-invasive, transdermal, path-selective and specific glucose monitoring via a graphene-based platform *Nat. Nanotechnol.* 13 504–11
- [74] Kim K S, Zhao Y, Jang H, Lee S Y, Kim J M, Kim K S, Ahn J-H, Kim P, Choi J-Y and Hong B H 2009 Large-scale pattern growth of graphene films for stretchable transparent electrodes *Nature* 457 706–10
- [75] Choi D, Choi M-Y, Choi W M, Shin H-J, Park H-K, Seo J-S, Park J, Yoon S-M, Chae S J, Lee Y H, Kim S-W, Choi J-Y, Lee S Y and Kim J M 2010 Fully Rollable Transparent Nanogenerators Based on Graphene Electrodes *Adv. Mater.* 22 2187–92
- [76] Kwak Y H, Choi D S, Kim Y N, Kim H, Yoon D H, Ahn S-S, Yang J-W, Yang W S and Seo S 2012 Flexible glucose sensor using CVD-grown graphene-based field effect transistor *Biosens. Bioelectron.* 37 82–7
- [77] Sun Q, Seung W, Kim B J, Seo S, Kim S-W and Cho J H 2015 Active Matrix Electronic Skin Strain Sensor Based on Piezopotential-Powered Graphene Transistors *Adv. Mater.* 27 3411–7
- [78] Mannoor M S, Tao H, Clayton J D, Sengupta A, Kaplan D L, Naik R R, Verma N, Omenetto F G and McAlpine M C 2012 Graphene-based wireless bacteria detection on tooth enamel *Nat. Commun.* 3
- [79] Boland C S, Khan U, Backes C, O’Neill A, McCauley J, Duane S, Shanker R, Liu Y, Jurewicz I, Dalton A B and Coleman J N 2014 Sensitive, High-Strain, High-Rate Bodily Motion Sensors Based on Graphene–Rubber Composites *ACS Nano* 8 8819–30
- [80] Boland C S, Khan U, Ryan G, Barwich S, Charifou R, Harvey A, Backes C, Li Z, Ferreira M S, Möbius M E, Young R J and Coleman J N 2016 Sensitive electromechanical sensors using viscoelastic graphene-polymer nanocomposites *Science* 354 1257–60
- [81] Park Y, Shim J, Jeong S, Yi G-R, Chae H, Bae J W, Kim S O and Pang C 2017 Microtopography-Guided Conductive Patterns of Liquid-Driven Graphene Nanoplatelet Networks for Stretchable and Skin-Conformal Sensor Array *Adv. Mater.* 29 1606453

- [82] Li X, Yang T, Yang Y, Zhu J, Li L, Alam F E, Li X, Wang K, Cheng H, Lin C-T, Fang Y and Zhu H 2016 Large-Area Ultrathin Graphene Films by Single-Step Marangoni Self-Assembly for Highly Sensitive Strain Sensing Application *Adv. Funct. Mater.* 26 1322–9
- [83] Park J J, Hyun W J, Mun S C, Park Y T and Park O O 2015 Highly Stretchable and Wearable Graphene Strain Sensors with Controllable Sensitivity for Human Motion Monitoring *ACS Appl. Mater. Interfaces* 7 6317–24
- [84] Shi G, Zhao Z, Pai J-H, Lee I, Zhang L, Stevenson C, Ishara K, Zhang R, Zhu H and Ma J 2016 Highly Sensitive, Wearable, Durable Strain Sensors and Stretchable Conductors Using Graphene/Silicon Rubber Composites *Adv. Funct. Mater.* 26 7614–25
- [85] Lee S W, Park J J, Park B H, Mun S C, Park Y T, Liao K, Seo T S, Hyun W J and Park O O 2017 Enhanced Sensitivity of Patterned Graphene Strain Sensors Used for Monitoring Subtle Human Body Motions *ACS Appl. Mater. Interfaces* 9 11176–83
- [86] Ju Yun Y, Hong W G, Choi N-J, Hoon Kim B, Jun Y and Lee H-K 2015 Ultrasensitive and Highly Selective Graphene-Based Single Yarn for Use in Wearable Gas Sensor *Sci. Rep.* 5
- [87] Yuan W, Zhou Q, Li Y and Shi G 2015 Small and light strain sensors based on graphene coated human hairs *Nanoscale* 7 16361–5
- [88] Karim N, Afroj S, Tan S, He P, Fernando A, Carr C and Novoselov K S 2017 Scalable Production of Graphene-Based Wearable E-Textiles *ACS Nano* 11 12266–75
- [89] Zhu B, Niu Z, Wang H, Leow W R, Wang H, Li Y, Zheng L, Wei J, Huo F and Chen X 2014 Microstructured Graphene Arrays for Highly Sensitive Flexible Tactile Sensors *Small* 10 3625–31
- [90] Liu Q, Chen J, Li Y and Shi G 2016 High-Performance Strain Sensors with Fish-Scale-Like Graphene-Sensing Layers for Full-Range Detection of Human Motions *ACS Nano* 10 7901–6
- [91] Yapici M K, Alkhidir T, Samad Y A and Liao K 2015 Graphene-clad textile electrodes for electrocardiogram monitoring *Sens. Actuators B Chem.* 221 1469–74
- [92] Ren J, Wang C, Zhang X, Carey T, Chen K, Yin Y and Torrissi F 2017 Environmentally-friendly conductive cotton fabric as flexible strain sensor based on hot press reduced graphene oxide *Carbon* 111 622–30

- [93] Ai Y, Hsu T H, Wu D C, Lee L, Chen J-H, Chen Y-Z, Wu S-C, Wu C, Wang Z M and Chueh Y-L 2018 An ultrasensitive flexible pressure sensor for multimodal wearable electronic skins based on large-scale polystyrene ball@reduced graphene-oxide core-shell nanoparticles *J. Mater. Chem. C*
- [94] Trung T Q, Ramasundaram S, Hwang B-U and Lee N-E 2016 An All-Elastomeric Transparent and Stretchable Temperature Sensor for Body-Attachable Wearable Electronics *Adv. Mater.* 28 502–9
- [95] Chun S, Jung H, Choi Y, Bae G, Kil J P and Park W 2015 A tactile sensor using a graphene film formed by the reduced graphene oxide flakes and its detection of surface morphology *Carbon* 94 982–7
- [96] Xu H, Lu Y F, Xiang J X, Zhang M K, Zhao Y J, Xie Z Y and Gu Z Z 2018 A multifunctional wearable sensor based on a graphene/inverse opal cellulose film for simultaneous, *in situ* monitoring of human motion and sweat *Nanoscale* 10 2090–8
- [97] Trung T Q, Tien N T, Kim D, Jang M, Yoon O J and Lee N-E 2014 A Flexible Reduced Graphene Oxide Field-Effect Transistor for Ultrasensitive Strain Sensing *Adv. Funct. Mater.* 24 117–24
- [98] Wang Y, Wang L, Yang T, Li X, Zang X, Zhu M, Wang K, Wu D and Zhu H 2014 Wearable and Highly Sensitive Graphene Strain Sensors for Human Motion Monitoring *Adv. Funct. Mater.* 24 4666–70
- [99] Wang Y, Yang T, Lao J, Zhang R, Zhang Y, Zhu M, Li X, Zang X, Wang K, Yu W, Jin H, Wang L and Zhu H 2015 Ultra-sensitive graphene strain sensor for sound signal acquisition and recognition *Nano Res. Beijing* 8 1627–36
- [100] Yang T, Wang W, Zhang H, Li X, Shi J, He Y, Zheng Q, Li Z and Zhu H 2015 Tactile Sensing System Based on Arrays of Graphene Woven Microfabrics: Electromechanical Behavior and Electronic Skin Application *ACS Nano* 9 10867–75
- [101] Li X, Zhang R, Yu W, Wang K, Wei J, Wu D, Cao A, Li Z, Cheng Y, Zheng Q, Ruoff R S and Zhu H 2012 Stretchable and highly sensitive graphene-on-polymer strain sensors *Sci. Rep.* 2
- [102] Du D, Li P and Ouyang J 2016 Graphene coated nonwoven fabrics as wearable sensors *J. Mater. Chem. C* 4 3224–30

- [103] Yang T, Jiang X, Zhong Y, Zhao X, Lin S, Li J, Li X, Xu J, Li Z and Zhu H 2017 A Wearable and Highly Sensitive Graphene Strain Sensor for Precise Home-Based Pulse Wave Monitoring *ACS Sens.* 2 967–74
- [104] Du B, Yang D, She X, Yuan Y, Mao D, Jiang Y and Lu F 2017 MoS<sub>2</sub>-based all-fiber humidity sensor for monitoring human breath with fast response and recovery *Sens. Actuators B Chem.* 251 180–4
- [105] Park M, Park Y J, Chen X, Park Y-K, Kim M-S and Ahn J-H 2016 MoS<sub>2</sub> -Based Tactile Sensor for Electronic Skin Applications *Adv. Mater.* 28 2556–62
- [106] Chen X, Park Y J, Kang M, Kang S-K, Koo J, Shinde S M, Shin J, Jeon S, Park G, Yan Y, MacEwan M R, Ray W Z, Lee K-M, Rogers J A and Ahn J-H 2018 CVD-grown monolayer MoS<sub>2</sub> in bioabsorbable electronics and biosensors *Nat. Commun.* 9
- [107] Cai Y, Shen J, Ge G, Zhang Y, Jin W, Huang W, Shao J, Yang J and Dong X 2018 Stretchable Ti<sub>3</sub>C<sub>2</sub>T<sub>x</sub> MXene/Carbon Nanotube Composite Based Strain Sensor with Ultrahigh Sensitivity and Tunable Sensing Range *ACS Nano* 12 56–62
- [108] Jiang Q, Wu C, Wang Z, Wang A C, He J-H, Wang Z L and Alshareef H N 2018 MXene electrochemical microsupercapacitor integrated with triboelectric nanogenerator as a wearable self-charging power unit *Nano Energy* 45 266–72
- [109] Kedambaimoole V, Kumar N, Shirhatti V, Nuthalapati S, Sen P, Nayak M M, Rajanna K and Kumar S 2020 Laser-Induced Direct Patterning of Free-standing Ti<sub>3</sub>C<sub>2</sub>-MXene Films for Skin Conformal Tattoo Sensors *ACS Sens.* 5 2086–95
- [110] Levitt A, Zhang J, Dion G, Gogotsi Y and Razal J M 2020 MXene-Based Fibers, Yarns, and Fabrics for Wearable Energy Storage Devices *Adv. Funct. Mater.* 2000739
- [111] Li L, Fu X, Chen S, Uzun S, Levitt A S, Shuck C E, Han W and Gogotsi Y 2020 Hydrophobic and Stable MXene–Polymer Pressure Sensors for Wearable Electronics *ACS Appl. Mater. Interfaces* 12 15362–9
- [112] Seyedin S, Uzun S, Levitt A, Anasori B, Dion G, Gogotsi Y and Razal J M 2020 MXene Composite and Coaxial Fibers with High Stretchability and Conductivity for Wearable Strain Sensing Textiles *Adv. Funct. Mater.* 30 1910504
- [113] Yang Y, Shi L, Cao Z, Wang R and Sun J 2019 Strain Sensors with a High Sensitivity and a Wide Sensing Range Based on a Ti<sub>3</sub>C<sub>2</sub>T<sub>x</sub> (MXene) Nanoparticle–Nanosheet Hybrid Network *Adv. Funct. Mater.* 29 1807882

- [114] Li Q, Ullah Z, Li W, Guo Y, Xu J, Wang R, Zeng Q, Chen M, Liu C and Liu L 2016 Wide-Range Strain Sensors Based on Highly Transparent and Supremely Stretchable Graphene/Ag-Nanowires Hybrid Structures *Small* 12 5058–65
- [115] Park J, Kim J, Kim K, Kim S-Y, Hyung Cheong W, Park K, Hyeon Song J, Namgoong G, Joon Kim J, Heo J, Bien F and Park J-U 2016 Wearable, wireless gas sensors using highly stretchable and transparent structures of nanowires and graphene *Nanoscale* 8 10591–7
- [116] Kim J, Kim M, Lee M-S, Kim K, Ji S, Kim Y-T, Park J, Na K, Bae K-H, Kyun Kim H, Bien F, Young Lee C and Park J-U 2017 Wearable smart sensor systems integrated on soft contact lenses for wireless ocular diagnostics *Nat. Commun.* 8 14997
- [117] Choi T Y, Hwang B-U, Kim B-Y, Trung T Q, Nam Y H, Kim D-N, Eom K and Lee N-E 2017 Stretchable, Transparent, and Stretch-Unresponsive Capacitive Touch Sensor Array with Selectively Patterned Silver Nanowires/Reduced Graphene Oxide Electrodes *ACS Appl. Mater. Interfaces* 9 18022–30
- [118] Shi X, Liu S, Sun Y, Liang J and Chen Y 2018 Lowering Internal Friction of 0D–1D–2D Ternary Nanocomposite-Based Strain Sensor by Fullerene to Boost the Sensing Performance *Adv. Funct. Mater.* 28 1800850
- [119] Kim J, Lee M-S, Jeon S, Kim M, Kim S, Kim K, Bien F, Hong S Y and Park J-U 2015 Highly Transparent and Stretchable Field-Effect Transistor Sensors Using Graphene–Nanowire Hybrid Nanostructures *Adv. Mater.* 27 3292–7
- [120] Lee J S, Shin K-Y, Cheong O J, Kim J H and Jang J 2015 Highly Sensitive and Multifunctional Tactile Sensor Using Free-standing ZnO/PVDF Thin Film with Graphene Electrodes for Pressure and Temperature Monitoring *Sci. Rep.* 5
- [121] Shi J, Li X, Cheng H, Liu Z, Zhao L, Yang T, Dai Z, Cheng Z, Shi E, Yang L, Zhang Z, Cao A, Zhu H and Fang Y 2016 Graphene Reinforced Carbon Nanotube Networks for Wearable Strain Sensors *Adv. Funct. Mater.* 26 2078–84
- [122] Park J W and Jang J 2015 Fabrication of graphene/free-standing nanofibrillar PEDOT/P(VDF-HFP) hybrid device for wearable and sensitive electronic skin application *Carbon* 87 275–81
- [123] Yan T, Wang Z, Wang Y-Q and Pan Z-J 2018 Carbon/graphene composite nanofiber yarns for highly sensitive strain sensors *Mater. Des.* 143 214–23

- [124] Chen S, Wei Y, Yuan X, Lin Y and Liu L 2016 A highly stretchable strain sensor based on a graphene/silver nanoparticle synergic conductive network and a sandwich structure *J. Mater. Chem. C* 4 4304–11
- [125] Yang Y, Yang X, Zou X, Wu S, Wan D, Cao A, Liao L, Yuan Q and Duan X 2017 Ultrafine Graphene Nanomesh with Large On/Off Ratio for High-Performance Flexible Biosensors *Adv. Funct. Mater.* 27 1604096
- [126] Eswaraiyah V, Balasubramaniam K and Ramaprabhu S 2012 One-pot synthesis of conducting graphene – polymer composites and their strain sensing application *Nanoscale* 4 1258–62
- [127] Lou Z, Chen S, Wang L, Jiang K and Shen G 2016 An ultra-sensitive and rapid response speed graphene pressure sensors for electronic skin and health monitoring *Nano Energy* 23 7–14
- [128] Wang T, Guo Y, Wan P, Sun X, Zhang H, Yu Z and Chen X 2017 A flexible transparent colorimetric wrist strap sensor *Nanoscale* 9 869–74
- [129] Hou C, Wang H, Zhang Q, Li Y and Zhu M 2014 Highly Conductive, Flexible, and Compressible All-Graphene Passive Electronic Skin for Sensing Human Touch *Adv. Mater.* 26 5018–24
- [130] Yang J, Wei D, Tang L, Song X, Luo W, Chu J, Gao T, Shi H and Du C 2015 Wearable temperature sensor based on graphene nanowalls *RSC Adv.* 5 25609–15
- [131] Tian H, Shu Y, Wang X-F, Mohammad M A, Bie Z, Xie Q-Y, Li C, Mi W-T, Yang Y and Ren T-L 2015 A Graphene-Based Resistive Pressure Sensor with Record-High Sensitivity in a Wide Pressure Range *Sci. Rep.* 5 8603
- [132] Tao L-Q, Wang D-Y, Tian H, Ju Z-Y, Liu Y, Pang Y, Chen Y-Q, Yang Y and Ren T-L 2017 Self-adapted and tunable graphene strain sensors for detecting both subtle and large human motions *Nanoscale* 9 8266–73
- [133] Jeong Y R, Park H, Jin S W, Hong S Y, Lee S-S and Ha J S 2015 Highly Stretchable and Sensitive Strain Sensors Using Fragmentized Graphene Foam *Adv. Funct. Mater.* 25 4228–36
- [134] Nakamura A, Hamanishi T, Kawakami S and Takeda M 2017 A piezo-resistive graphene strain sensor with a hollow cylindrical geometry *Mater. Sci. Eng. B* 219 20–7
- [135] Yan C, Wang J, Kang W, Cui M, Wang X, Foo C Y, Chee K J and Lee P S 2014 Highly Stretchable Piezoresistive Graphene–Nanocellulose Nanopaper for Strain Sensors *Adv. Mater.* 26 2022–7

- [136] Yoon J, Park W, Bae G-Y, Kim Y, Jang H S, Hyun Y, Lim S K, Kahng Y H, Hong W-K, Lee B H and Ko H C 2013 Highly Flexible and Transparent Multilayer MoS<sub>2</sub> Transistors with Graphene Electrodes *Small* n/a-n/a
- [137] He Q, Zeng Z, Yin Z, Li H, Wu S, Huang X and Zhang H 2012 Fabrication of Flexible MoS<sub>2</sub> Thin-Film Transistor Arrays for Practical Gas-Sensing Applications *Small* 8 2994–9
- [138] Yang Y-F, Tao L-Q, Pang Y, Tian H, Ju Z, Wu X-M, Yang Y and Ren T-L 2018 An Ultrasensitive Strain Sensor with Large Strain Range Based on Graphene Armour Scales *Nanoscale*
- [139] Cui C, Xue F, Hu W-J and Li L-J 2018 Two-dimensional materials with piezoelectric and ferroelectric functionalities *Npj 2D Mater. Appl.* 2
- [140] Gan X, Zhao H and Quan X 2017 Two-dimensional MoS<sub>2</sub>: A promising building block for biosensors *Biosens. Bioelectron.* 89 56–71
- [141] Huang X, Yin Z, Wu S, Qi X, He Q, Zhang Q, Yan Q, Boey F and Zhang H 2011 Graphene-Based Materials: Synthesis, Characterization, Properties, and Applications *Small* 7 1876–902
- [142] Nag A, Mitra A and Mukhopadhyay S C 2018 Graphene and its sensor-based applications: A review *Sens. Actuators Phys.* 270 177–94
- [143] Reina A, Jia X, Ho J, Nezich D, Son H, Bulovic V, Dresselhaus M S and Kong J 2009 Large Area, Few-Layer Graphene Films on Arbitrary Substrates by Chemical Vapor Deposition *Nano Lett.* 9 30–5
- [144] Li X, Cai W, An J, Kim S, Nah J, Yang D, Piner R, Velamakanni A, Jung I, Tutuc E, Banerjee S K, Colombo L and Ruoff R S 2009 Large-Area Synthesis of High-Quality and Uniform Graphene Films on Copper Foils *Science* 324 1312–4
- [145] Eda G, Fanchini G and Chhowalla M 2008 Large-area ultrathin films of reduced graphene oxide as a transparent and flexible electronic material *Nat. Nanotechnol.* 3 270–4
- [146] Liu H, Liu Y and Zhu D 2011 Chemical doping of graphene *J Mater Chem* 21 3335–45
- [147] Huo N and Konstantatos G 2018 Recent Progress and Future Prospects of 2D-Based Photodetectors *Adv. Mater.* 30 1801164
- [148] Jeong Y R, Kim J, Xie Z, Xue Y, Won S M, Lee G, Jin S W, Hong S Y, Feng X, Huang Y, Rogers J A and Ha J S 2017 A skin-attachable, stretchable integrated

system based on liquid GaInSn for wireless human motion monitoring with multi-site sensing capabilities *NPG Asia Mater.* 9 e443

- [149] Guo H, Lan C, Zhou Z, Sun P, Wei D and Li C 2017 Transparent, flexible, and stretchable WS<sub>2</sub> based humidity sensors for electronic skin *Nanoscale* 9 6246–53
- [150] Wang Y, Qiu Y, Ameri S K, Jang H, Dai Z, Huang Y and Lu N 2018 Low-cost,  $\mu\text{m}$ -thick, tape-free electronic tattoo sensors with minimized motion and sweat artifacts *Npj Flex. Electron.* 2
- [151] Lee H, Choi T K, Lee Y B, Cho H R, Ghaffari R, Wang L, Choi H J, Chung T D, Lu N, Hyeon T, Choi S H and Kim D-H 2016 A graphene-based electrochemical device with thermoresponsive microneedles for diabetes monitoring and therapy *Nat. Nanotechnol.* 11 566–72
- [152] Kim D-H, Lu N, Ma R, Kim Y-S, Kim R-H, Wang S, Wu J, Won S M, Tao H, Islam A, Yu K J, Kim T, Chowdhury R, Ying M, Xu L, Li M, Chung H-J, Keum H, McCormick M, Liu P, Zhang Y-W, Omenetto F G, Huang Y, Coleman T and Rogers J A 2011 Epidermal Electronics *Science* 333 838–43
- [153] Lee Y, Kim J, Jang B, Kim S, Sharma B K, Kim J-H and Ahn J-H 2019 Graphene-based stretchable/wearable self-powered touch sensor *Nano Energy* 62 259–67
- [154] Andrzejewski D, Oliver R, Beckmann Y, Grundmann A, Heuken M, Kalisch H, Vescan A, Kümmell T and Bacher G 2020 Flexible Large-Area Light-Emitting Devices Based on WS<sub>2</sub> Monolayers *Adv. Opt. Mater.* 8 2000694
- [155] Liu Y and Peng X 2017 Recent advances of supercapacitors based on two-dimensional materials *Appl. Mater. Today* 8 104–15
- [156] Wu W, Wang L, Li Y, Zhang F, Lin L, Niu S, Chenet D, Zhang X, Hao Y, Heinz T F, Hone J and Wang Z L 2014 Piezoelectricity of single-atomic-layer MoS<sub>2</sub> for energy conversion and piezotronics *Nature* 514 470–4
- [157] Ko H C, Stoykovich M P, Song J, Malyarchuk V, Choi W M, Yu C-J, Geddes III J B, Xiao J, Wang S, Huang Y and Rogers J A 2008 A hemispherical electronic eye camera based on compressible silicon optoelectronics *Nature* 454 748–53
- [158] Jones J, Lacour S P, Wagner S and Suo Z 2004 Stretchable wavy metal interconnects *J. Vac. Sci. Technol. Vac. Surf. Films* 22 1723–5
- [159] Wang X, Feiner R, Luan H, Zhang Q, Zhao S, Zhang Y, Han M, Li Y, Sun R, Wang H, Liu T-L, Guo X, Oved H, Noor N, Shapira A, Zhang Y, Huang Y, Dvir T

- and Rogers J A 2020 Three-dimensional electronic scaffolds for monitoring and regulation of multifunctional hybrid tissues *Extreme Mech. Lett.* 35 100634
- [160] Gray D S, Tien J and Chen C S 2004 High-Conductivity Elastomeric Electronics *Adv. Mater.* 16 393–7
- [161] Li T, Suo Z, Lacour S P and Wagner S 2005 Compliant thin film patterns of stiff materials as platforms for stretchable electronics *J. Mater. Res.* 20 3274–7
- [162] Yang S, Qiao S and Lu N 2017 Elasticity Solutions to Nonbuckling Serpentine Ribbons *J. Appl. Mech.* 84 021004
- [163] Xu S, Zhang Y, Cho J, Lee J, Huang X, Jia L, Fan J A, Su Y, Su J, Zhang H, Cheng H, Lu B, Yu C, Chuang C, Kim T, Song T, Shigeta K, Kang S, Dagdeviren C, Petrov I, Braun P V, Huang Y, Paik U and Rogers J A 2013 Stretchable batteries with self-similar serpentine interconnects and integrated wireless recharging systems *Nat. Commun.* 4 1543
- [164] Xian Huang, Huanyu Cheng, Kaile Chen, Yilin Zhang, Yihui Zhang, Yuhao Liu, Chenqi Zhu, Shao-chi Ouyang, Gil-Woo Kong, Cunjiang Yu, Yonggang Huang and Rogers J A 2013 Epidermal Impedance Sensing Sheets for Precision Hydration Assessment and Spatial Mapping *IEEE Trans. Biomed. Eng.* 60 2848–57
- [165] Xiao L, Zhu C, Xiong W, Huang Y and Yin Z 2018 The Conformal Design of an Island-Bridge Structure on a Non-Developable Surface for Stretchable Electronics *Micromachines* 9 392
- [166] Kim D-H, Lu N, Ma R, Kim Y-S, Kim R-H, Wang S, Wu J, Won S M, Tao H, Islam A, Yu K J, Kim T -i., Chowdhury R, Ying M, Xu L, Li M, Chung H-J, Keum H, McCormick M, Liu P, Zhang Y-W, Omenetto F G, Huang Y, Coleman T and Rogers J A 2011 Epidermal Electronics *Science* 333 838–43
- [167] Ha T, Tran J, Liu S, Jang H, Jeong H, Mitbender R, Huh H, Qiu Y, Duong J, Wang R L, Wang P, Tandon A, Sirohi J and Lu N 2019 A Chest-Laminated Ultrathin and Stretchable E-Tattoo for the Measurement of Electrocardiogram, Seismocardiogram, and Cardiac Time Intervals *Adv. Sci.* 1900290
- [168] Choi S, Han S I, Jung D, Hwang H J, Lim C, Bae S, Park O K, Tschabrunn C M, Lee M, Bae S Y, Yu J W, Ryu J H, Lee S-W, Park K, Kang P M, Lee W B, Nezafat R, Hyeon T and Kim D-H 2018 Highly conductive, stretchable and biocompatible Ag–Au core–sheath nanowire composite for wearable and implantable bioelectronics *Nat. Nanotechnol.*

- [169] Kabiri Ameri S, Ho R, Jang H, Tao L, Wang Y, Wang L, Schnyer D M, Akinwande D and Lu N 2017 Graphene Electronic Tattoo Sensors *ACS Nano* 11 7634–41
- [170] Li L, Lin H, Qiao S, Huang Y-Z, Li J-Y, Michon J, Gu T, Alosno-Ramos C, Vivien L, Yadav A, Richardson K, Lu N and Hu J 2018 Monolithically integrated stretchable photonics *Light Sci. Appl.* 7 17138–17138
- [171] Wang Y, Yin L, Bai Y, Liu S, Wang L, Zhou Y, Hou C, Yang Z, Wu H, Ma J, Shen Y, Deng P, Zhang S, Duan T, Li Z, Ren J, Xiao L, Yin Z, Lu N and Huang Y 2020 Electrically compensated, tattoo-like electrodes for epidermal electrophysiology at scale *Sci. Adv.* 6 eabd0996
- [172] Fan J A, Yeo W-H, Su Y, Hattori Y, Lee W, Jung S-Y, Zhang Y, Liu Z, Cheng H, Falgout L, Bajema M, Coleman T, Gregoire D, Larsen R J, Huang Y and Rogers J A 2014 Fractal design concepts for stretchable electronics *Nat. Commun.* 5 3266
- [173] Zhang Y, Fu H, Su Y, Xu S, Cheng H, Fan J A, Hwang K-C, Rogers J A and Huang Y 2013 Mechanics of ultra-stretchable self-similar serpentine interconnects *Acta Mater.* 61 7816–27
- [174] Xu L, Gutbrod S R, Ma Y, Petrossians A, Liu Y, Webb R C, Fan J A, Yang Z, Xu R, Whalen J J, Weiland J D, Huang Y, Efimov I R and Rogers J A 2015 Materials and Fractal Designs for 3D Multifunctional Integumentary Membranes with Capabilities in Cardiac Electrotherapy *Adv. Mater.* 27 1731–7
- [175] Jang K-I, Chung H U, Xu S, Lee C H, Luan H, Jeong J, Cheng H, Kim G-T, Han S Y, Lee J W, Kim J, Cho M, Miao F, Yang Y, Jung H N, Flavin M, Liu H, Kong G W, Yu K J, Rhee S I, Chung J, Kim B, Kwak J W, Yun M H, Kim J Y, Song Y M, Paik U, Zhang Y, Huang Y and Rogers J A 2015 Soft network composite materials with deterministic and bio-inspired designs *Nat. Commun.* 6 6566
- [176] Lee W, Kobayashi S, Nagase M, Jimbo Y, Saito I, Inoue Y, Yambe T, Sekino M, Malliaras G G, Yokota T, Tanaka M and Someya T 2018 Nonthrombogenic, stretchable, active multielectrode array for electroanatomical mapping *Sci. Adv.* 4 eaau2426
- [177] Li H, Ma Y, Liang Z, Wang Z, Cao Y, Xu Y, Zhou H, Lu B, Chen Y, Han Z, Cai S and Feng X 2020 Wearable skin-like optoelectronic systems with suppression of motion artifacts for cuff-less continuous blood pressure monitor *Natl. Sci. Rev.* 7 849–62

- [178] Morikawa Y, Yamagiwa S, Sawahata H, Numano R, Koida K, Ishida M and Kawano T 2018 Ultrastretchable Kirigami Bioprobes *Adv. Healthc. Mater.* 7 1701100
- [179] Matsuhisa N, Chen X, Bao Z and Someya T 2019 Materials and structural designs of stretchable conductors *Chem. Soc. Rev.* 48 2946–66
- [180] Morikawa Y, Yamagiwa S, Sawahata H, Numano R, Koida K and Kawano T 2019 Donut-Shaped Stretchable Kirigami: Enabling Electronics to Integrate with the Deformable Muscle *Adv. Healthc. Mater.* 8 1900939
- [181] Sun R, Carreira S C, Chen Y, Xiang C, Xu L, Zhang B, Chen M, Farrow I, Scarpa F and Rossiter J 2019 Stretchable Piezoelectric Sensing Systems for Self-Powered and Wireless Health Monitoring *Adv. Mater. Technol.* 4 1900100
- [182] Xu X, Xie S, Zhang Y and Peng H 2019 The Rise of Fiber Electronics *Angew. Chem. Int. Ed.* 58 13643–53
- [183] Miyamoto A, Lee S, Cooray N F, Lee S, Mori M, Matsuhisa N, Jin H, Yoda L, Yokota T, Itoh A, Sekino M, Kawasaki H, Ebihara T, Amagai M and Someya T 2017 Inflammation-free, gas-permeable, lightweight, stretchable on-skin electronics with nanomeshes *Nat. Nanotechnol.* 12 907–13
- [184] Zhong J, Zhang Y, Zhong Q, Hu Q, Hu B, Wang Z L and Zhou J 2014 Fiber-Based Generator for Wearable Electronics and Mobile Medication *ACS Nano* 8 6273–80
- [185] Lee J, Kwon H, Seo J, Shin S, Koo J H, Pang C, Son S, Kim J H, Jang Y H, Kim D E and Lee T 2015 Conductive Fiber-Based Ultrasensitive Textile Pressure Sensor for Wearable Electronics *Adv. Mater.* 27 2433–9
- [186] Zeng W, Shu L, Li Q, Chen S, Wang F and Tao X-M 2014 Fiber-Based Wearable Electronics: A Review of Materials, Fabrication, Devices, and Applications *Adv. Mater.* 26 5310–36
- [187] Kireev D, Okogbue E, RT J, Ko T-J, Jung Y and Akinwande D 2020 Multipurpose and Reusable Ultrathin Electronic Tattoos Based on PtSe<sub>2</sub> and PtTe<sub>2</sub> *ArXiv201007534 Cond-Mat*
- [188] Karim N, Afroj S, Malandraki A, Butterworth S, Beach C, Rigout M, Novoselov K S, Casson A J and Yeates S G 2017 All inkjet-printed graphene-based conductive patterns for wearable e-textile applications *J. Mater. Chem. C* 5 11640–8

- [189] Chandrashekar B N, Deng B, Smitha A S, Chen Y, Tan C, Zhang H, Peng H and Liu Z 2015 Roll-to-Roll Green Transfer of CVD Graphene onto Plastic for a Transparent and Flexible Triboelectric Nanogenerator *Adv. Mater.* 27 5210–6
- [190] Kwon S, Kim S, Kim I, Hong Y K and Na S 2018 Direct 3D Printing of Graphene Nanoplatelet/Silver Nanoparticle-Based Nanocomposites for Multiaxial Piezoresistive Sensor Applications *Adv. Mater. Technol.* 1800500
- [191] Tao L-Q, Tian H, Liu Y, Ju Z-Y, Pang Y, Chen Y-Q, Wang D-Y, Tian X-G, Yan J-C, Deng N-Q, Yang Y and Ren T-L 2017 An intelligent artificial throat with sound-sensing ability based on laser induced graphene *Nat. Commun.* 8 14579
- [192] Qiao Y, Wang Y, Tian H, Li M, Jian J, Wei Y, Tian Y, Wang D-Y, Pang Y, Geng X, Wang X, Zhao Y, Wang H, Deng N, Jian M, Zhang Y, Liang R, Yang Y and Ren T-L 2018 Multilayer Graphene Epidermal Electronic Skin *ACS Nano*
- [193] Setti L, Fraleoni-Morgera A, Ballarin B, Filippini A, Frascaro D and Piana C 2005 An amperometric glucose biosensor prototype fabricated by thermal inkjet printing *Biosens. Bioelectron.* 20 2019–26
- [194] Secor E B, Prabhumirashi P L, Puntambekar K, Geier M L and Hersam M C 2013 Inkjet Printing of High Conductivity, Flexible Graphene Patterns *J. Phys. Chem. Lett.* 4 1347–51
- [195] Lin J, Peng Z, Liu Y, Ruiz-Zepeda F, Ye R, Samuel E L G, Yacaman M J, Yakobson B I and Tour J M 2014 Laser-induced porous graphene films from commercial polymers *Nat. Commun.* 5 5714
- [196] Zhang Z, Song M, Hao J, Wu K, Li C and Hu C 2018 Visible light laser-induced graphene from phenolic resin: A new approach for directly writing graphene-based electrochemical devices on various substrates *Carbon* 127 287–96
- [197] Carvalho A F, Fernandes A J S, Leitão C, Deuermeier J, Marques A C, Martins R, Fortunato E and Costa F M 2018 Laser-Induced Graphene Strain Sensors Produced by Ultraviolet Irradiation of Polyimide *Adv. Funct. Mater.* 28 1805271
- [198] Liu W, Huang Y, Peng Y, Walczak M, Wang D, Chen Q, Liu Z and Li L 2020 Stable Wearable Strain Sensors on Textiles by Direct Laser Writing of Graphene *ACS Appl. Nano Mater.* 3 283–93
- [199] Zhao J, Zhang G-Y and Shi D-X 2013 Review of graphene-based strain sensors *Chin. Phys. B* 22 057701
- [200] Hempel M, Nezich D, Kong J and Hofmann M 2012 A Novel Class of Strain Gauges Based on Layered Percolative Films of 2D Materials *Nano Lett.* 12 5714–8

- [201] Fiori G, Bonaccorso F, Iannaccone G, Palacios T, Neumaier D, Seabaugh A, Banerjee S K and Colombo L 2014 Electronics based on two-dimensional materials *Nat. Nanotechnol.* 9 768–79
- [202] Ferrari L M, Sudha S, Tarantino S, Esposti R, Bolzoni F, Cavallari P, Cipriani C, Mattoli V and Greco F 2018 Ultraconformable Temporary Tattoo Electrodes for Electrophysiology *Adv. Sci.* 5 1700771
- [203] Mostafalu P and Sonkusale S 2015 A high-density nanowire electrode on paper for biomedical applications *RSC Adv.* 5 8680–7
- [204] Kireev D, Okogbue E, Jayanth R, Ko T-J, Jung Y and Akinwande D 2021 Multipurpose and Reusable Ultrathin Electronic Tattoos Based on PtSe<sub>2</sub> and PtTe<sub>2</sub> *ACS Nano* acsnano.0c08689
- [205] Steinhubl S R, Muse E D and Topol E J 2015 The emerging field of mobile health *Sci. Transl. Med.* 7
- [206] Jeong J-W, Yeo W-H, Akhtar A, Norton J J S, Kwack Y-J, Li S, Jung S-Y, Su Y, Lee W, Xia J, Cheng H, Huang Y, Choi W-S, Bretl T and Rogers J A 2013 Materials and Optimized Designs for Human-Machine Interfaces Via Epidermal Electronics *Adv. Mater.* 25 6839–46
- [207] Wang S, Li M, Wu J, Kim D-H, Lu N, Su Y, Kang Z, Huang Y and Rogers J A 2012 Mechanics of Epidermal Electronics *J. Appl. Mech.* 79 031022
- [208] Arumugam V, Naresh M D and Sanjeevi R 1994 Effect of strain rate on the fracture behaviour of skin *J. Biosci.* 19 307–13
- [209] Park D-W, Schendel A A, Mikael S, Brodnick S K, Richner T J, Ness J P, Hayat M R, Atry F, Frye S T, Pashaie R, Thongpang S, Ma Z and Williams J C 2014 Graphene-based carbon-layered electrode array technology for neural imaging and optogenetic applications *Nat. Commun.* 5 5258
- [210] Wang L and Lu N 2016 Conformability of a Thin Elastic Membrane Laminated on a Soft Substrate With Slightly Wavy Surface *J. Appl. Mech.* 83 041007
- [211] Chi Y M, Jung T-P and Cauwenberghs G 2010 Dry-Contact and Noncontact Biopotential Electrodes: Methodological Review *IEEE Rev. Biomed. Eng.* 3 106–19
- [212] Celik N, Manivannan N, Strudwick A and Balachandran W 2016 Graphene-Enabled Electrodes for Electrocardiogram Monitoring *Nanomaterials* 6 156

- [213] Koo J H, Kim D C, Shim H J, Kim T-H and Kim D-H 2018 Flexible and Stretchable Smart Display: Materials, Fabrication, Device Design, and System Integration *Adv. Funct. Mater.* 0 1801834
- [214] Lu N and Kim D-H 2014 Flexible and Stretchable Electronics Paving the Way for Soft Robotics *Soft Robot.* 1 53–62
- [215] Fan F R, Tang W and Wang Z L 2016 Flexible Nanogenerators for Energy Harvesting and Self-Powered Electronics *Adv. Mater.* 28 4283–305
- [216] Lu N and Yang S 2015 Mechanics for stretchable sensors *Curr. Opin. Solid State Mater. Sci.* 19 149–59
- [217] Yao S and Zhu Y 2015 Nanomaterial-Enabled Stretchable Conductors: Strategies, Materials and Devices *Adv. Mater.* 27 1480–511
- [218] Cao Q and Rogers J A 2009 Ultrathin Films of Single-Walled Carbon Nanotubes for Electronics and Sensors: A Review of Fundamental and Applied Aspects *Adv. Mater.* 21 29–53
- [219] Chae S H and Lee Y H 2014 Carbon nanotubes and graphene towards soft electronics *Nano Converg.* 1 15
- [220] Lee P, Lee J, Lee H, Yeo J, Hong S, Nam K H, Lee D, Lee S S and Ko S H 2012 Highly Stretchable and Highly Conductive Metal Electrode by Very Long Metal Nanowire Percolation Network *Adv. Mater.* 24 3326–32
- [221] Langley D, Giusti G, Mayousse C, Celle C, Bellet D and Simonato J-P 2013 Flexible transparent conductive materials based on silver nanowire networks: a review *Nanotechnology* 24 452001
- [222] Akinwande D, Petrone N and Hone J 2014 Two-dimensional flexible nanoelectronics *Nat. Commun.* 5 5678
- [223] Zhuang X, Mai Y, Wu D, Zhang F and Feng X 2015 Two-Dimensional Soft Nanomaterials: A Fascinating World of Materials *Adv. Mater.* 27 403–27
- [224] Lee C, Wei X, Kysar J W and Hone J 2008 Measurement of the Elastic Properties and Intrinsic Strength of Monolayer Graphene *Science* 321 385–8
- [225] Bae S, Kim H, Lee Y, Xu X, Park J-S, Zheng Y, Balakrishnan J, Lei T, Kim H R, Song Y I, Kim Y-J, Kim K S, Özyilmaz B, Ahn J-H, Hong B H and Iijima S 2010 Roll-to-roll production of 30-inch graphene films for transparent electrodes *Nat. Nanotechnol.* 5 574–8

- [226] Zhu J, Yang D, Yin Z, Yan Q and Zhang H 2014 Graphene and Graphene-Based Materials for Energy Storage Applications *Small* 10 3480–98
- [227] Jang H, Park Y J, Chen X, Das T, Kim M-S and Ahn J-H 2016 Graphene-Based Flexible and Stretchable Electronics *Adv. Mater.* 28 4184–202
- [228] Ghosh S, Calizo I, Teweldebrhan D, Pokatilov E P, Nika D L, Balandin A A, Bao W, Miao F and Lau C N 2008 Extremely high thermal conductivity of graphene: Prospects for thermal management applications in nanoelectronic circuits *Appl. Phys. Lett.* 92 151911
- [229] Renteria J, Nika D and Balandin A 2014 Graphene Thermal Properties: Applications in Thermal Management and Energy Storage *Appl. Sci.* 4 525–47
- [230] Sgouros A P, Kalosakas G, Galiotis C and Papagelis K 2016 Uniaxial compression of suspended single and multilayer graphenes *2D Mater.* 3 025033
- [231] Hwangbo Y, Lee C-K, Kim S-M, Kim J-H, Kim K-S, Jang B, Lee H-J, Lee S-K, Kim S-S, Ahn J-H and Lee S-M 2015 Fracture Characteristics of Monolayer CVD-Graphene *Sci. Rep.* 4 4439
- [232] Lee S-M, Kim J-H and Ahn J-H 2015 Graphene as a flexible electronic material: mechanical limitations by defect formation and efforts to overcome *Mater. Today* 18 336–44
- [233] Wei X, Mao L, Soler-Crespo R A, Paci J T, Huang J, Nguyen S T and Espinosa H D 2015 Plasticity and ductility in graphene oxide through a mechanochemically induced damage tolerance mechanism *Nat. Commun.* 6
- [234] López-Polín G, Gómez-Herrero J and Gómez-Navarro C 2015 Confining Crack Propagation in Defective Graphene *Nano Lett.* 15 2050–4
- [235] Lee J-H, Jang D-W, Hong S-G, Park B C, Kim J-H, Jung H-J and Lee S-B 2017 Fracture mechanism and electromechanical behavior of chemical vapor deposited graphene on flexible substrate under tension *Carbon* 118 475–84
- [236] Anagnostopoulos G, Pappas P-N, Li Z, Kinloch I A, Young R J, Novoselov K S, Lu C Y, Pugno N, Parthenios J, Galiotis C and Papagelis K 2016 Mechanical Stability of Flexible Graphene-Based Displays *ACS Appl. Mater. Interfaces* 8 22605–14
- [237] Verma V P, Das S, Lahiri I and Choi W 2010 Large-area graphene on polymer film for flexible and transparent anode in field emission device *Appl. Phys. Lett.* 96 203108

- [238] Lee S-K, Kim B J, Jang H, Yoon S C, Lee C, Hong B H, Rogers J A, Cho J H and Ahn J-H 2011 Stretchable Graphene Transistors with Printed Dielectrics and Gate Electrodes *Nano Lett.* 11 4642–6
- [239] Won S, Hwangbo Y, Lee S-K, Kim K-S, Kim K-S, Lee S-M, Lee H-J, Ahn J-H, Kim J-H and Lee S-B 2014 Double-layer CVD graphene as stretchable transparent electrodes *Nanoscale* 6 6057–64
- [240] Chen Z, Xu C, Ma C, Ren W and Cheng H-M 2013 Lightweight and Flexible Graphene Foam Composites for High-Performance Electromagnetic Interference Shielding *Adv. Mater.* 25 1296–300
- [241] Liu N, Chortos A, Lei T, Jin L, Kim T R, Bae W-G, Zhu C, Wang S, Pfattner R, Chen X, Sinclair R and Bao Z 2017 Ultratransparent and stretchable graphene electrodes *Sci. Adv.* 3 e1700159
- [242] Li X, Sun P, Fan L, Zhu M, Wang K, Zhong M, Wei J, Wu D, Cheng Y and Zhu H 2012 Multifunctional graphene woven fabrics *Sci. Rep.* 2
- [243] Papageorgiou D G, Kinloch I A and Young R J 2017 Mechanical properties of graphene and graphene-based nanocomposites *Prog. Mater. Sci.* 90 75–127
- [244] Gong L, Kinloch I A, Young R J, Riaz I, Jalil R and Novoselov K S 2010 Interfacial Stress Transfer in a Graphene Monolayer Nanocomposite *Adv. Mater.* 22 2694–7
- [245] Sanchez D A, Dai Z, Wang P, Cantu-Chavez A, Brennan C J, Huang R and Lu N 2018 Mechanics of spontaneously formed nanoblisters trapped by transferred 2D crystals *Proc. Natl. Acad. Sci.* 115 7884–9
- [246] Wang G, Dai Z, Wang Y, Tan P, Liu L, Xu Z, Wei Y, Huang R and Zhang Z 2017 Measuring Interlayer Shear Stress in Bilayer Graphene *Phys. Rev. Lett.* 119 036101
- [247] Jang H, Dai Z, Ha K-H, Ameri S K and Lu N 2019 Stretchability of PMMA-supported CVD graphene and of its electrical contacts *2D Mater.* 7 014003
- [248] Ni Z H, Yu T, Lu Y H, Wang Y Y, Feng Y P and Shen Z X 2008 Uniaxial Strain on Graphene: Raman Spectroscopy Study and Band-Gap Opening *ACS Nano* 2 2301–5
- [249] Deng S and Berry V 2016 Wrinkled, rippled and crumpled graphene: an overview of formation mechanism, electronic properties, and applications *Mater. Today* 19 197–212

- [250] Yu Z, Niu X, Liu Z and Pei Q 2011 Intrinsically Stretchable Polymer Light-Emitting Devices Using Carbon Nanotube-Polymer Composite Electrodes *Adv. Mater.* 23 3989–94
- [251] Gao W and Tkatchenko A 2015 Sliding Mechanisms in Multilayered Hexagonal Boron Nitride and Graphene: The Effects of Directionality, Thickness, and Sliding Constraints *Phys. Rev. Lett.* 114
- [252] Liu Z, Yang J, Grey F, Liu J Z, Liu Y, Wang Y, Yang Y, Cheng Y and Zheng Q 2012 Observation of Microscale Superlubricity in Graphite *Phys. Rev. Lett.* 108
- [253] Rafiee M A, Rafiee J, Srivastava I, Wang Z, Song H, Yu Z-Z and Koratkar N 2010 Fracture and Fatigue in Graphene Nanocomposites *Small* 6 179–83
- [254] Shen M-Y, Chang T-Y, Hsieh T-H, Li Y-L, Chiang C-L, Yang H and Yip M-C 2013 Mechanical Properties and Tensile Fatigue of Graphene Nanoplatelets Reinforced Polymer Nanocomposites *J. Nanomater.* 2013 1–9
- [255] Hoey D and Taylor D 2009 Comparison of the fatigue behaviour of two different forms of PMMA *Fatigue Fract. Eng. Mater. Struct.* 32 261–9
- [256] Ferrari L M, Ismailov U, Badier J-M, Greco F and Ismailova E 2020 Conducting polymer tattoo electrodes in clinical electro- and magneto-encephalography *Npj Flex. Electron.* 4 4
- [257] Xie J, Chen Q, Shen H and Li G 2020 Review—Wearable Graphene Devices for Sensing *J. Electrochem. Soc.* 167 037541
- [258] Zheng Q, Lee J, Shen X, Chen X and Kim J-K 2020 Graphene-based wearable piezoresistive physical sensors *Mater. Today* 36 158–79
- [259] Ferrari L M, Sudha S, Tarantino S, Esposti R, Bolzoni F, Cavallari P, Cipriani C, Mattoli V and Greco F 2018 Ultraconformable Temporary Tattoo Electrodes for Electrophysiology *Adv. Sci.* 5 1700771
- [260] Kabiri Ameri S, Ho R, Jang H, Tao L, Wang Y, Wang L, Schnyer D M, Akinwande D and Lu N 2017 Graphene Electronic Tattoo Sensors *ACS Nano* 11 7634–41
- [261] Yang S, Chen Y-C, Nicolini L, Pasupathy P, Sacks J, Su B, Yang R, Sanchez D, Chang Y-F, Wang P, Schnyer D, Neikirk D and Lu N 2015 “Cut-and-Paste” Manufacture of Multiparametric Epidermal Sensor Systems *Adv. Mater.* 27 6423–30

- [262] Amjadi M, Yoon Y J and Park I 2015 Ultra-stretchable and skin-mountable strain sensors using carbon nanotubes–Ecoflex nanocomposites *Nanotechnology* 26 375501
- [263] Widlund T, Yang S, Hsu Y-Y and Lu N 2014 Stretchability and compliance of freestanding serpentine-shaped ribbons *Int. J. Solids Struct.* 51 4026–37
- [264] Yang S, Su B, Bitar G and Lu N 2014 Stretchability of indium tin oxide (ITO) serpentine thin films supported by Kapton substrates *Int. J. Fract.* 190 99–110
- [265] Arumugam V, Naresh M D and Sanjeevi R 1994 Effect of strain rate on the fracture behaviour of skin *J. Biosci.* 19 307–13
- [266] Lu N, Lu C, Yang S and Rogers J 2012 Highly Sensitive Skin-Mountable Strain Gauges Based Entirely on Elastomers *Adv. Funct. Mater.* 22 4044–50
- [267] Yang S and Lu N 2013 Gauge Factor and Stretchability of Silicon-on-Polymer Strain Gauges *Sensors* 13 8577–94
- [268] Miyamoto A, Lee S, Cooray N F, Lee S, Mori M, Matsuhisa N, Jin H, Yoda L, Yokota T, Itoh A, Sekino M, Kawasaki H, Ebihara T, Amagai M and Someya T 2017 Inflammation-free, gas-permeable, lightweight, stretchable on-skin electronics with nanomeshes *Nat. Nanotechnol.* 12 907–13
- [269] Fang Y, Li Y, Wang X, Zhou Z, Zhang K, Zhou J and Hu B 2020 Cryo-Transferred Ultrathin and Stretchable Epidermal Electrodes *Small* 2000450
- [270] The American Institute of Stress 2014 2014 Stress Statistics
- [271] National Alliance on Mental Illness 2019 Mental Health By the Numbers
- [272] van Praag H M 2004 Stress and Suicide: Are We Well-Equipped to Study this Issue? *Crisis* 25 80–5
- [273] Greco A, Valenza G and Scilingo E P 2016 *Advances in Electrodermal Activity Processing with Applications for Mental Health* (Cham: Springer International Publishing)
- [274] Boucsein W 2012 *Electrodermal Activity* (Boston, MA: Springer US)
- [275] Kappeler-Setz C, Gravenhorst F, Schumm J, Arnrich B and Tröster G 2013 Towards long term monitoring of electrodermal activity in daily life *Pers. Ubiquitous Comput.* 17 261–71

- [276] Edelberg R 1993 Electrodermal Mechanisms: A Critique of the Two-Effector Hypothesis and a Proposed Replacement *Progress in Electrodermal Research* ed J-C Roy, W Boucsein, D C Fowles and J H Gruzelier (Boston, MA: Springer US) pp 7–29
- [277] Fowles D C, Christie M J, Edelberg R, Grings W W, Lykken D T and Venables P H 1981 Publication Recommendations for Electrodermal Measurements *Psychophysiology* 18 232–9
- [278] Posada-Quintero H F and Chon K H 2020 Innovations in Electrodermal Activity Data Collection and Signal Processing: A Systematic Review *Sensors* 20 479
- [279] Greenfield N S and Sternbach R A 1972 *Handbook of Psychophysiology* vol xii (Oxford, UK: Holt, Rinehart & Winston)
- [280] Kim H, Kim Y, Mahmood M, Kwon S, Zavanelli N, Kim H S, Rim Y S, Epps F and Yeo W 2020 Fully Integrated, Stretchable, Wireless Skin-Conformal Bioelectronics for Continuous Stress Monitoring in Daily Life *Adv. Sci.* 2000810
- [281] Yoon S, Sim J K and Cho Y-H 2016 A Flexible and Wearable Human Stress Monitoring Patch *Sci. Rep.* 6 23468
- [282] Ming-Zher Poh, Swenson N C and Picard R W 2010 A Wearable Sensor for Unobtrusive, Long-Term Assessment of Electrodermal Activity *IEEE Trans. Biomed. Eng.* 57 1243–52
- [283] Choi M, Koo G, Seo M and Kim S W 2018 Wearable Device-Based System to Monitor a Driver’s Stress, Fatigue, and Drowsiness *IEEE Trans. Instrum. Meas.* 67 634–45
- [284] Wang S, Yan J, Zhu C, Yao J, Liu Q and Yang X 2020 A Low Contact Impedance Medical Flexible Electrode Based on a Pyramid Array Micro-Structure *Micromachines* 11 57
- [285] Jeehoon Kim, Sungjun Kwon, Sangwon Seo, and Kwangsuk Park 2014 Highly wearable galvanic skin response sensor using flexible and conductive polymer foam *2014 36th Annual International Conference of the IEEE Engineering in Medicine and Biology Society* 2014 36th Annual International Conference of the IEEE Engineering in Medicine and Biology Society (EMBC) (Chicago, IL: IEEE) pp 6631–4
- [286] Montagu J D and Coles E M 1966 Mechanism and measurement of the galvanic skin response. *Psychol. Bull.* 65 261–79

- [287] Lam L K and Szypula A J 2018 Wearable emotion sensor on flexible substrate for mobile health applications *2018 IEEE Sensors Applications Symposium (SAS)* 2018 IEEE Sensors Applications Symposium (SAS) (Seoul, Korea (South): IEEE) pp 1–5
- [288] Tang L, Shang J and Jiang X 2021 Multilayered electronic transfer tattoo that can enable the crease amplification effect *Sci. Adv.* 7 eabe3778
- [289] Taccola S, Poliziani A, Santonocito D, Mondini A, Denk C, Ide A N, Oberparleiter M, Greco F and Mattoli V 2021 Toward the Use of Temporary Tattoo Electrodes for Impedancemetric Respiration Monitoring and Other Electrophysiological Recordings on Skin *Sensors* 21 1197
- [290] Ha M, Cañón Bermúdez G S, Kosub T, Mönch I, Zabala Y, Oliveros Mata E S, Illing R, Wang Y, Fassbender J and Makarov D 2021 Printable and Stretchable Giant Magnetoresistive Sensors for Highly Compliant and Skin-Conformal Electronics *Adv. Mater.* 33 2005521
- [291] Lee S, Franklin S, Hassani F A, Yokota T, Nayeem M O G, Wang Y, Leib R, Cheng G, Franklin D W and Someya T 2020 Nanomesh pressure sensor for monitoring finger manipulation without sensory interference *Science* 370 966–70
- [292] Fang Y, Li Y, Li Y, Ding M, Xie J and Hu B 2020 Solution-Processed Submicron Free-Standing, Conformal, Transparent, Breathable Epidermal Electrodes *ACS Appl. Mater. Interfaces* 12 23689–96
- [293] Benedek M and Kaernbach C 2010 A continuous measure of phasic electrodermal activity *J. Neurosci. Methods* 190 80–91
- [294] Sun J-Y, Lu N, Yoon J, Oh K-H, Suo Z and Vlassak J J 2012 Debonding and fracture of ceramic islands on polymer substrates *J. Appl. Phys.* 111 013517
- [295] Kim R-H, Kim D-H, Xiao J, Kim B H, Park S-I, Panilaitis B, Ghaffari R, Yao J, Li M, Liu Z, Malyarchuk V, Kim D G, Le A-P, Nuzzo R G, Kaplan D L, Omenetto F G, Huang Y, Kang Z and Rogers J A 2010 Waterproof AllInGaP optoelectronics on stretchable substrates with applications in biomedicine and robotics *Nat. Mater.* 9 929–37
- [296] Wang L, Qiao S, Kabiri Ameri S, Jeong H and Lu N 2017 A Thin Elastic Membrane Conformed to a Soft and Rough Substrate Subjected to Stretching/Compression *J. Appl. Mech.* 84 111003
- [297] Gahoi A, Passi V, Kataria S, Wagner S, Bablich A and Lemme M C 2015 Systematic comparison of metal contacts on CVD graphene *2015 45th European*

*Solid State Device Research Conference (ESSDERC) 45th European Solid-State Device Research Conference (ESSDERC 2015) (Graz: IEEE) pp 184–7*

- [298] Robinson J A, LaBella M, Zhu M, Hollander M, Kasarda R, Hughes Z, Trumbull K, Cavalero R and Snyder D 2011 Contacting graphene *Appl. Phys. Lett.* 98 053103
- [299] Adams T and Vaughan J A 1965 Human eccrine sweat gland activity and palmar electrical skin resistance *J. Appl. Physiol.* 20 980–3
- [300] Carretié L, Tapia M, López-Martín S and Albert J 2019 EmoMadrid: An emotional pictures database for affect research *Motiv. Emot.* 43 929–39
- [301] Posada-Quintero H F, Kong Y, Nguyen K, Tran C, Beardslee L, Chen L, Guo T, Cong X, Feng B and Chon K H 2020 Using electrodermal activity to validate multilevel pain stimulation in healthy volunteers evoked by thermal grills *Am. J. Physiol.-Regul. Integr. Comp. Physiol.* 319 R366–75
- [302] Sano A and Picard R W 2011 Toward a taxonomy of autonomic sleep patterns with electrodermal activity *2011 Annual International Conference of the IEEE Engineering in Medicine and Biology Society 2011 33rd Annual International Conference of the IEEE Engineering in Medicine and Biology Society (Boston, MA: IEEE) pp 777–80*